Dynamic changes in mitochondria support phenotypic flexibility of microglia

Katherine Espinoza*[,1,2], Ari W. Schaler *[,1,2], Daniel T. Gray[1], Arielle R. Sass[1], Adrian Escobar[1,2], Kamilia Moore[1], Megan E. Yu[1], Casandra G. Chamorro[1], Lindsay M. De Biase[1,3]

* Equal contribution

[1] Department of Physiology, David Geffen School of Medicine, UCLA, Los Angeles

[2] UCLA Neuroscience Interdepartmental Graduate Program

[3] Department of Neurobiology, David Geffen School of Medicine, UCLA, Los Angeles

Correspondence should be addressed to Lindsay M. De Biase at ldebiase@mednet.ucla.edu

ABSTRACT

Microglial capacity to adapt to tissue needs is a hallmark feature of these cells. New studies show that mitochondria critically regulate the phenotypic adaptability of macrophages. To determine whether these organelles play similar roles in shaping microglial phenotype, we generated transgenic crosses to accurately visualize and manipulate microglial mitochondria. We find that brain-region differences in microglial attributes and responses to aging are accompanied by regional differences in mitochondrial mass and aging-associated mitochondrial remodeling. Microglial mitochondria are also altered within hours of LPS injections and microglial expression of inflammation-, trophic-, and phagocytosis-relevant genes is strongly correlated with expression levels of mitochondria-relevant genes. Finally, direct genetic manipulation of microglial mitochondria alters microglial morphology and leads to brain-region specific effects on microglial gene expression. Overall, this study advances our understanding of microglial mitochondria and supports the idea that mitochondria influence basal microglia phenotype and phenotypic remodeling that takes place over hours to months.

INTRODUCTION

An essential and defining characteristic of microglia is their ability to rapidly remodel their attributes and shift into a wide array of distinct functional states[1–3]. Historically, microglial cellular phenotype was viewed in a binary fashion as either pro-inflammatory (M1, activated) or anti-inflammatory / tissue-reparative (M2, homeostatic)[4]. Work over the past 10-15 years has refined our understanding of microglial function, showing that they can adopt a wide spectrum of transcriptional signatures, morphologies, and secretory/ proliferative/ phagocytic/ migratory profiles[5]. Moreover, the particular combination of microglial properties observed depends on brain region, age, and the presence or absence of chronic stress, high fat diet, and pollution exposure. Distinct tissue injury, infection, and disease processes also elicit unique sets of properties in responsive microglia[5–17], meaning that binary categorization of microglial functional states is far too simplistic and inaccurate.

As the field works to catalogue the spectrum of cellular phenotypes that microglia display in distinct circumstances, efforts have also been made to identify “central” or “master” regulators of microglial phenotype. Key examples include transcription factors that turn on entire programs of microglial gene expression and associated downstream functional capabilities. Other examples include chromatin remodelers that can similarly enable or suppress expression of large numbers of genes that will shape downstream microglial attributes and functions[10,18]. Identifying such central regulators of microglial phenotype that have the capacity to modulate numerous microglial attributes is of high utility for the field. It can assist with defining and categorizing microglial functional states, as they can be determined on the basis of the central regulator rather than panels of 10s-100s of microglial genes, proteins, or functional readouts. These central regulators are also of great interest as potential therapeutic targets that could be utilized to elicit broad changes in microglial function via coordinated regulation of multiple microglial attributes. Recent findings raise the possibility that mitochondria - as organelles - may have the capability to act as master regulators of microglial phenotype in this fashion.

Classically thought of as the ATP producing powerhouse of the cell, mitochondria are now recognized as critical signaling hubs[19–22]. Mitochondria can influence calcium-dependent intracellular signaling pathways via their ability to buffer intracellular calcium. They exert strong

influence on signaling that involves protein post-translational modifications, as mitochondrial metabolic pathways generate many of the metabolites needed for these modifications. Mitochondria can influence the function of cellular endoplasmic reticulum and lysosomes via physical interactions with these organelles, and mitochondria can signal to the nucleus to impact gene expression[19–22]. Research in macrophages supports the idea that mitochondria act as signaling hubs, demonstrating that mitochondria regulate macrophage responses to pathology and ability to shift into distinct inflammatory states[23–29]. Key observations suggest a similarly important role for these organelles in regulating changes in microglial cellular phenotype. Regional differences in microglial phenotype are accompanied by prominent differences in expression of mitochondrial-relevant genes[30], and the state of mitochondria appears to be linked to microglial responses to early life immune challenge, brain injury, and protein aggregates in neurodegenerative disease[31–38]. Yet, direct and rigorous study of these organelles in microglia *in vivo* is minimal and gaps persist in our knowledge about potential mitochondrial regulation of microglial attributes.

To begin addressing this knowledge gap, we sought to analyze the relationship between mitochondria and key microglial attributes in both physiological and pathological contexts. We used multiple transgenic crosses and multidisciplinary approaches to determine whether differences in microglial properties across brain regions during normative aging were accompanied by regional differences in microglial mitochondria. To explore the relationship between these organelles and microglial properties during CNS challenges, we chose pathological insults that differ in their modality (tissue injury vs inflammatory challenge) and time course over which microglia exhibit phenotypic remodeling (minutes vs hours/days). Finally, to probe causal links between mitochondrial state and microglial properties we generated transgenic crosses to selectively manipulate microglial mitochondria and link organelle state to cellular properties. Collectively, these studies advance the field by revealing the mitochondrial landscape within microglia and the relationship of these organelles to microglial phenotypic remodeling across brain regions, in response to inflammatory insult, and during aging.

RESULTS

Region-specific phenotypes of microglia are accompanied by regional differences in mitochondrial mass and number.

Mitochondrial abundance, morphology, and molecular composition vary dramatically across cell types[39], suggesting that the relationship between mitochondria and cellular function cannot be generalized across cell types and needs to be defined on a cell by cell basis. To unequivocally visualize microglial mitochondria, we crossed mice that express inducible cre recombinase in microglia (*CX3CR1*$^{CreER/+}$) with mice that express Cre-dependent mitochondrial-targeted GFP (mitoGFP) (**Fig. 1A**)[40,41]. In fixed tissue from young adult (2mo) double transgenic *CX3CR1*$^{CreER/+}$*;mitoGFP* mice (*MG-mitoGFP* mice hereafter), numerous GFP+ structures could be observed throughout the somas and cell processes of microglia in the nucleus accumbens (NAc) and ventral tegmental area (VTA), two interconnected brain regions where we have extensively mapped microglial phenotypes across the lifespan (**Fig. 1B** and **Fig. S1A,B**)[30,42,43]. Consistent with reports of tamoxifen-independent recombination when using *CX3CR1*$^{CreER/+}$ and reporters with minimal distance between loxP sites[44,45], recombination was observed in approximately 80% of microglia in *MG-mitoGFP* mice without tamoxifen administration (**Fig. S1A - C**) or in oil-injected controls (**Fig. S1D,E**). FACS-based analysis indicated that 4-

hydroxytamoxifen treatment increased recombination to approximately 90% of microglia (**Fig. S1F,G**). Given the high level of tamoxifen-independent recombination, we elected to carry out analyses without tamoxifen treating mice, unless otherwise noted. In terms of cellular and organelle specificity of mitoGFP, FACS analyses indicated that GFP expression was not observed in non-microglial CNS cells (**Fig. S1H,I**). Moreover, in acute brain sections from *MG-mitoGFP* mice, GFP+ structures were consistently colocalized with tetramethylrhodamine (TMRM), a mitochondrial membrane potential indicator, confirming that GFP-tagged structures are mitochondria (**Fig. S1J,K**). Together these results indicate that *MG-mitoGFP* mice accurately label microglial mitochondria.

Microglia show prominent differences in cell density, branching complexity, and gene expression across the NAc and VTA[30]. To determine if these regional differences in baseline microglial attributes were accompanied by regional differences in microglial mitochondria, we carried out high resolution confocal imaging and 3D volumetric reconstruction of both microglia and their mitochondria in the NAc and VTA of young adult mice (**Fig. 1B** and **Fig. S2A**). Consistent with previous findings, microglial tissue coverage in the VTA was lower than that observed in NAc (**Fig. 1C**)[30]. Yet, field of view (FOV) mitochondrial mass (mitochondrial volume relative to microglial volume) and FOV mitochondrial number relative to microglial volume were greater in the VTA compared to the NAc (**Fig. 1D,E**). The FOV sphericity, median volume, max volume, and aspect ratio (longest axis/shortest axis - measure of elongation) of individual mitochondria were relatively consistent across NAc and VTA (**Fig. S2B-E**). Together, these observations indicate that regional differences in microglial cellular phenotype are accompanied by regional differences in some but not all mitochondrial metrics.

Mitochondrial number is partially correlated with morphological complexity of microglia. Microglial capacity to survey the surrounding brain tissue is influenced by the degree of their cell branching complexity. To define how mitochondrial networks relate to microglial branching structure, we crossed *MG-mitoGFP* mice to Ai14 reporter mice to drive cytosolic expression of TdTomato (TdTom) along with GFP tagging of microglial mitochondria (**Fig. 1A**)[40,41,46]. In the absence of tamoxifen injection, incidence of mitoGFP+TdTom+ cells was low enough to allow rigorous and unequivocal reconstruction of the branching patterns of individual microglial cells and their mitochondrial networks in VTA and NAc as well as prefrontal cortex (PFC) (**Fig. 1F and Fig. S2F**). Consistent with previous findings, microglia display morphological differences across these brain regions, with NAc microglia exhibiting greater total process length than VTA microglia (**Fig. 1G**)[30]. PFC microglia displayed total process length comparable to that of VTA microglia. To relate these regional differences in total process length to mitochondria of the cells, we used regression analyses and found that greater process length was significantly associated with higher total volume of mitochondria in NAc microglia (**Fig. 1H**). Both VTA and PFC microglia showed trends toward greater process length being correlated with greater number of mitochondria (**Fig. 1H**). These findings suggest that a greater quantity/volume of mitochondria are needed to support a greater mass of cell processes.

Microglia also displayed regional differences in morphology in terms of total number of branch points, with this metric being elevated in NAc microglia compared to VTA and PFC microglia (**Fig 1I**). Robust regression analyses revealed that greater branching was associated with a greater number of mitochondria for VTA microglia (**Fig. 1J**). Trends toward greater branching being associated with a larger total volume of mitochondria were also evident for NAc and VTA microglia. Intriguingly, these findings suggest that the *architecture* of cell processes, rather than

simply the total *amount* of cell processes, may be related to mitochondrial networks within microglia (**Fig. 1J**). Consistent with this idea, Sholl analysis revealed that both number of intersections (reflecting number of cell process branches / morphological complexity) and number of mitochondria reached a maximum at approximately 20-25 µm from the cell soma in the PFC, NAc and VTA microglia (**Fig. S2G-I**). Hence, the subcellular distribution of the organelles aligns with branching architecture, as opposed to mitochondria being primarily clustered in the soma or at the motile tips of microglial processes. In addition, maximum number of Sholl intersections was significantly correlated with total number of mitochondria in PFC, with NAc and VTA microglia showing trends toward significance in this metric (**Fig. S2J**). Altogether, these analyses suggest that baseline microglial morphology and features of their mitochondria are partially interlinked.

Mitochondrial number and mitochondrial motility are not aligned with microglial tissue surveillance.

Microglia engage in continual morphological remodeling as they survey the surrounding tissue. Microglial tissue surveillance can also vary across brain regions and is assumed to be an energy intensive process[7,47]. However, the relationship between microglial cell process motility and mitochondrial abundance has not been explored. We performed two-photon imaging in acute brain sections prepared from young adult (2-3mo) *MG-mitoGFP;Ai14* mice and recorded motility of NAc and VTA microglial cell processes (TdTom) and attributes of mitochondria (GFP) within these cells (**Fig. 2A,B** and **Fig. S3A-C**). Microglia were imaged at least 60µm below the surface of the brain section. Although microglia show more simplified branching in acute brain sections compared to fixed tissue, total mitochondrial volume and total number of microglial Sholl intersections were positively correlated (**Fig. S3D**), indicating that alignment of mitochondria with morphological architecture of the cells was preserved in acute brain sections. Moreover, microglial motility and mitochondrial motility were not correlated with time elapsed since preparation of brain sections (**Fig. S3E,F**), suggesting that this preparation is well suited for initial exploration of relationships between mitochondria and microglial cell dynamics.

Although NAc and VTA microglia displayed regional differences in morphology and mitochondrial mass in fixed tissue (**Fig. 1**), microglial cell process motility, defined as percent pixel change over a 10 minute period, was similar across NAc and VTA in acute brain sections (**Fig. 2B, C** and **Fig. S3B**). In addition, despite several associations between microglial morphology and features of their mitochondria in fixed tissue (**Fig. 1H,J** and **Fig. S2J**), there was no correlation between total mitochondrial volume or mitochondrial mass and microglial motility in NAc or VTA (**Fig. 2D,E**) in acute brain sections. These observations suggest that there is a more robust relationship between mitochondrial abundance and baseline cell morphology than with dynamic remodeling of that morphology.

Microglial mitochondria themselves also exhibited motility that included jitter, concerted directional movement, and occasional examples of fission and fusion (**Fig. 2F,G** and **Fig. S3C**). These types of mitochondrial motility are consistent with what has been reported in other cell types[29,48]. 3D reconstruction and tracking of mitochondria in Imaris revealed that motility of individual mitochondria (total displacement over 10 minutes) was similar in NAc and VTA microglia, with the majority of mitochondria displaying modest movement (approximately 1µm) and a smaller number of mitochondria showing larger movements of 2-6µm (**Fig. 2H**). To begin exploring whether mitochondrial motility was related to cell processing remodeling of individual microglia, we used robust regression analyses and found that mitochondrial motility (percent

pixel change for all mitochondria in the cell) was not significantly correlated with microglial motility in either the NAc or the VTA (**Fig. 2I**). This was also the case at the level of primary branches of microglia. Even within one microglial cell, some primary branches contained few or no mitochondria while others contained multiple mitochondria. However, there was no significant correlation between motility of primary microglial branches and either mitochondrial motility (**Fig. 2J**) or mitochondrial mass within those branches (**Fig. S3G**). Altogether, these data further reinforce the idea that mitochondria are not tightly linked to baseline microglial tissue surveillance within a 10 minute time frame.

Mitochondrial distribution is stable during early phases of microglial response to focal injury.

In addition to homeostatic tissue surveillance, microglia exhibit rapid and robust cell process extension toward focal sites of CNS injury[49–51]. In acute brain sections from *MG-mitoGFP;Ai14* mice, we induced focal laser lesions and imaged the response of both microglia and their mitochondria to this insult. Consistent with previous findings in the field[49,52], microglia rapidly extended cell processes toward and contacted the lesion within 5 min (**Fig. 3A-G**). However, these rapidly extending cell processes did not contain any mitochondria and no mitochondria were trafficked into lesion-responsive cell processes during the imaging period (**Fig. 3A-E**). Quantitative analyses confirmed minimal change in mitochondrial (GFP+) signals within 30µm of the lesion over a 20 minute period (**Fig. 3H,I**). Qualitative observations suggested minimal remodeling of mitochondria in the somas and non-extending processes of microglia that responded to laser lesion (**Fig. 3A-E, zoom**). Minimal mitochondrial remodeling was also observed in a subset of experiments where imaging time was extended to 70 minutes post-lesion (*not shown*).

Mitochondrial remodeling is evident at the earliest stages of microglial responses to inflammatory challenge.

Microglia respond to a wide variety of CNS insults that vary substantially in both the nature of the insult (injury vs. infection vs. disease process vs. pathological electrical activity etc.) as well as the time course over which microglial responses emerge and evolve (minutes to months). Given lack of clear evidence for mitochondrial involvement in rapid microglial responses to tissue injury, we sought to further explore the relationship between mitochondria and microglial phenotypic remodeling using a pathological insult of distinct modality as well as time course. Intraperitoneal (i.p.) injections of lipopolysaccharide (LPS), a component of the cell wall of gram-negative bacteria, were used to model inflammatory responses that accompany infection. Microglia show prominent changes in gene expression within hours of LPS injection and changes in morphology by 24-48 hours post-injection[53]. *In vitro* LPS exposure alters microglial mitochondrial structure and function[54–57] and, in macrophages, mitochondrial alterations play an essential role in enabling and regulating changes in macrophage attributes as they respond to inflammatory challenges[24–27,29,58,59]. All together, these findings suggest that there may be important relationships between mitochondria, as organelles, and microglial responses to inflammatory challenge.

Young adult (3-4mo) *MG-MitoGFP* mice were given i.p. injections of saline or LPS and microglial gene- and protein- expression were analyzed via FACS, using the previously described gating strategy to identify and isolate microglia (**Fig. S1D**), followed by downstream qPCR (**Fig. 4A**). High expression of key microglial genes (*Cx3cr1* and *P2ry12*) and little to no expression of oligodendrocyte-lineage, astrocyte-, and neuron-specific genes (**Fig. S4A**)

confirmed fidelity of our microglial isolation. Within 4hr of LPS challenge, microglia from both striatum (STR, containing NAc) and midbrain (MB, containing VTA) upregulated transcripts for pro-inflammatory factors (*Il1β, Tnfα*), and downregulated transcripts for homeostatic microglial genes (*Tgfβ1, P2ry12, Cx3cr1*), consistent with previous studies[53,60]. Upregulation of genes associated with microglial phagocytic function (*Cd45, Itgam*) was evident by 24hr post injection (**Fig. 4B, S4B** and **Table S1, S2**). Overall, STR and MB microglia responded similarly to LPS challenge at the gene expression level.

Microglial expression of mitochondrial-function related genes was also altered at both 4hr and 24hr post injection (**Fig. 4B, S4B** and **Table S1, S2**). Within 4hr of LPS challenge, genes related to mitochondrial ROS handling (*Sod2, Cat*), mitochondrial fission (*Dnm1l*), and mitochondrial biogenesis (*Nrf1*) were significantly altered. Some of these gene expression changes were maintained into 24hr post injection (*Sod2, Dnm1l*), while others appeared more restricted to the 4hr time point (*Cat, Nrf1*). At 24hr post injection, prominent upregulation of electron transport chain component genes *Ndufa12* (Complex I), *Cox4i1* (Complex IV), and *Atp5d* (Complex V) emerged. Genes related to mitochondrial calcium handling (*Vdac1, Micu1*) were also significantly altered. Again, most gene expression changes were similar across STR and MB, (**Fig. 4B, S4B** and **Table S1, S2**).

To probe the relationship between mitochondrial state and key features of microglia as they respond to inflammatory challenge, we used Principal Component Analysis (PCA) and found that PCA based solely on expression patterns of mitochondrial function-relevant genes can explain 64.7% of sample variation with the first 2 components and 81% of variation with the first 3 components (**Fig. 4C** and **Fig. S4C**). Moreover, 24hr post injection samples cluster away from Saline samples (**Fig. 4C**) and 4hr post injection samples are interspersed among Saline samples or skewed toward the 24hr samples. Hence, without even considering microglial inflammatory genes or homeostatic genes, microglia that are responding to LPS challenge can be clearly identified on the basis of their mitochondrial function profiles. We also used robust regression analyses and found numerous correlations between individual microglial-state and mitochondrial state genes (**Fig. 4D** and **Table S3**). For example, expression of homeostatic microglial gene *P2ry12* showed significant correlation with electron transport chain (ETC) genes (*Ndufa12, Sdha*) as well as *Tfam*, which influences expression of mitochondrial DNA encoded ETC genes, in saline treated animals, but the majority of these correlations were lost at 4hr post LPS. Microglial pro-inflammatory genes *Il1β* and *Tnfα* showed significant correlation with mitochondrial biogenesis genes (*Nrf1, Tfam*), mitochondrial fusion and fission genes (*Mnf1, Dnm1l*) and the ROS handling gene *Sod2* at 4hr post LPS (**Fig. 4D** and **Table S3**). Microglial- and mitochondrial- gene correlations remained abundant and continued to evolve at 24hrs post LPS.

Together these data indicate that numerous facets of mitochondrial function are remodeled during microglial responses to inflammatory challenge and that mitochondrial remodeling begins at the earliest stages of microglial responses to inflammatory challenge. Moreover, examination of *Cd68*, a key microglial lysosome gene, hints that mitochondria, as organelles, may be uniquely positioned to regulate microglial functional state during inflammatory challenge. While LPS treatment increased the correlation between most mitochondria-relevant genes and key microglial function genes (*Cd45*, *Cx3cr1*, *P2ry12*, *Tgfβ1*) (**Fig. 4D**), LPS treatment did not modulate correlations between *Cd68* and *Cx3cr1*, *P2ry12*, *Tgfβ1* (correlations between *Cd68* and *Cd45* increased at 24hrs post LPS) (**Fig. S4D** and **Table S4**). Moreover, while multiple

mitochondria-relevant genes were positively correlated with expression of the microglial pro-inflammatory factors *Tnfα* and *Il1β* at 4hrs post-LPS, *Cd68* expression was not correlated with *Tnfα* and *Il1β* in any of the conditions examined (**Fig. S4D**).

The transcript-level, qPCR-based analyses presented thus far show high sensitivity for detection of early changes in cell and organelle state following LPS challenge. To test for protein-level changes following the LPS challenge, we analyzed data recorded during FACS isolation of microglia. These analyses revealed that the intensity of GFP, reflecting mitochondrial mass, was significantly increased at 24hr post injection in both the STR and MB, with hints of emerging increases at 4hrs post injection (**Fig. 4E, 4F**). In contrast, mitochondrial membrane potential, as detected by TMRM intensity, decreased significantly at 24hr post LPS (**Fig. 4E, 4F**). These changes in mitochondrial mass and mitochondrial membrane potential were accompanied by significant protein-level increases in CD45 by 24hr in STR microglia and trends toward increased CD45 in MB microglia. Protein level expression of CX3CR1 and P2RY12 differed across regions but not across treatment (**Fig S4E**). Microglial size, as indicated by forward scatter, was significantly elevated in both STR and MB by 24hrs post LPS, while internal complexity (side scatter) remained unchanged (**Fig S4E**). These data confirm that changes in mitochondrial state at the protein and functional level are associated with changes in microglial protein-level expression and cell structure.

Increased mitochondrial mass and mitochondrial elongation are associated with microglial responses to inflammatory challenge.
To investigate how LPS challenge impacts morphology of microglial mitochondria, we analyzed fixed tissue from 3-4mo *MG-MitoGFP* mice (**Fig. 5A**, **Fig. S5A**) at 24hr post-LPS, when protein-level changes in microglia and their mitochondria were most evident via FACS (**Fig. 4**). 3D reconstruction of both microglia and their mitochondria in NAc and VTA revealed significant increases in mitochondrial mass at 24hr post LPS (**Fig. 5B**), consistent with FACS-based analyses of GFP and qPCR-based increases in mitochondrial biogenesis factor *Nrf1*. No significant changes in mitochondrial number (relative to cell volume) were detected (**Fig. 5C**) and, instead, microglial mitochondria showed significant elongation, as detected by increases in aspect ratio (**Fig. 5D**). Elongation of mitochondria has been associated with increased capacity for oxidative phosphorylation[61–63], which would be consistent with the qPCR-based observation of robust increases in electron transport chain components (*Ndufa12, Atp5d, Cox4i1*) at 24hrs post LPS (**Fig. 4B**). Collectively, these findings indicate that mitochondrial structural remodeling is a key component of microglial responses to inflammatory challenge.

Microglial mitochondria undergo morphological and functional changes during aging.
The results described above indicate that there are key relationships between mitochondria and region-specific microglial morphology (**Fig. 1**), as well as microglial expression of homeostatic genes and inflammatory factors in the context of an inflammatory insult (**Fig. 4**). Microglia exhibit numerous changes during aging, including altered morphology and inflammatory profile[13,43,64–66]. Altered mitochondrial function is heavily implicated in CNS aging, but aging-associated changes in mitochondria have not been investigated with cellular specificity[67–69]. Hence, whether and how mitochondrial remodeling is linked to changing microglial attributes during aging is unknown. We also showed previously that microglial responses to aging vary across brain regions, with VTA microglia displaying proliferative and inflammatory changes months before microglia in the NAc[43]. Whether there are links between mitochondrial state and early VTA microglial aging has also not been investigated.

To determine if aging-associated changes in microglial morphology and inflammatory profile are accompanied by changes in their mitochondria, we analyzed NAc and VTA microglial mitochondria in fixed tissue from middle age (12-13mo) and late middle age (16-18mo) *MG-MitoGFP* mice (**Fig. 6A**) and compared them to microglial mitochondria in young adult (2-3mo) mice. Tissues were treated with TrueBlack to quench autofluorescent aggregates (lipofuscin) that emerges during aging and any dim residual signals in microglia could be clearly distinguished from *MG-MitoGFP* signal during analysis (**Fig. S6A**)[70]. With age, mitochondrial mass tended to increase, particularly in the VTA, and significant increases in mitochondrial number (relative to cell volume) were observed in both NAc and VTA microglia (**Fig. 6B,C**). VTA microglia also showed significant increases in mitochondrial elongation at 16-18mo (**Fig. 6B,C**). Hence, at the level of mitochondrial structure, LPS challenge and aging both elicit similar types of mitochondrial remodeling.

Although aging impacts microglia in both the NAc and VTA, key regional differences in microglial aging are also apparent. VTA microglia show more prominent lysosome swelling, proliferation, and inflammatory profiles, while NAc microglia show more prominent reductions in cell branching complexity[43]. To further explore how regional differences in microglial aging relate to mitochondrial remodeling during aging, within mouse comparisons were carried out using paired t-tests. This analysis revealed that the elevated mitochondrial mass and mitochondrial number in VTA microglia relative to NAc microglia that were observed at 2-3mo were no longer significant at 12-13mo and 16-18mo, likely due to increased mouse to mouse variation (**Fig. S6B,C**) and increased mitochondrial number (relative to cell volume) in NAc microglia. Finally, VTA microglia exhibited elevated aspect ratio (greater mitochondrial elongation) relative to NAc microglia at 16-18mo (**Fig. S6D**). Therefore, some regional differences in microglial mitochondria that are evident in young adulthood (mitochondrial mass and number) are lost during aging, while other regional differences in microglial mitochondria are gained (elongation).

To further explore how aging impacts microglial mitochondria, we used the previously described gating strategy (**Fig. S1D**) for FACS-based analysis of microglia from 3mo and 18mo *MG-mitoGFP* mice. This analysis revealed that median fluorescence intensity of GFP was significantly increased with age in both STR (containing NAc) and MB (containing VTA) microglia (**Fig. S6E**), pointing to increases in mitochondrial mass. Conversely, mitochondrial membrane potential (TMRM intensity normalized to GFP) was significantly reduced with age in both regions (**Fig. 6D,E**). To confirm changes to mitochondrial membrane potential and further elucidate the time course of such changes, we analyzed TMRM intensity of microglia from WT mice and included an intermediate 12-13mo time point. In this analysis, MB microglia exhibited slightly more depolarized mitochondrial membrane potential (lower TMRM intensity) than STR microglia in 2-3mo old mice (**Fig. 6F**). These regional differences grew progressively larger in 12-13mo old mice (**Fig. 6F**) and 16-18mo old mice (**Fig. S6F**). Examining the time course of TMRM changes within each region revealed subtle but significant depolarization in 12-13mo MB microglia and pronounced depolarization in 16-18mo MB microglia, compared to MB microglia from 2-3mo mice. Interestingly, STR microglia exhibited hyperpolarized mitochondrial membrane potential (higher TMRM intensity) in 12-13mo mice compared to 2-3mo mice. At 16-18mo, however, they showed depolarized mitochondrial membrane potential, relative to microglia from 2-3mo mice (**Fig. 6F**). Together, these findings indicate that the functional status of microglial mitochondria changes significantly during aging, with key differences in the time course and magnitude of these changes across brain regions. Moreover, they reveal that

remodeling of microglial mitochondrial status begins in middle age, rather than late stages of aging.

Targeted genetic manipulation of microglial mitochondria elicits changes in microglial morphology and gene expression.
Results presented thus far indicate that there are correlations between region-specific microglial morphology and mitochondrial mass/number. They also reveal correlations between mitochondrial mass, mitochondrial elongation, mitochondrial membrane potential and changes in microglial morphology and inflammatory profiles during responses to LPS challenge and aging. To further probe whether there are causal links between mitochondria and these microglial phenotypic attributes, we crossed *CX3CR1*$^{CreER/+}$ mice and *CX3CR1*$^{CreER/+}$*;mitoGFP* mice with *Tfam*$^{fl/fl}$ mice to achieve targeted deletion of mitochondrial transcription factor A (TFAM) in microglia (*MG-TFAMKO* or *MG-mitoGFP-TFAMKO*)(**Fig. 7A**). TFAM deletion in diverse cell types leads to reduced expression of electron transport chain subunits encoded by mitochondrial DNA and gives rise to changes in mitochondrial membrane potential and mitochondrial morphology, making this an ideal genetic manipulation to further elucidate the relationship between mitochondria and microglial phenotype[71–75].

For these experiments, mice were injected with 4-hydroxytamoxifen and analyzed 2 months later to allow for both TFAM deletion and turnover of existing mitochondrial components that will be impacted by TFAM deletion, as mitochondrial proteins are among the most long-lived within the cell[76]. This interval also allows for replacement of any peripheral CX3CR1+ cells that experience TFAM deletion in these mice. FACS followed by qPCR confirmed that this treatment paradigm resulted in downregulation of *Tfam* in both STR and MB microglia in *MG-TFAMKO* mice (**Fig. 7B**). Histology in fixed tissue revealed that microglial TFAM loss resulted in increased mitochondrial volume, mitochondrial number, and mitochondrial sphericity at the tissue (FOV) level in *MG-mitoGFP-TFAMKO* mice (**Fig. 7C-F, Fig. S7A**)**.** Mean intensity of the mitoGFP signal was also elevated in *MG-mitoGFP-TFAMKO* mice in both NAc and VTA (**Fig. S7A-S7C**). This increase in GFP intensity appeared to vary substantially from cell-to-cell in *MG-mitoGFP-TFAMKO* mice and may reflect incomplete TFAM recombination in some microglia. Analysis of individual cells confirmed increases in mitochondrial number and trends toward increased mitochondrial sphericity in microglia from *MG-mitoGFP-TFAMKO* mice (**Fig. S7D,E**). This analysis also highlighted increased cell-cell variation in microglia from *MG-mitoGFP-TFAMKO* mice. Some properties of microglial mitochondria, such as FOV median and max mitochondrial volume, were unchanged following TFAM loss (**Fig. S7F**). Together, these findings confirm that this genetic manipulation induces changes to some of the same mitochondrial attributes (number, sphericity, GFP intensity) that differ across brain regions and that are remodeled during microglial responses to LPS and aging.

To determine how genetically-induced changes in mitochondrial status relate to microglial properties, we analyzed microglial density, tissue coverage, and individual microglial morphological complexity. Microglial density did not differ significantly between *MG-mitoGFP-TFAMKO* and control mice (**Fig. 7G**). However, microglial tissue coverage was significantly increased in both NAc and VTA microglia from *MG-mitoGFP-TFAMKO* mice (**Fig. 7H**), suggesting that this manipulation caused changes to microglial morphology. To investigate this possibility, we also reconstructed individual microglial cells and assessed branching complexity via Sholl analysis. The total number of Sholl intersections was elevated in microglia from *MG-mitoGFP-TFAMKO* mice, particularly in the NAc (**Fig. 7I**), supporting the idea that there are important links between mitochondrial state and microglial morphology. Moreover, this *increase* in morphological complexity suggests that TFAM deletion does not simply make microglia “reactive” or compromise their health. Finally, no significant changes were observed in FOV mitochondrial number (relative to FOV microglial volume) or mitochondrial mass in *MG-*

mitoGFP-TFAMKO mice (**Fig. 7J-K**), which would be expected if both microglial volume and mitochondrial number/volume are increased in these mice.

To further elucidate how genetically targeted manipulation of microglial mitochondria affects microglial properties, we used FACS analysis of STR and MB microglia (gated via the previously described strategy, **Fig. S1D**) as well as qPCR for a panel of microglial- and mitochondrial-function related genes. FACS analysis revealed significant increases in microglial forward scatter (FSC, cell size) and side scatter (SSC, internal cellular complexity) in *MG-TFAMKO* samples (**Fig. 8A**), consistent with observed increases in microglial tissue coverage/volume (**Fig. 7H**). Protein level expression of CD45 and CX3CR1 (median fluorescence intensity, MFI, measured during FACS) differed across brain region, but was not significantly altered by TFAM loss. qPCR analysis revealed that multiple mitochondria-related genes were altered in response to TFAM knockout. This included increased expression of genes coding for components of the electron transport chain (*Ndufa12, Atp5d, Cox4i1, Sdha*), as well as genes related to mitochondrial ROS (*Sod2* and *Cat*) and calcium handling (*Micu1*, **Fig. 8B**, **Fig. S8A** and **Table S5**). Mitochondrial biogenesis genes *Nrf1* and *Ppargc1a* also showed significant changes, but in opposite directions (**Fig. 8B**, **Fig. S8A** and **Table S5**). Mitochondrial fusion gene *Dnm1l* was significantly decreased and there were no significant changes in expression of mitochondrial fission associated gene *Mfn1* (**Fig. 8B**, **Fig. S8A** and **Table S5**). Together, these data indicate that loss of microglial TFAM induces broad changes to expression of nuclear-encoded, mitochondria-relevant genes and suggest that multiple aspects of mitochondrial function are impacted by this manipulation.

These alterations in mitochondrial state upon TFAM knockout were accompanied by significant changes in genes related to key microglial functions. Proinflammatory transcripts *Il1β* and *Tnfα* were significantly increased in *MG-TFAMKO* microglia while *Ifnβ1* was significantly decreased. For multiple microglial genes that show regional differences in expression (*Cd45, Cd68, P2ry12*), these regional differences were preserved in TFAM knockout mice, and were not significantly modulated by TFAM loss. Instead, *Tgfβ1* and *Cx3cr1*, which have both been implicated in modulation of overall microglial phenotype, were significantly increased in microglia from *MG-TFAMKO* mice (**Fig. 8C**). Post hoc analysis revealed that many of the gene expression changes associated with TFAM KO occurred in a brain region specific manner. Increases in *Tnfα* were primarily observed in MB TFAM knockout samples, while increases in *Tgfβ1* and *Cx3cr1* were only prominent in STR TFAM knockout microglia (**Fig. 8C** and **Table S5**). Leveraging PCA analysis to examine these gene expression changes in an integrated fashion revealed that *MG-TFAMKO* samples from STR and MB appeared to cluster separately from one another (**Fig. 8C** and **Fig. S8B-C**), providing further evidence that manipulating mitochondrial function exerts distinct effects on STR and MB microglia.

Loss of TFAM causes subtle changes in LPS-induced mitochondrial remodeling and microglial responses to inflammatory challenge

In addition to defining how mitochondrial manipulation impacts basal microglial phenotype, we sought to investigate the impact of TFAM knockout on microglial ability to respond to an inflammatory challenge. To this end, *MG-mitoGFP-TFAMKO* and *MG-mitoGFP* control mice were given i.p. injections of LPS and microglial gene- and protein- expression were analyzed via FACS and downstream qPCR. To maximize ability to detect protein level alterations, as well as catch potential differences in time course of microglial transcriptional responses, samples were collected and analyzed at an intermediate time point (12hrs) between those examined previously (4hrs and 24hrs, **Fig. 4,5**). On the whole, TFAM loss did not appear to substantially impair remodeling of microglial mitochondria following LPS treatment. For example, both microglia from *MG-mitoGFP* control and *MG-mitoGFP-TFAMKO* mice showed increased mitoGFP at 12hrs post LPS (**Fig. 8D**), consistent with previous observations of increased

mitoGFP at 24hrs post LPS (**Fig. 4F**). Moreover, the magnitude of the mitoGFP increase did not differ across genotypes. TMRM levels, which were seen to decrease at 24hrs post LPS (**Fig. 4F**), had not yet declined at 12hrs post LPS and did not differ across genotypes (**Fig. S8D**). Similarly, at the transcript level, LPS-induced changes in expression of mitochondria-relevant genes appeared to proceed irrespective of TFAM loss (**Table S6**). For example, *Sod2* (up-regulated at 4hrs and 24hrs compared to saline) and *Vdac1* (down regulated at 4hrs compared to saline) were still up- and down-regulated in TFAM KO microglia at 12hrs post LPS (**Fig. S8F, G**). In cases where significant differences were observed across genotypes, many of these were already evident without LPS challenge. For example, *Cox4i* was elevated in TFAM KO microglia relative to controls at baseline (**Fig. 8B**), and it remained elevated relative to controls after LPS (**Fig. S8H**).

The microglial response to LPS-challenge was also largely preserved at both the protein- and gene- expression irrespective of TFAM loss. Microglia from both *MG-mitoGFP* control and *MG-mitoGFP-TFAMKO* mice showed increases in FSC (cell size) at 12 hrs post injection (**Fig. 8D**), consistent with observations at 24hrs post LPS (**Fig. 4F**). TFAM KO microglia showed significantly higher FSC than control microglia, but this increased FSC was already evident in the absence of LPS treatment (**Fig. 8A**). Regional differences in expression of CD45 and CX3CR1 across STR and MB that were present at baseline in TFAM KO and control microglia (**Fig. 4F**, **Fig. S4E**, **Fig. 8A**) remained present at 12hrs post LPS (**Fig. 8D**, and **S8D**). At the transcript level, the prominent increases in *Tnfα* and *Il1β* that are observed following LPS injection (**Fig. 4B**), were still observed in TFAM KO microglia (**Fig. 8E** and **Fig. S8H**) and did not differ significantly in magnitude from responses in control microglia. Similarly, LPS-induced downregulation of homeostatic transcripts *Tgfβ1* and *Cx3cr1* did not differ across genotypes (**Fig. 8E** and **Fig. S8I**). Expression levels of *Cd68* and *Itgam* did differ significantly across genotypes, with TFAM KO microglia showing more muted reductions in expression compared to control samples at 12hrs post LPS injection (**Fig. 8E**).

Altogether, these subtle differences in response to LPS challenge were evident in PCA analysis comparing the gene expression patterns of saline treated *MG-mitoGFP* samples (**Fig. 4B**), untreated *MG-TFAMKO* samples (**Fig. 8B**), and 12hr LPS treated control and *MG-mitoGFP-TFAMKO* samples. This analysis revealed that LPS-treatment was the strongest driver of sample clustering (**Fig. 8G**) on PC1, with genotype effects being evident on PC2. Together, these data suggest that microglial mitochondrial remodeling and changes in microglial attributes in response to acute inflammatory challenge remain largely intact in *MG-mitoGFP-TFAMKO* mice. Future studies using repeated or chronic inflammatory challenge will be needed to determine whether the subtle differences in mitochondrial remodeling that were observed lead to more prominent downstream shifts in microglial function.

DISCUSSION

Changes in mitochondrial function have been associated with developmental delays, epilepsy, psychiatric disorders, aging, and neurodegeneration[77,78]. A key priority in uncovering how mitochondria are linked to CNS pathology is understanding how mitochondria impact the function of specific CNS cells. However, because mitochondrial structure and molecular composition vary widely across distinct cell types[39], findings about the functional roles of these organelles cannot be generalized and mitochondria need to be studied with cellular specificity. Our study provides detailed information about microglial mitochondria and supports the idea that mitochondrial function is distinct across CNS cells. We observed that mitochondria occupy about 4-6% of microglial volume, and entire microglial branches sometimes have few, if any,

mitochondria (**Fig. 1** and **Fig. 2**). This is similar to mature oligodendrocytes, where mitochondria make up about 4% of cell volume[79] but unlike astrocytes where mitochondria make up about 80% of astrocyte volume in young adult mice[80]. Qualitatively, our experiments using TMRM incubation in acute brain sections also suggest that microglial mitochondria are less hyperpolarized than mitochondria of surrounding cells (**Fig. S1H**). Hence, our study underscores the need for cell-specific study of mitochondria in CNS cells and argues for caution in assuming that relationships between mitochondria and cell function in one cell type will also hold true for other cell types.

Previous studies have suggested that mitochondrial function in microglia changes in the context of disease, stress, and immune activation[31,32,52–54]. Almost nothing is known, however, about how these organelles are linked to physiological functions of microglia. We found key relationships between mitochondrial abundance and total process length as well as branching complexity of microglia (**Fig. 1**). Hence, even if microglia have fewer mitochondria than other CNS cells, our data suggest that these organelles play a key role in shaping general cellular architecture of microglia. This finding is further supported by our observation that targeted manipulation of microglial mitochondria (deletion of microglial TFAM) led to increased branching complexity of NAc and VTA microglia (**Fig. 7I**), as well as increased cell size assessed via FACS (**Fig. 8A**). Our qPCR-based analyses also indicated that expression of critical homeostatic microglial gene *P2ry12* was significantly correlated with expression of multiple mitochondrial genes under basal conditions. Moreover, targeted manipulation of microglial mitochondria (deletion of microglial TFAM) increased expression of the homeostatic microglial genes *Cx3cr1* and *Tgfβ1*, providing further evidence that the state of mitochondria impacts multiple molecules involved in basal microglial phenotype. Finally, regional specialization is also a key feature of homeostatic microglia[6,9,10,30,42] and we found that regional differences in microglial cellular phenotype were accompanied by regional differences in mitochondrial mass, mitochondrial number, and mitochondrial membrane potential in young adult mice (**Fig. 1** and **Fig. 6**). Altogether, these observations indicate that mitochondrial status is tightly linked to key microglial attributes under physiological conditions.

Additional studies will be required to fully elucidate the significance for physiological microglial function if a microglial cell exhibits higher mitochondrial mass, mitochondrial number, and/or distinct mitochondrial membrane potential. Increased mitochondrial mass, at the most basic level, means that a cell exhibits increased volume of mitochondria relative to the cell volume. While this could imply, simplistically, that a given cell has elevated energetic needs, interpretation of increased mitochondrial mass is not so straightforward. Abundance of electron transport chain (ETC) components can vary across individual mitochondria[81,82], meaning that more mitochondrial volume does not automatically equate to enhanced capacity for oxidative phosphorylation and ATP production. Some mitochondria lack cristae and are specialized in reductive synthesis of macromolecules[81] needed to support growth and other cellular functions. The subcellular localization of mitochondria also matters. For example, mitochondria at pre-synaptic terminals in neurons play critical roles in calcium buffering[83]. Alternatively, mitochondria positioned together with ER membranes play critical roles in lipid synthesis and regulation of autophagy and inflammasome activation[84]. Thus, an elevated mitochondrial mass could have different functional implications depending on subcellular location.

In the present study, we did not observe obvious differences in subcellular distribution of mitochondria between NAc and VTA microglia (**Fig. S2G-I**) nor did we observe significant

differences in the morphology/elongation of individual mitochondria (**Fig. S2B-E**) across these brain regions. We previously found via RNAseq of NAc and VTA microglia that the latter express higher levels of *Vdac1* and *Vdac2* (mitochondrial calcium channels) as well as *Sod2* (reactive oxygen species buffer). At the same time, VTA microglia express lower levels of *Atp5k* and *Atp5g2* (components of the ATP synthase). Taken together, these observations raise the possibility that elevated mitochondrial number and mitochondrial mass in VTA microglia may be related to non-ATP production functions of mitochondria. This idea would also be consistent with the observation of more depolarized mitochondrial membrane potential (lower TMRM intensity) observed in MB microglia (**Fig. 6F**), as mitochondrial membrane potential fuels ATP production. Future studies can employ genetically-encoded mitochondrial calcium indicators and genetically-encoded mitochondrial ROS indicators as well as strategies to perturb mitochondrial calcium channels and ROS regulatory molecules in microglia to further elucidate functional significance of regional differences in microglial mitochondrial mass and number.

The idea that non-ATP producing functions of mitochondria are important for microglia is also supported by our unexpected finding that microglial cell process motility did not show a positive correlation with abundance of mitochondria (**Fig. 2**). We also analyzed movement of the mitochondria themselves and observed the same forms of dynamic mitochondrial remodeling (fission, fusion, trafficking) described in other cell types. Yet, we failed to find any association between mitochondrial displacement and cell process motility, suggesting that mitochondrial trafficking to specific subcellular locations is not required for overall baseline microglial tissue surveillance. Connections between abundance of mitochondria and cell process remodeling of fine branchlets may exist, however. Using *in vivo* multiphoton imaging, Pietramale and colleagues found that microglial branchlets with fewer mitochondria were more likely to be fully retracted[85]. Finally, we found that mitochondria are relatively stable within microglia as they rapidly extend cell processes toward focal laser lesions (**Fig. 3**). Similar responses were observed *in vivo* by Pietramale and colleagues during early phases of microglial responses to laser lesion. Intriguingly, at longer intervals post-lesion (6hrs) they did observe significant mitochondrial remodeling in nearby microglia, suggesting roles for these organelles in microglial injury responses over hours-to-days[85]. Microglial tissue surveillance and rapid tissue injury responses are assumed to be energy intensive processes. It may be, however, that the more rapid, albeit less efficient, process of glycolysis provides the primary energetic support for microglial tissue surveillance and injury responsive motility. Future studies will need to investigate highly localized relationships between microglial filopodia and nearby mitochondria to examine whether mitochondrial membrane potential or other features of mitochondrial state (e.g. fission and fusion) are linked to movement of adjacent cell processes. Improvements in optical tools for detection of ATP[86] and glycolytic function can also be used in conjunction with assessment of mitochondrial abundance and localization to expand our understanding of how these organelles do or do not support the energetics of microglial motility.

Our LPS experiments indicate that remodeling of mitochondrial function is an early and prominent component of microglial responses to inflammatory challenge. Our finding of mitochondrial elongation following LPS challenge differs from *in vitro* experiments that found fragmented mitochondria in primary microglia treated with LPS for 24hrs[54]. Differences between *in vitro* versus *in vivo* microglia and direct versus systemic LPS treatment likely contribute to these distinct findings. In our experiments, rapid increases in microglial *Tnfα* and *Il1β* mRNA were accompanied by altered expression of multiple mitochondrial-relevant genes (**Fig. 4**). Moreover, expression levels of *Tnfα*, *Il1β*, and *Cd45* in individual samples at 4hr post-LPS were

significantly correlated with expression levels of genes involved in mitochondrial fission and fusion, calcium handling, and ROS handling, in addition to genes involved in mitochondrial biogenesis and oxidative phosphorylation. These findings support the possibility that mitochondrial signaling *regulates* changes in microglial attributes rather than simply altering energy production to support a newly emerging cellular phenotype. The idea that mitochondrial state may regulate inflammatory profiles of microglia is further supported by the increased expression of *Tnfα* and *Il1β* in TFAM KO microglia, particularly in the midbrain (**Fig. 8B**). These qPCR results also suggest important future directions for investigation of the links between mitochondria and microglial inflammatory responses. For example, the surge in mitochondrial biogenesis transcription factor *Nrf1* at 4hrs post LPS (**Fig. 4B**) followed by significant increases in mitoGFP signal by 12hrs post LPS (**Fig. 8D**) suggest that targeted impairment of mitochondrial biogenesis capacity may be a fruitful strategy for dissecting how these organelles regulate microglial responses to inflammatory challenge.

Although TFAM deletion led to significant increases in microglial branching (**Fig. 7I**), overall cell size (**Fig. 8A**), and expression of inflammatory and homeostatic microglial genes (**Fig. 8B**), the impact of TFAM loss on acute microglial responses to LPS was relatively muted (**Fig. 8D-F**). A key consideration in interpreting these results is that TFAM loss did not substantially interfere with ability of microglia to increase mitochondrial biogenesis (increase mitoGFP) and alter expression of nuclear-encoded, mitochondria-relevant genes in response to LPS challenge. Hence, additional mitochondria-targeted manipulations will be needed to fully elucidate the relationship between this organelle and microglial responses to inflammatory challenge. Given that TFAM-KO microglia exhibit distinct morphology and expression of inflammatory and homeostatic genes at baseline, it will also be of interest to examine their responses to more chronic or repeated challenges, such as those encountered during normative aging or in the context of neurodegenerative disease. Although the impact of TFAM loss on acute inflammatory microglial responses is subtle, the cumulative effect of these subtle changes during a chronic challenge may be substantial.

Importantly, targeted manipulation of microglial mitochondria did not impact MB and STR microglia in the same way (**Fig. 8C**), suggesting that mitochondrial regulation of microglial function is not equivalent throughout the brain. Following TFAM loss, MB microglia showed substantial changes in proinflammatory genes (upregulation of *Tnfα* and *Il1β*, and down regulation of *Ifnβ1*). STR microglia, instead, exhibited prominent upregulation of homeostatic genes *Cx3cr1* and *Tgfβ1*. These findings align with some of our prior observations of regional differences in microglial responses to aging. Previously, we showed that VTA microglia exhibit early proliferative and inflammatory responses compared to NAc microglia during aging[43]. In the current study, we demonstrated similar trends in mitochondria, with MB microglia showing earlier and more prominent aging-induced changes to mitochondrial membrane potential compared to STR microglia (**Fig. 6**). When combined with our observation that targeted manipulation of microglial mitochondria leads to prominent changes in inflammatory factor expression specifically in MB microglia (**Fig. 8**), our findings support the idea that VTA/MB microglia are uniquely vulnerable to perturbations of mitochondrial function and that mitochondrial function is intimately linked to inflammatory profiles of these MB microglia. Multiple mutations that increase risk for neurodegenerative disease are in mitochondrial-relevant genes[19,87,88] and microglia themselves are also highly implicated in shaping risk for and progression of neurodegeneration.

Several recent studies have begun investigating links between microglial mitochondria and neurodegeneration, but more research is needed. Microglia deficient in mitochondrial complex I activity induced glial inflammation, synapse loss and premature death in juvenile mice[35] but, conversely, blocking complex I activity was neuroprotective in an EAE-model of multiple sclerosis[36]. Similarly, age- and disease model-dependent findings have emerged using models of Alzheimer's disease. In 5x FAD mice, microglial deletion of a subunit of complex III resulted in increased microglial coverage of amyloid beta plaques and decreased plaque number[37], while deletion of microglial mitochondrial translocator protein (TSPO) impaired microglial phagocytosis of amyloid beta in a different mouse model of Alzheimer's[38]. Future studies should delve into whether mitochondria-associated disease risk stems from brain region specific impact of mitochondrial function on neuroprotective vs. neurotoxic phenotypes of microglia.

Several limitations of our study are important to note. First, we carried out our studies using light microscopy and this limits the ability to determine if densely packed mitochondria remain distinct or are part of a larger, interconnected mitochondrial network. In microglial somas, this was particularly evident, and future studies using super-resolution approaches such as STED imaging will be needed to more clearly determine if there are changes degree of mitochondrial interconnectedness in microglial somas across brain regions, during aging, or following pathological challenges. A second limitation of our study is that border associated macrophages (BAMs) can also be labeled by Iba1 immunostaining and are expected to experience recombination and mitoGFP expression in *CX3CR1*$^{CreER/+}$*;mitoGFP* mice. As BAMs are primarily concentrated in the meninges and vascular interfaces and are significantly less abundant than microglia, we are confident that our results are focused on parenchymal microglia[89]. Nonetheless, future studies employing markers of BAMs can explicitly analyze the mitochondria of BAMs and identify similarities and differences of BAM and microglial mitochondria and how these organelles regulate cell function.

Important future directions for this work and for the field also include deeper investigation of whether there are sex differences in microglial mitochondrial function. Both male and female mice were included in our study and we did not observe clear sex differences in most analyses of mitochondrial number, elongation, and remodeling following LPS challenge (**Fig. S9**). However, we did observe potential elevations of mitochondrial mass in microglia from female mice compared to microglia from male mice (**Fig. S9A**). Sex differences in microglial function are increasingly recognized in multiple contexts including neurodevelopment and neurodegenerative disease[90] and this will be an important area to explore further. Finally, mitochondria are highly complex organelles with numerous functions beyond ATP production. Our study provides insight into how these organelles align with key physiological properties of microglia as well as their attributes during responses to CNS insults. To expand upon this work and continue to elucidate how mitochondria impact microglial attributes and functions, we need to develop more tools that allow cell-specific manipulation of discrete facets of mitochondrial function such as calcium buffering, lipid metabolism, ROS handling, and interactions with other organelles.

METHODS

Mouse lines

C57Bl6 WT mice were obtained from the NIA Aged Rodent Colony and housed in the UCLA vivarium for at least one month before experiments. *CX3CR1*$^{CreER/+}$ mice were originally obtained from Jackson Labs (stock #025524) and subsequently maintained in our colony[41]. *Rosa26-lsl-mito-GFP* mice (*mitoGFP* mice) were obtained from Dr. Jeremy Nathans (Johns Hopkins University) and are available at Jackson Labs (stock #021429). These mice enable cre-dependent expression of GFP that is fused to an N-terminal signal derived from mouse cytochrome c oxidase, subunit VIIIa, enabling specific localization to mitochondria[40]. *Ai14* TdTomato reporter mice were obtained from Jackson Labs (stock #007914) and subsequently maintained in our colony[46]. Mice used for experiments were heterozygous for these transgenes. *Tfam*$^{fl/fl}$ floxed mice were obtained from Jackson Laboratories and have *loxP* sites flanking exons 6-7 of the transcription factor A, mitochondrial (*Tfam*) gene (stock #026123)[75]. These mice were crossed to the *CX3CR1*^{CreER} mice with a final breeding strategy to generate *CX3CR1*^{CreER}*;Tfam*$^{fl/fl}$ and *CX3CR1*^{CreER}*;Tfam*$^{+/+}$ littermate controls. In all experiments, balanced numbers of male and female mice were used. Mice were housed in normal light/dark cycle and had ad libitum access to food and water. All experiments were performed in strict accordance to an animal use protocol (ARC-2018-103) approved by the Animal Care and Use Committees at UCLA.

Tamoxifen Injections

In general, experiments were carried out without treating mice with tamoxifen. For select experiments as noted, 4-Hydroxytamoxifen (H7904-25mg, 95% pure z-isomer) was dissolved at 20 mg/mL in ethanol. For injections preparation, 4-OHT was redissolved in ethanol and diluted in a 1:4 mixture of castor oil:sunflower seed oil (Sigma, Cat #s 259853 and S5007) to give a final concentration of 1mg/kg. *CX3CR1*$^{CreER/+}$*;mitoGFP* mice at 3-4 mos received intraperitoneal injections of 4-OHT or vehicle (oil mixture) twice a day for 3 days at 1mg/kg. Mice were euthanized 3 weeks later for immunohistochemistry and flow cytometry. *CX3CR1*$^{CreER/+}$*;mitoGFP;Tfam*$^{fl/fl}$ mice and *CX3CR1*$^{CreER/+}$*;Tfam*$^{fl/fl}$ at 3-4 mos received injections of 4-Hydroxytamoxifen twice a day for 3 days at 1mg/kg. The mice were housed for 2 months after injections to allow for turnover of long-lived mitochondrial proteins[76,91]. Mice were then euthanized for immunohistochemistry or flow cytometry.

Lipopolysaccharide Injections

CX3CR1$^{CreER/+}$*;mitoGFP* and *CX3CR1*$^{CreER/+}$*;mitoGFP;Tfam*$^{fl/fl}$ *mice* 3 to 7 months (mos) of age received single intraperitoneal injections of 1mg/kg of Lipopolysaccharide (LPS) (Millipore Sigma, strain O55:B5, cat# L2880-25MG) or saline. All injections were performed around ~10am. For immunohistochemistry, mice were deeply anesthetized via isoflurane inhalation and transcardially perfused with 1M phosphate buffered saline (PBS; pH 7.4) followed by ice-cold 4% paraformaldehyde (PFA) in 1M PBS. For flow cytometry, mice were deeply anesthetized via isoflurane inhalation and transcardially perfused with 10 mL of chilled 1M PBS. Timepoints for experiments were 4hrs, 12 hrs or 24hrs post-injection.

Tissue collection and immunohistochemistry

Mice were deeply anesthetized via isoflurane inhalation and transcardially perfused with 1M PBS followed by ice-cold 4% PFA in 1M PBS. Brain tissue was isolated and postfixed in PFA for ~4hrs at 4°C and then stored in 1M PBS with 0.1% sodium azide until sectioning. Coronal brain sections were prepared using a vibratome at 60µm thickness. For immunostaining, free-floating brain sections were washed with 1M PBS (5 min) and then permeabilized and blocked in a

solution of 2% bovine serum albumin (BSA) and 3% normal donkey serum (NDS) and 0.01% of Triton-X for 2 hrs with rotation at room temperature. Sections were then incubated overnight with primary antibodies prepared in 2% bovine serum albumin (BSA) and 3% normal donkey serum (NDS) at 4°C with rotation. Sections from aged mice were incubated in TrueBlack lipofuscin autofluorescence quencher, (5%; Biotium cat: 23007) for 60 s followed by a 3x5 min rinse in 1M PBS prior to incubation with primary antibodies. Following primary antibody incubation, sections were washed 3x with 1M PBS and then incubated with secondary antibodies prepared in 2% bovine serum albumin (BSA) and 3% normal donkey serum (NDS) at room temperature for 2 hrs with rotation. This was followed by washes in 1M PBS (3x) with a second wash containing 1:4000 dilution of DAPI in 1M PBS. Sections were mounted using Aqua-Poly/Mount (Polysciences cat: 18606) and cover-slipped. Primary antibodies used include: rabbit anti- Iba1 (1:800; Wako, catalog #019-19741), rat anti-CD68 (1:200; clone FA11, AbD Serotec, catalog #MCA1957), chicken anti-TH (1:500; Aves, catalog #TYH). Secondary antibody combinations include rabbit AlexaFluor-647, chicken AlexaFluor-594, rat AlexaFluor-594, or chicken AlexaFluor-405 (used at 1:1000; all raised in donkey; Jackson ImmunoResearch Laboratories). For each set of analyses, three brain sections containing nucleus accumbens (NAc) and prefrontal cortex (PFC) and three brain sections containing ventral tegmental area (VTA) were chosen from each mouse. Brain sections were selected based on well-defined anatomical parameters and were matched for anterior-posterior location.

Confocal image acquisition and analysis

Fixed tissue slides were imaged using a Zeiss LSM880 or Zeiss LSM700 confocal microscope. Within the NAc, images were acquired at the boundary between core and shell (identified anatomically) and include both subregions. In the VTA, images captured were medial to the medial lemniscus. For quantification of MitoGFP recombination within microglia, stacks of confocal images (z-stacks) with a z interval of 1 µm were taken using a 20x objective and imported into ImageJ software for analysis. Maximum intensity projections were counted manually for the % of microglia exhibiting MitoGFP expression. For 3D volumetric reconstruction of microglia and mitochondria, confocal z-stacks were acquired with a 63x objective and z interval of 0.3 µm and imported into Imaris (Bitplane) software for analysis. The surface reconstruction module was used for volumetric reconstruction of mitochondria and microglia within the entire field of view (FOV). Measures of the average volume of individual mitochondria, mitochondrial sphericity (degree of circularity, with 1 representing a perfect circle), and aspect ratio (longest axis of mitochondria / shortest axis of mitochondria) were generated within the Imaris surfaces module and exported for graphing and statistical testing. For FOV based analyses, two or three images from separate brain sections were analyzed per mouse to obtain an average value for that mouse. 3 to 7 mice were analyzed per brain region, per age and/or per condition. In some cases, further analysis of individual microglia was carried out by selecting Imaris surfaces from an individual cell and the mitochondria within that cell. In these cases, 4-6 cells were analyzed per mouse. To select individual microglia for full 3D morphological reconstruction in *MG-mitoGFP;Ai14* mice, the brain region of interest was located and centered using only TH staining and anatomical landmarks with 20x objectives. After switching to 63x objectives, TdTom+mitoGFP+ microglia within that field of view were imaged. Slight X-Y adjustments were made, if needed, to bring a TdTom+mitoGFP+ microglial cell away from the edge of the FOV to avoid truncating processes. Cells were excluded from reconstruction if their somas fell near the top or bottom edge of the brain slice rather than being situated near the middle of the z-stack. The Imaris filament tracer module was used for reconstruction and

analysis of branching morphology of individual cells and surfaces were used to reconstruct mitochondria as described above. 1 or 2 cells were reconstructed per FOV per brain region, yielding 3-6 morphologically reconstructed cells per mouse. The Imaris filament tracer tool was also used for Sholl analysis, where each concentric circle was 1 µm apart. For analysis of mitoGFP signal intensity in *MG-mitoGFP-TFAMKO* and *MG-mitoGFP* control mice, mean fluorescence intensities for each individual, Imaris-reconstructed mitochondria in a field of view were extracted. Mean fluorescence intensity values for all reconstructed mitochondria from one mouse were then pooled (n=3 FOVs per mouse per brain region) and a cumulative distribution plot for that mouse and brain region was generated. Cumulative distribution plots from all mice from one genotype and brain region were then averaged to generate an average cumulative distribution for that group.

Acute brain slice preparation

CX3CR1 $^{CreER/+}$*; mitoGFP* or *CX3CR1* $^{CreER/+}$*; mitoGFP ; Ai14* mice at 1.5 to 2.5 months were anesthetized with isoflurane and perfused transcardially with 10 mL of oxygenated, ice-cold N-methyl-D-glucamine (NMDG)-based solution containing the following (in mM): 92 NMDG, 20 HEPES, 30 $NaHCO_3$, 1.2 NaH_2PO_4, 2.5 KCl, 5 sodium ascorbate, 3 sodium pyruvate, 2 thiourea, 10 $MgSO_4$, and 0.5 $CaCl_2$, 10 glucose, pH 7.4 (310 mOsm). Brains were then rapidly dissected free and horizontal midbrain sections (230 µm thick) and coronal forebrain sections (300 µm thick) were prepared using a vibratome in ice cold NMDG-based cutting solution bubbled continuously with 95% O_2 / 5% CO_2. Following sectioning, sections were transferred to a holding chamber containing NMDG solution at 34 ^{o}C for 5 min and then transferred to artificial cerebrospinal fluid (aCSF) solution at room temperature for 30 min recovery containing the following (in mM): 125 NaCl, 2.5 KCl, 1.25 NaH_2PO_4•$2H_2O$, 1 $MgCl_2$•$6H_2O$, 26 $NaHCO_3$, 11 Glucose and 2.4 $CaCl_2$•$2H_2O$ and bubbled continuously with 95% O_2 / 5% CO_2.

Acute brain slice multiphoton imaging

Acute brain slices from NAc and VTA were imaged using a Leica Stellaris 8 Dive, multiphoton microscope equipped with a Coherent Chameleon Ultra II laser and a Leica 25x/1.00 NA W motCORR objective. During video acquisition, acute brain slices were continuously perfused with aCSF bubbled with 95% O_2 / 5% CO_2. Videos were acquired at least 60 µm below the surface of the slice and video acquisition was carried out within 1-3 hours after sectioning. For analysis of microglial mitochondria only in *CX3CR1* $^{CreER/+}$*; mitoGFP* mice, an excitation wavelength of 930 nm was used and GFP was detected via a non-descanned detector (464 - 542nm). For analysis of microglial mitochondria and microglial cell process motility in *CX3CR1* $^{CreER/+}$*; mitoGFP ; Ai14* mice, an excitation wavelength of 930 nm was used, and GFP and TdTom signals were detected simultaneously via two non descanned detectors (detector 1: 463 – 537nm, detector 2: 558 - 668nm). Stacks of images encompassing entire microglial cells (z-step interval 1 µm) were acquired at 0.02Hz (for mitochondrial motility only) and .008Hz (mitochondrial motility + microglial cell process motility). To induce a focal laser lesion, exposure to high power illumination of 750nm for 10 seconds was applied 60 µm below the surface with maximal zoom in the space between 4-5 GFP+TdTom+ microglial cells. Imaging of microglia and their mitochondria post lesion was then carried out as described above.

Analysis of microglial and mitochondrial motility

To analyze microglial and mitochondrial motility, 3Dmorph, a previously published automated analysis pipeline by York et al.[92], was adapted for 2D analysis. Movies were pre-processed in ImageJ. Pre-processing included: background subtraction, median filter, drift correction (MultiStackReg ImageJ plugin), and bleach correction (Histogram matching ImageJ plugin). Individual cells were highlighted by ROI of maximum projections at each time point and the signal outside of ROI was removed. The adapted 3D morph script was applied to the final 2D movie to determine added/subtracted pixels, total pixels changed, and the area of TdTomato (microglia) and GFP (mitochondria) channels. To calculate microglial and mitochondrial motility, the total number of pixels altered during a 10-minute interval were normalized to the total number of pixels making up the cell (cell area). For quantification focused on individual microglial branches, preprocessed videos were cropped to isolate entire primary branches of the cell from the point at which the primary branch connects to the cell soma out to terminal endings of branches emanating from that primary process. Analysis and quantification were then carried out in the same manner as for entire cells. Mitochondrial mass of whole microglia or primary branching processes was calculated as GFP area divided by TdTomato area in final frame. Morphological complexity of microglia was analyzed using Sholl analysis through the Simple Neurite Tracer plugin in ImageJ[42]. Each concentric circle was 1 µm apart, like the morphological analysis conducted in fixed tissue. Values from Sholl analysis of cell branching in the first and last frame of 10-minute videos were averaged to obtain an overall assessment of cell complexity throughout the imaging period. To analyze mitochondrial motility in 3D, additional analyses were carried out within Imaris (Bitplane) Software. The surface reconstruction module was used to create surfaces for GFP+ mitochondria in microglial cell processes where individual mitochondria can be easily tracked; microglial somas contain large mitochondrial networks, complicating tracking of individual mitochondria. 4D movement tracks were then generated for each reconstructed mitochondrion. Some manual editing of tracks was performed to ensure accurate tracking of reconstructed mitochondria across time. 3D positional information at the start and end of 10 minute videos was used to calculate displacement of individual mitochondria. Individual mitochondrial displacements were averaged per cell to obtain average mitochondrial displacement within individual microglia. The volume for individual mitochondria was averaged across the initial frame and the final frame and volume of all mitochondria in a cell was summed to obtain the mitochondrial volume for each microglial cell.

Analysis of laser lesion response

Videos were preprocessed in ImageJ for background subtraction, median filter, maximum projection, and thresholding. Using an analysis strategy similar to that employed by others in the field[50,51], circular ROIs were used to create three rings within images at defined times post lesion (0, 5, 10 and 20 minutes), with the first ring enclosing the lesion, the second ring at 15 µm from the first, and the third ring at 30 µm from the first. ROI rings were used as masks to extract pixels within each ring at each time point and the measure function was used to extract ring area and percent of area covered by thresholded pixels. Percent change of pixels within a ring was calculated as initial pixels minus final pixels divided by initial pixels.

Tissue dissociation and flow cytometry

2-4mo, 12-13mo, and 16-18mo WT, *CX3CR*$^{CreER/+}$*;mitoGFP* and *CX3CR1*$^{CreER/+}$*;Tfam*$^{fl/fl}$ mice were deeply anesthetized with isoflurane and transcardially perfused with 10mL of chilled 1M

PBS. The brain was rapidly removed, cut coronally with a razor blade using anatomical landmarks and midbrain and striatum were dissected free. Samples were thoroughly minced with a razor blade on a chilled glass surface and transferred to 1.7mL tubes containing chilled 1mL Hibernate A Low-Fluorescence (BrainBits, Half100). Samples were then mechanically dissociated using gentle sequential trituration with fire-polished glass pipettes of decreasing diameter. Cell suspensions were pelleted via centrifugation and resuspended in 1M PBS + Debris Removal Solution (Miltenyi, 130-109-398). Debris removal was carried out according to the manufacturer's instructions. Following debris removal, samples were resuspended in small volumes of 1M PBS and incubated with primary antibodies on ice for 20min. Tetramethylrhodamine (TMRM) (Biotium, 70017) was used in some experiments to assess mitochondrial membrane potential. For these experiments, samples incubated with TMRM 50nM for 20 min at room temperature, prior to antibody incubation. Following incubation, samples were washed with 1xPBS and filtered through a 35μm filter (Falcon, 352235) prior to sorting. With the exception of TMRM incubation, throughout the experiment, samples were kept at 4°C. Samples were sorted using a FACS Aria I cell sorter (BD Biosciences). The population of cells containing microglia could be readily identified based on forward scattering (FSC) and side scattering (SSC) properties. A gating strategy based on FSC and SSC width and height was used to select single cells and reduce dead cells and doublets. Microglial cells within this population were then identified and sorted based on combinations of microglial antibodies. Antibody combinations used included anti-CD45 (1:400; Biolegend, 147703), anti-P2RY12 (1:500; Biolegend, 848005), and anti-CX3CR1 (1:800; Biolegend, 149023). Microglia from *CX3CR1*$^{CreER/+}$*;mitoGFP* mice were further gated from microglial antibodies to sort GFP+ cells. Placement of gates was verified using unstained samples as well as single color controls and Fluorescence Minus One (FMOs) controls. Gated Microglia were FACS sorted into 1.7mL tubes containing 50µl Pico Pure RNA extraction buffer and, following the sort, samples were incubated at 42°C for 30 min, and stored in RNase-free tubes at -80°C until further processing. Total sample processing time from brain dissection to completion of FACS purification ranged from 2-4hrs depending on the sort order of individual samples. Samples were collected in batches with each day of sorting including a young adult, saline injected, or TFAM$^{+/+}$ control mouse. Sort order of samples from specific ages, brain regions, treatment conditions, or genotypes was interleaved to avoid introduction of bias related to tissue processing length. FACS-isolation itself was carried out at 4°C. FACS-isolation of all samples for a given set of experiments was completed prior to downstream processing to allow simultaneous RNA isolation and cDNA preparation as described below.

Flow cytometry analyses

FCS files from sorting experiments were imported into FlowJo software for additional analyses of flow cytometry data. After placement of gates as described above, median fluorescence intensity measures were exported for populations of interest. Graphing and statistical analyses of MFI values were performed in OriginPro. To examine TMRM values normalized for mitochondrial volume / abundance, TMRM signal for each individual cell in a given sample was normalized to mitoGFP signal for that cell. Median values for this TMRM/mitoGFP measure were then calculated across all cells for a given sample. In some experiments, fluorescence signals across the entire population of cells from one sample were examined via cumulative distribution plots. For these analyses, a cumulative distribution plot was generated for each sample. Cumulative distribution curves from all samples in a group were then averaged to generate an average plot for that group.

RNA Extraction and qPCR

Total RNA was extracted from sorted cells using Pico Pure RNA isolation kit (Arcturus Bioscience) according to the manufacturer's instructions. Single strand cDNAs were synthesized using Superscript III first-strand cDNA synthesis kit (Invitrogen, 18080051), according to the manufacturer's protocol. Samples were subjected to PreAmplification-RT-PCR. TaqMan PreAmp Master Mix Kit was used for cDNA preamplification (Cat# 4391128; Applied Biosystems, Life Technologies), using pooled primer mixes of 20x dilution of TaqMan Gene Expression Assay and 80 nM of custom-designed primer sets. cDNAs were pre-amplified in an Veriti 96-Well Fast Thermal Cycler (ThermoFisher Scientific, 4375305) using the program: 95°C hold for 10 min, 14 cycles of 90°C denaturation for 15 s, and 60°C annealing and extension for 4 min. Pre-amplification PCR products were immediately diluted five times with molecular biology grade water and stored at -20°C, or immediately processed for RT-PCR. For qPCR analysis of gene expression, single plex qPCR assays were performed on technical duplicates using TaqMan probes for each gene target or for endogenous control gene (*Gapdh* for LPS experiments, *Gusb* for *MG-TFAMKO/MG-mitoGFP-TFAMKO* experiments). TaqMan Advanced Fast PCR Master Mix was used (catalog #4444963; Invitrogen). To avoid amplification of any genomic DNA contamination, primers and probes that amplify across target gene exon–exon junctions were selected when possible. qPCRs reactions were run in a QuantStudio5 using the program: 95°C hold for 20 s, followed by 40 cycles of 95°C denaturation for 3 s, and 60°C annealing and extension for 30 s. Calculations of relative expression and expression fold change from Ct data were conducted according to User Bulletin #2 for ABI Prism 7900 Sequence Detection System. For each target gene, the average Ct value for the endogenous control gene (*Gapdh*/*Gusb*) was subtracted from the average Ct value for the target gene, to obtain ΔCt. The relative expression was then plotted as $2^{-\Delta Ct}$. ΔΔCt was obtained by subtracting the average ΔCt of the control group from the average ΔCt of a given sample. Expression fold change was then plotted as $2^{-\Delta\Delta Ct}$. Average ΔCt of the control group was calculated separately for STR and MB samples. All TaqMan Assays and custom primers/probes that were used are detailed in *Table S8*.

Statistical analyses

Statistical analysis was performed in OriginPro, Matlab, and R. Heatmaps were generated in R using the ComplexHeatmap package by Gu Z et al[93]. PCAs were generated in R using the ggplot2 package by Wickham H[94]. Robust regression with False Discovery Rate control analyses were performed in R or Matlab. Cumulative distribution plots were analyzed for significant differences using Kolmogorov-Smirnov tests in OriginPro or Matlab. All graphed values are shown as mean ± SEM. Statistical details of experiments (statistical tests used, exact value of N, what N represents) can be found in results and the figure legends. In general, statistical significance was assessed using one- or two-way ANOVA. Post hoc comparisons were conducted using Student's t-test with Bonferroni correction for multiple comparisons. Data are sufficiently normal and variance within groups is sufficiently similar for use of parametric tests. 2 tailed paired t-tests were used to compare trends across two different brain regions within individual mice. Statistical significance was considered if $P<0.05$. Asterisks were used to delineate statistical significance.

Data availability

Source data are provided with this paper. Source data used to prepare all figures in this study have been deposited in FigShare database. Raw data files are available to researchers wishing to carry out additional analyses or validation analyses for non-commercial purposes. Access to raw data files can be obtained by contacting Dr. Lindsay De Biase, ldebiase@mednet.ucla.edu.

Code availability

MatLab code used for analysis of microglial motility (slightly modified from original 3DMorph code) is available on github.

References

1. Li, Q. & Barres, B. A. Microglia and macrophages in brain homeostasis and disease. *Nat. Rev. Immunol.* **18**, 225–242 (2018).
2. Sierra, A., Paolicelli, R. C. & Kettenmann, H. Cien Años de Microglía: Milestones in a Century of Microglial Research. *Trends Neurosci.* **42**, 778–792 (2019).
3. Matsudaira, T. & Prinz, M. Life and death of microglia: Mechanisms governing microglial states and fates. *Immunol. Lett.* **245**, 51–60 (2022).
4. Ransohoff, R. M. A polarizing question: do M1 and M2 microglia exist? *Nat. Neurosci.* **19**, 987–991 (2016).
5. Paolicelli, R. C. *et al.* Microglia states and nomenclature: A field at its crossroads. *Neuron* **110**, 3458–3483 (2022).
6. Grabert, K. *et al.* Microglial brain region−dependent diversity and selective regional sensitivities to aging. *Nat. Neurosci.* **19**, 504–516 (2016).
7. Stowell, R. D. *et al.* Cerebellar microglia are dynamically unique and survey Purkinje neurons in vivo. *Dev. Neurobiol.* **78**, 627–644 (2018).
8. Böttcher, C. *et al.* Human microglia regional heterogeneity and phenotypes determined by multiplexed single-cell mass cytometry. *Nat. Neurosci.* **22**, 78–90 (2019).
9. De Biase, L. M. & Bonci, A. Region-Specific Phenotypes of Microglia: The Role of Local Regulatory Cues. *The Neuroscientist* **25**, 314–333 (2019).

10. Ayata, P. *et al.* Epigenetic regulation of brain region-specific microglia clearance activity. *Nat. Neurosci.* **21**, 1049–1060 (2018).
11. Hanamsagar, R. & Bilbo, S. D. Environment matters: microglia function and dysfunction in a changing world. *Curr. Opin. Neurobiol.* **47**, 146–155 (2017).
12. Salter, M. W. & Stevens, B. Microglia emerge as central players in brain disease. *Nat. Med.* **23**, 1018–1027 (2017).
13. Wolf, S. A., Boddeke, H. W. G. M. & Kettenmann, H. Microglia in Physiology and Disease. *Annu. Rev. Physiol.* **79**, 619–643 (2017).
14. Gleichman, A. J. & Carmichael, S. T. Glia in neurodegeneration: Drivers of disease or along for the ride? *Neurobiol. Dis.* **142**, 104957 (2020).
15. Ceasrine, A. M. & Bilbo, S. D. Dietary fat: a potent microglial influencer. *Trends Endocrinol. Metab. TEM* **33**, 196–205 (2022).
16. Sequeira, M. K. & Bolton, J. L. Stressed Microglia: Neuroendocrine-Neuroimmune Interactions in the Stress Response. *Endocrinology* **164**, bqad088 (2023).
17. Wangler, L. M. & Godbout, J. P. Microglia moonlighting after traumatic brain injury: aging and interferons influence chronic microglia reactivity. *Trends Neurosci.* **46**, 926–940 (2023).
18. Cheray, M. & Joseph, B. Epigenetics Control Microglia Plasticity. *Front. Cell. Neurosci.* **12**, 243 (2018).
19. Shen, K. *et al.* Mitochondria as Cellular and Organismal Signaling Hubs. *Annu. Rev. Cell Dev. Biol.* **38**, 179–218 (2022).
20. Collier, J. J., Oláhová, M., McWilliams, T. G. & Taylor, R. W. Mitochondrial signalling and homeostasis: from cell biology to neurological disease. *Trends Neurosci.* **46**, 137–152 (2023).
21. Picard, M. & Shirihai, O. S. Mitochondrial signal transduction. *Cell Metab.* **34**, 1620–1653 (2022).

22. Tan, J. X. & Finkel, T. Mitochondria as intracellular signaling platforms in health and disease. *J. Cell Biol.* **219**, e202002179 (2020).
23. Kolliniati, O., Ieronymaki, E., Vergadi, E. & Tsatsanis, C. Metabolic Regulation of Macrophage Activation. *J. Innate Immun.* **14**, 51–68 (2021).
24. Mills, E. L. & O'Neill, L. A. Reprogramming mitochondrial metabolism in macrophages as an anti-inflammatory signal. *Eur. J. Immunol.* **46**, 13–21 (2016).
25. Mills, E. L. *et al.* Succinate Dehydrogenase Supports Metabolic Repurposing of Mitochondria to Drive Inflammatory Macrophages. *Cell* **167**, 457-470.e13 (2016).
26. Diskin, C. & Pålsson-McDermott, E. M. Metabolic Modulation in Macrophage Effector Function. *Front. Immunol.* **9**, 270 (2018).
27. Ramond, E., Jamet, A., Coureuil, M. & Charbit, A. Pivotal Role of Mitochondria in Macrophage Response to Bacterial Pathogens. *Front. Immunol.* **10**, 2461 (2019).
28. Wang, X.-L. & Li, L. Microglia Regulate Neuronal Circuits in Homeostatic and High-Fat Diet-Induced Inflammatory Conditions. *Front. Cell. Neurosci.* **15**, (2021).
29. Afroz, S. F. *et al.* Mitochondrial dynamics in macrophages: divide to conquer or unite to survive? *Biochem. Soc. Trans.* **51**, 41–56 (2023).
30. De Biase, L. M. *et al.* Local Cues Establish and Maintain Region-Specific Phenotypes of Basal Ganglia Microglia. *Neuron* **95**, 341-356.e6 (2017).
31. Maes, M. E. *et al.* Mitochondrial network adaptations of microglia reveal sex-specific stress response after injury and UCP2 knockout. *iScience* **26**, 107780 (2023).
32. Bordt, E. A. *et al.* Gonadal hormones impart male-biased behavioral vulnerabilities to immune activation via microglial mitochondrial function. *Brain. Behav. Immun.* **115**, 680–695 (2024).
33. Baik, S. H. *et al.* A Breakdown in Metabolic Reprogramming Causes Microglia Dysfunction in Alzheimer's Disease. *Cell Metab.* **30**, 493-507.e6 (2019).

34. March-Diaz, R. *et al.* Hypoxia compromises the mitochondrial metabolism of Alzheimer's disease microglia via HIF1. *Nat. Aging* **1**, 385–399 (2021).
35. Mora-Romero, B. *et al.* Microglia mitochondrial complex I deficiency during development induces glial dysfunction and early lethality. *Nat. Metab.* **6**, 1479–1491 (2024).
36. Peruzzotti-Jametti, L. *et al.* Mitochondrial complex I activity in microglia sustains neuroinflammation. *Nature* **628**, 195–203 (2024).
37. Stoolman, J. S. *et al.* Mitochondrial respiration in microglia is essential for response to demyelinating injury but not proliferation. *Nat. Metab.* **6**, 1492–1504 (2024).
38. Fairley, L. H. *et al.* Mitochondrial control of microglial phagocytosis by the translocator protein and hexokinase 2 in Alzheimer's disease. *Proc. Natl. Acad. Sci. U. S. A.* **120**, e2209177120 (2023).
39. Fecher, C. *et al.* Cell-type-specific profiling of brain mitochondria reveals functional and molecular diversity. *Nat. Neurosci.* **22**, 1731–1742 (2019).
40. Agarwal, A. *et al.* Transient Opening of the Mitochondrial Permeability Transition Pore Induces Microdomain Calcium Transients in Astrocyte Processes. *Neuron* **93**, 587-605.e7 (2017).
41. Yona, S. *et al.* Fate Mapping Reveals Origins and Dynamics of Monocytes and Tissue Macrophages under Homeostasis. *Immunity* **38**, 79–91 (2013).
42. Hope, K. T., Hawes, I. A., Moca, E. N., Bonci, A. & De Biase, L. M. Maturation of the microglial population varies across mesolimbic nuclei. *Eur. J. Neurosci.* **52**, 3689–3709 (2020).
43. Moca, E. N. *et al.* Microglia Drive Pockets of Neuroinflammation in Middle Age. *J. Neurosci.* **42**, 3896–3918 (2022).
44. Faust, T. E. *et al.* A comparative analysis of microglial inducible Cre lines. *Cell Rep.* **42**, 113031 (2023).

45. Bedolla, A. M. *et al.* A comparative evaluation of the strengths and potential caveats of the microglial inducible CreER mouse models. *Cell Rep.* **43**, 113660 (2024).

46. Madisen, L. *et al.* A robust and high-throughput Cre reporting and characterization system for the whole mouse brain. *Nat. Neurosci.* **13**, 133–140 (2010).

47. Nimmerjahn, A., Kirchhoff, F. & Helmchen, F. Resting Microglial Cells Are Highly Dynamic Surveillants of Brain Parenchyma in Vivo. *Science* **308**, 1314–1318 (2005).

48. Chiurazzi, M., Di Maro, M., Cozzolino, M. & Colantuoni, A. Mitochondrial Dynamics and Microglia as New Targets in Metabolism Regulation. *Int. J. Mol. Sci.* **21**, 3450 (2020).

49. Etienne, F. *et al.* Two-photon Imaging of Microglial Processes' Attraction Toward ATP or Serotonin in Acute Brain Slices. *J. Vis. Exp. JoVE* (2019) doi:10.3791/58788.

50. Davalos, D. *et al.* ATP mediates rapid microglial response to local brain injury in vivo. *Nat. Neurosci.* **8**, 752–758 (2005).

51. Lou, N. *et al.* Purinergic receptor P2RY12-dependent microglial closure of the injured blood-brain barrier. *Proc. Natl. Acad. Sci. U. S. A.* **113**, 1074–1079 (2016).

52. Bernier, L.-P. *et al.* Microglial metabolic flexibility supports immune surveillance of the brain parenchyma. *Nat. Commun.* **11**, 1559 (2020).

53. Norden, D. M., Trojanowski, P. J., Villanueva, E., Navarro, E. & Godbout, J. P. Sequential activation of microglia and astrocyte cytokine expression precedes increased Iba-1 or GFAP immunoreactivity following systemic immune challenge. *Glia* **64**, 300–316 (2016).

54. Nair, S. *et al.* Lipopolysaccharide-induced alteration of mitochondrial morphology induces a metabolic shift in microglia modulating the inflammatory response in vitro and in vivo. *Glia* **67**, 1047–1061 (2019).

55. Park, J. *et al.* Mitochondrial dynamics modulate the expression of pro-inflammatory mediators in microglial cells. *J. Neurochem.* **127**, 221–232 (2013).

56. Orihuela, R., McPherson, C. A. & Harry, G. J. Microglial M1/M2 polarization and metabolic states. *Br. J. Pharmacol.* **173**, 649–665 (2016).

57. Hu, Y. *et al.* mTOR-mediated metabolic reprogramming shapes distinct microglia functions in response to lipopolysaccharide and ATP. *Glia* **68**, 1031–1045 (2020).
58. O'Neill, L. A. J., Kishton, R. J. & Rathmell, J. A guide to immunometabolism for immunologists. *Nat. Rev. Immunol.* **16**, 553–565 (2016).
59. Van den Bossche, J. *et al.* Mitochondrial Dysfunction Prevents Repolarization of Inflammatory Macrophages. *Cell Rep.* **17**, 684–696 (2016).
60. Hoogland, I. C. M. *et al.* Microglial Activation After Systemic Stimulation With Lipopolysaccharide and Escherichia coli. *Front. Cell. Neurosci.* **12**, 110 (2018).
61. Picard, M., Shirihai, O. S., Gentil, B. J. & Burelle, Y. Mitochondrial morphology transitions and functions: implications for retrograde signaling? *Am. J. Physiol.-Regul. Integr. Comp. Physiol.* **304**, R393–R406 (2013).
62. Chan, D. C. Mitochondrial Dynamics and Its Involvement in Disease. *Annu. Rev. Pathol.* **15**, 235–259 (2020).
63. Su, É., Villard, C. & Manneville, J.-B. Mitochondria: At the crossroads between mechanobiology and cell metabolism. *Biol. Cell* **115**, e2300010 (2023).
64. Candlish, M. & Hefendehl, J. K. Microglia Phenotypes Converge in Aging and Neurodegenerative Disease. *Front. Neurol.* **12**, 660720 (2021).
65. Brawek, B., Skok, M. & Garaschuk, O. Changing Functional Signatures of Microglia along the Axis of Brain Aging. *Int. J. Mol. Sci.* **22**, 1091 (2021).
66. Niraula, A., Sheridan, J. F. & Godbout, J. P. Microglia Priming with Aging and Stress. *Neuropsychopharmacol. Off. Publ. Am. Coll. Neuropsychopharmacol.* **42**, 318–333 (2017).
67. Lima, T., Li, T. Y., Mottis, A. & Auwerx, J. Pleiotropic effects of mitochondria in aging. *Nat. Aging* **2**, 199–213 (2022).
68. Sun, N., Youle, R. J. & Finkel, T. The Mitochondrial Basis of Aging. *Mol. Cell* **61**, 654–666 (2016).

69. Chistiakov, D. A., Sobenin, I. A., Revin, V. V., Orekhov, A. N. & Bobryshev, Y. V. Mitochondrial aging and age-related dysfunction of mitochondria. *BioMed Res. Int.* **2014**, 238463 (2014).
70. Stillman, J. M. *et al.* Lipofuscin-like autofluorescence within microglia and its impact on studying microglial engulfment. *Nat. Commun.* **14**, 7060 (2023).
71. Fiebig, C. *et al.* Mitochondrial Dysfunction in Astrocytes Impairs the Generation of Reactive Astrocytes and Enhances Neuronal Cell Death in the Cortex Upon Photothrombotic Lesion. *Front. Mol. Neurosci.* **12**, 40 (2019).
72. Sterky, F. H., Lee, S., Wibom, R., Olson, L. & Larsson, N.-G. Impaired mitochondrial transport and Parkin-independent degeneration of respiratory chain-deficient dopamine neurons in vivo. *Proc. Natl. Acad. Sci. U. S. A.* **108**, 12937–12942 (2011).
73. Vernochet, C. *et al.* Adipose-specific deletion of TFAM increases mitochondrial oxidation and protects mice against obesity and insulin resistance. *Cell Metab.* **16**, 765–776 (2012).
74. Sörensen, L. *et al.* Late-onset corticohippocampal neurodepletion attributable to catastrophic failure of oxidative phosphorylation in MILON mice. *J. Neurosci. Off. J. Soc. Neurosci.* **21**, 8082–8090 (2001).
75. Larsson, N. G. *et al.* Mitochondrial transcription factor A is necessary for mtDNA maintenance and embryogenesis in mice. *Nat. Genet.* **18**, 231–236 (1998).
76. Fornasiero, E. F. *et al.* Precisely measured protein lifetimes in the mouse brain reveal differences across tissues and subcellular fractions. *Nat. Commun.* **9**, 4230 (2018).
77. Alshial, E. E. *et al.* Mitochondrial dysfunction and neurological disorders: A narrative review and treatment overview. *Life Sci.* **334**, 122257 (2023).
78. Norat, P. *et al.* Mitochondrial dysfunction in neurological disorders: Exploring mitochondrial transplantation. *NPJ Regen. Med.* **5**, 22 (2020).
79. Bame, X. & Hill, R. A. Mitochondrial network reorganization and transient expansion during oligodendrocyte generation. *Nat. Commun.* **15**, 6979 (2024).

80. Zehnder, T. *et al.* Mitochondrial biogenesis in developing astrocytes regulates astrocyte maturation and synapse formation. *Cell Rep.* **35**, 108952 (2021).

81. Ryu, K. W. *et al.* Cellular ATP demand creates metabolically distinct subpopulations of mitochondria. *Nature* **635**, 746–754 (2024).

82. Aryaman, J., Johnston, I. G. & Jones, N. S. Mitochondrial Heterogeneity. *Front. Genet.* **9**, 718 (2018).

83. Seager, R., Lee, L., Henley, J. M. & Wilkinson, K. A. Mechanisms and roles of mitochondrial localisation and dynamics in neuronal function. *Neuronal Signal.* **4**, NS20200008 (2020).

84. Degechisa, S. T., Dabi, Y. T. & Gizaw, S. T. The mitochondrial associated endoplasmic reticulum membranes: A platform for the pathogenesis of inflammation-mediated metabolic diseases. *Immun. Inflamm. Dis.* **10**, e647 (2022).

85. Pietramale, A. N., Bame, X., Doty, M. E. & Hill, R. A. Mitochondria are absent from microglial processes performing surveillance, chemotaxis, and phagocytic engulfment. *BioRxiv Prepr. Serv. Biol.* 2024.10.15.618505 (2024) doi:10.1101/2024.10.15.618505.

86. Sivagnanam, S., Mahato, P. & Das, P. An overview on the development of different optical sensing platforms for adenosine triphosphate (ATP) recognition. *Org. Biomol. Chem.* **21**, 3942–3983 (2023).

87. Harrington, J. S., Ryter, S. W., Plataki, M., Price, D. R. & Choi, A. M. K. Mitochondria in health, disease, and aging. *Physiol. Rev.* **103**, 2349–2422 (2023).

88. König, T. & McBride, H. M. Mitochondrial-derived vesicles in metabolism, disease, and aging. *Cell Metab.* **36**, 21–35 (2024).

89. Utz, S. G. *et al.* Early Fate Defines Microglia and Non-parenchymal Brain Macrophage Development. *Cell* **181**, 557-573.e18 (2020).

90. Han, J., Fan, Y., Zhou, K., Blomgren, K. & Harris, R. A. Uncovering sex differences of rodent microglia. *J. Neuroinflammation* **18**, 74 (2021).

91. Krishna, S. *et al.* Identification of long-lived proteins in the mitochondria reveals increased stability of the electron transport chain. *Dev. Cell* **56**, 2952-2965.e9 (2021).

92. York, E. M., Bernier, L.-P. & MacVicar, B. A. Microglial modulation of neuronal activity in the healthy brain. *Dev. Neurobiol.* **78**, 593–603 (2018).

93. Gu, Z., Eils, R. & Schlesner, M. Complex heatmaps reveal patterns and correlations in multidimensional genomic data. *Bioinforma. Oxf. Engl.* **32**, 2847–2849 (2016).

94. Wickham, H. *Ggplot2*. (Springer International Publishing, Cham, 2016). doi:10.1007/978-3-319-24277-4.

Acknowledgements

This work was supported by the Diana Jacobs Kalman Scholarship (American Federation on Aging Research scholarship to A.W.S), the Jennifer S. Buchwald Graduate Fellowship (UCLA Department of Physiology fellowship to K.E.), a University of California Office of the President Pre-Professoriate Fellowship (to K.E.), UCLA CARE Summer Undergraduate Fellowship (to C.C.), UCLA CARE Summer Undergraduate Fellowship (to K.M.), David Geffen School of Medicine at UCLA start-up funds (to L.M.D.) and a Stanley Fahn Junior Faculty Award (PF-SF-JFA-836586; Parkinson's Foundation Grant to L.M.D.). We thank the UCLA Eli and Edythe Broad Center of Regenerative Medicine and Stem Cell Research Flow Cytometry Core and the UCLA Jonsson Comprehensive Cancer Center and Center for AIDS Research Flow Cytometry Core for assistance with FACS-based experiments. We thank the UCLA Eli and Edythe Broad Center of Regenerative Medicine and Stem Cell Research Microscopy Core for access to and use of confocal microscopes and Imaris workstations. We thank Dr. Elaine Hsiao for the use of the Hsiao lab QuantStudio5 for qPCR experiments. We thank Dr. Fanny Etienne for assistance with training for multiphoton imaging experiments.

Author Contributions

K.E., A.W.S., and L.M.D. designed research; K.E., A.W.S., A.S., A.E., K.M., M.Y., and C.C. performed research; K.E., A.W.S., D.T.G., A.S., K.M., M.Y., and C.C. analyzed data; K.E., A.W.S., and L.M.D edited the paper, K.E. and A.W.S wrote the first draft of the paper, K.E. and A.W.S. wrote the paper; L.M.D supervised research

Competing Interests Statement

No competing interests.

FIGURE LEGENDS

FIGURE 1: Regional specialization of microglia is accompanied by regional differences in mitochondrial mass and number. (A) Schematic of transgenic crosses used to achieve GFP labeling of microglial mitochondria. **(B)** Representative high-magnification images from P60 *MG-mitoGFP* mice of NAc microglia (*Iba1*) and mitochondria (*GFP*); panels *at right* show 3D volumetric reconstructions of microglia (*transparent gray*) and mitochondria (*colored according to volume*). **(C-E)** Field of view (FOV) microglial volume (tissue coverage; *P = 0.003), FOV microglial mitochondrial mass (FOV mitochondrial volume / FOV microglial volume; *P = 0.001), and FOV microglial mitochondrial number (relative to FOV microglial volume; *P = 0.026) in NAc and VTA. Data points from the same mouse connected by lines (N = 7 mice, stats via two-tailed paired t-tests). **(F)** Representative confocal images of microglial cells in NAc and VTA expressing cytosolic TdTomato (TdTom) and mitochondrial targeted GFP (*MG-mitoGFP;Ai14* mice). Reconstruction of cell branching and 3D volumetric reconstruction of mitochondria in Imaris *at right*. **(G)** Total process length of individual microglia from PFC (N = 15 cells), NAc (N = 16 cells), and VTA (N = 15 cells). One-way ANOVA with Bonferroni correction, $F_{2,43} = 31.30$, P = 0.0001. *P<0.05. **(H)** Robust regression plots relating mitochondrial number and volume to total process length of individual microglia from PFC (R = 0.40 P = 0.17), NAc (R = 0.13 P = 0.42), and VTA (R = 0.56 P = 0.02). *P<0.05 **(I)** Sum of branch points of individual microglia from PFC, NAc, and VTA. One-way ANOVA with Bonferroni correction, $F_{2,43} = 36.73$, *P = 0.0001. *P<0.05. **(J)** Robust regression plots relating mitochondrial number and volume to morphological complexity (sum of branch points) of individual microglia from PFC (R = 0.17 P = 0.59), NAc (R = 0.45 P = 0.08), VTA (R = 0.49 P = 0.08). *P<0.05. Mice used for these experiments were not treated with 4-hydroxytamoxifen. Data for panels C, D, E, G, and I was plotted as mean +/- SEM. Source data for all graphs are provided as a Source Data file.

FIGURE 2: Mitochondrial abundance and mitochondrial motility are not strongly correlated with microglial tissue surveillance. (A) Representative images taken during multiphoton live imaging of VTA microglia (*TdTomato*) and their mitochondria (*GFP*) in acute brain sections from 1.5 -2mo old *MG-mitoGFP;Ai14* mice. **(B)** Example of microglial cell process extension indicated by *white arrow*. **(C)** Overall microglial motility in NAc and VTA during a 10- minute period. N = 14 NAc cells and N = 12 VTA cells, P = 0.659, two-tailed t-test. Data was plotted as mean +/- SEM. **(D)** Robust regression analysis relating mitochondrial volume (total volume in a cell averaged across time points) and microglial motility over a 10-minute period. N = 14 NAc cells, R = -0.42 P = 0.14 and N = 12 VTA cells, R = -0.19 P = 0.57. **(E)** Robust regression analysis relating mitochondrial mass and microglial motility over a 10-minute period. N = 14 NAc cells, R = -0.10 P = 0.49 and N = 12 VTA cells, R = 0.04 P = 0.98. **(F)** Representative examples of mitochondrial fission and fusion observed in microglia from *MG-mitoGFP* mice. **(G)** Raw fluorescence from multiphoton imaging (*left*) and 3D reconstruction of microglial mitochondria (*right*), colored by time. **(H)** Displacement of

individual mitochondria across cells over a 10-minute period. N = 116 NAc mitochondria and N = 134 VTA mitochondria. Box plot displaying median, 25-75 percentiles (box), and 5th and 95th percentiles (whiskers). **(I)** Robust regression analysis relating mitochondrial motility to microglial motility. N = 14 NAc cells, R = -0.07 P = 0.78 and N = 12 VTA cells, R = -0.06 P = 0.70. **(J)** Robust regression analysis relating mitochondrial motility *within* one primary microglial branch to motility of the primary branch itself. N = 55 primary branching processes from NAc microglia, R = 0.06 P = 0.91 and N = 46 primary branching processes from VTA microglia, R = 0.01 P = 0.75. Mice used for these experiments were not treated with 4-hydroxytamoxifen. Source data for all graphs are provided as a Source Data file.

FIGURE 3: Mitochondrial distribution is stable during early phases of microglial response to focal tissue injury. **(A)** Representative image from multiphoton live imaging of NAc microglia (*TdTomato*) and their mitochondria (*mitoGFP*) in an acute brain slice from young adult *MG-mitoGFP;Ai14* mouse prior to induction of focal laser injury. **(B)** TdTom+ microglia and GFP+ mitochondria from the same field of view as in *A* immediately following induction of focal laser lesion (T0). Ring 1 encompasses the primary lesion area, with *inner* and *outer* rings at 15 μm and 30 μm from ring 1, respectively. **(C-E)** TdTom+ microglia and GFP+ mitochondria from the same field of view as in *A* at 5, 10, and 20 min post laser lesions. **(F,G)** Percent change in TdTomato signal (microglial processes) within the outer and inner rings, respectively, relative to T0. *Outer ring* P = 0.73; *Inner ring* P = 0.07, One-way Anova with Repeated Measures and Bonferroni correction. **(H,I)** Percent change in GFP signal (microglial mitochondria) within the outer and inner rings, respectively, relative to T0. *Outer ring* P = 0.79; *Inner ring* P = 0.16, One-way Anova with Repeated Measures and Bonferroni correction. For data in *F-I*, N = 3 NAc acute brain sections from 3 mice (9 NAc acute brain sections total) and data was plotted as mean +/- SEM. Mice used for these experiments were not treated with 4-hydroxytamoxifen. Source data used to generate all graphs are provided as a Source Data file.

FIGURE 4: Response to inflammatory challenge (LPS) elicits rapid mitochondrial changes in microglia. (A) Schematic of experiment design (prepared in part with graphics from BioRender). 3-4mo *MG-MitoGFP* mice were injected with saline or lipopolysaccharide (LPS) prior to FACS isolation of STR/MB microglia and downstream qPCR analysis. **(B)** Heatmaps showing relative expression levels ($2^{-\Delta Ct}$) of key microglial function and mitochondrial function genes. Z-scores represent average gene expression across treatment groups and brain regions. See *Tables S1* and *S2* for Two-way ANOVAs and post hoc comparisons with Bonferroni correction. Treatment: * P < 0.05, ** P < 0.01, *** P < 0.001. Brain region difference: $ P < 0.05. (Saline STR N = 7 mice, Saline MB N = 7 mice, LPS 4hr STR N = 7 mice, LPS 4hr MB N = 6 mice, LPS 24hr STR N = 7mice, LPS 24hr MB N = 7 mice). **(C)** PC1 and PC2 of Principal Component Analysis of samples using only mitochondrial function genes. **(D)** Heatmaps

depicting the degree of correlation between expression levels of microglial function genes (pro-inflammatory - *Cd45*, *Il1β*, *Tnfα*; homeostatic - *Cx3cr1*, *P2ry12*, *Tgfβ1*) and mitochondrial function genes as determined by robust regression analysis with false discovery rate correction. See *Table S3* for R- and P-values. * $P < 0.05$, ** $P < 0.01$, *** $P < 0.001$. **(E)** Representative FACS contour plots showing TMRM and GFP fluorescence intensity of microglia from Saline, LPS 4hr, and LPS 24hr mice. **(F)** Median Fluorescence Intensity of GFP, TMRM (normalized to each cell's GFP to account for mitochondrial mass), and CD45 in STR and MB microglia from Saline (N = 7, squares), LPS 4hr (N = 7, triangles), and LPS 24hr (N = 7, circles) mice. One-way ANOVAs and post hoc comparisons with Bonferroni correction: GFP STR, $F_{(2,18)} = 25.06735$, $p < 0.0001$; GFP MB, $F_{(2,18)} = 29,85264$, $p < 0.0001$; TMRM STR, $F_{(2,18)} = 19.2316$, $p < 0.0001$; TMRM MB, $F_{(2,18)} = 6.61021$, $p = 0.00704$; CD45 STR, $F_{(2,18)} = 5.52274$, $p = 0.01348$; CD45 MB, $F_{(2,18)} = 2.99003$, $p = 0.07565$. * $P < 0.05$, ** $P < 0.01$, *** $P < 0.001$. Data was plotted as mean +/- SEM. Mice used for these experiments were not treated with 4 hydroxytamoxifen. Source data used to prepare all graphs are provided as a Source Data file.

FIGURE 5: Microglial responses to inflammatory challenge (LPS) are accompanied by mitochondrial elongation and increases in mitochondrial mass. **(A)** Representative images of NAc microglia (IBA1) and their mitochondria (GFP) from 3-4mo *MG-MitoGFP* mice injected with saline (*left*) or LPS 24hr (*right*). *White* and *yellow boxes* highlight microglial somas and cell processes shown at higher magnification in *lower panels*. **(B)** Field of view (FOV) microglial mitochondrial mass (FOV mitochondrial volume / FOV microglial cell volume) within NAc and VTA microglia of saline (*squares*) or LPS treated mice (*circles*); Two-way ANOVA with Bonferroni correction for post hoc comparisons: main effect of treatment, $F_{(1,17)} = 5.19787$, $P = 0.03579$; main effect of region, $F_{(1,17)} = 0.0713$, $P = 0.079266$. **(C)** FOV mitochondrial number (relative to FOV microglial cell volume) within NAc and VTA microglia of saline (*squares*) or LPS treated (*circles*) mice; Two-way ANOVA with Bonferroni correction for post hoc comparisons: main effect of treatment: $F_{(1,17)} = 0.23167$, $P = 0.63642$; main effect of region, $F_{(1,17)} = 0.05079$, $P = 0.82438$. **(D)** Average mitochondrial aspect ratio (longest axis / shortest axis) within NAc and VTA microglia of saline (*squares*) or LPS treated (*circles*) mice; Two-way ANOVA with Bonferroni correction for post hoc comparisons: main effect of treatment: main effect of treatment, $F_{(1,17)} = 10.19319$, $p = 0.00533$; main effect of region, $F_{(1,17)} = 0.26571$, $P = 0.61286$. Quantification for *B-D* from N = 5 saline-injected mice and N = 6 LPS-injected mice. Data for *B-D* was plotted as mean +/- SEM. *$P<0.05$, **$P<0.01$. Mice used for these experiments were not treated with 4 hydroxytamoxifen. Source data used to generate all graphs are provided as a Source Data file.

FIGURE 6: Microglial mitochondria undergo remodeling in middle- and late middle aged mice. (A) Representative images of NAc (*left*) and VTA (*right*) microglia (IBA1) and microglial mitochondria (GFP) from 2-3mo, 12-13mo, and 16-18mo *MG-MitoGFP* mice. Regions highlighted by *yellow boxes* shown at higher magnification in *lower panels*. **(B-C)** Field of view (FOV) mitochondrial mass, number, and aspect ratio of NAc and VTA microglia during aging, normalized to mean values from 2-3mo animals. 2-3mo (N = 7 mice), 12-13mo (N = 4 mice), and 16-18mo (N = 5 mice). One-way ANOVAs with Bonferroni correction for post hoc comparisons: mitochondrial mass NAc, $F_{(2,13)} = 0.43588$, P = 0.65581, mitochondrial number NAc, $F_{(2,13)} = 11.5342$, P = 0.00132, mitochondria aspect ratio NAc, $F_{(2,13)} = 2.54264$, P = 0.11695, mitochondrial mass VTA, $F_{(2,13)} = 1.47803$, P = 0.26401, mitochondrial number VTA, $F_{(2,13)} = 7.57294$, P = 0.0066, mitochondrial aspect ratio VTA, $F_{(2,13)} = 24.40763$, P < 0.0001. * P < 0.05. Data plotted as mean +/- SEM. **(D)** Representative FACS contour plots showing TMRM fluorescence intensity (measure of mitochondrial membrane potential) and GFP fluorescence intensity (mitochondrial abundance) of microglia from 2-3mo and 16-18mo *MG-MitoGFP* mice. **(E)** TMRM median fluorescence intensity (normalized to individual cell mitoGFP signal to account for mitochondrial abundance) of STR and MB microglia from 3mo (N = 6 STR, 6 MB) and 18mo (N = 5 STR, 6 MB) *MG-MitoGFP* mice. Two-way ANOVA with Bonferroni correction for post hoc comparisons: main effect of age, $F_{(1,19)} = 79.60044$, P < 0.0001; main effect of region, $F_{(1,19)} = 0.1661$, P = 0.68816. *** P < 0.001. Data was plotted as mean +/- SEM. **(F)** Cumulative probability distributions comparing TMRM fluorescence intensity across brain regions (STR *black*, MB *red*) in microglia from 2-3mo and 12-13mo C57Bl6 wildtype mice (*top panels*) and comparing TMRM fluorescence intensity across ages (2-3mo *black*, 12-13mo *red*, 16-18mo *blue*) in MB and STR microglia (*bottom panels*). * P < 0.05, Kolmogorov-Smirnov tests. Mice used for these experiments were not treated with 4 hydroxytamoxifen. Source data used to generate all graphs are provided as a Source Data file.

FIGURE 7: Loss of mitochondrial transcription factor A (TFAM) leads to altered morphology of both microglia and their mitochondria. (A) Schematic of transgenic crosses used to achieve microglial specific deletion of TFAM in microglia with or without simultaneous GFP labeling of microglial mitochondria. **(B)** qPCR-based analysis of TFAM expression (fold change relative to control, $2^{-\Delta\Delta CT}$) in FACS-isolated microglia from the midbrain (MB) and striatum (STR). Two-way ANOVA with Bonferroni correction for post hoc comparisons: main effect of genotype, $F_{(1,24)} = 115.410$, P < 0.0001, main effect of brain region $F_{(3,20)} = 1.654$, P = 0.213. N = 7 CTR mice (*filled circles*), N = 5 KO mice (*open circles*). **(C)** Representative high-magnification images of NAc microglia (IBA1) and mitochondria (GFP) from 5mo *MG-mitoGFP* (CTR) and *MG-mitoGFP-TFAMKO* (KO) mice. **(D)** Total mitochondrial volume within the field of view (FOV); Two-way ANOVA with Bonferroni correction for post hoc comparisons: main effect of genotype $F_{(3,14)} = 4.808$, P = 0.046, main effect of region $F_{(3,14)} = 4.716$, P = 0.046. **(E)** FOV mitochondrial number, Two-way ANOVA with Bonferroni correction for post hoc comparisons: main effect of genotype $F_{(3,14)} = 13.489$, P = 0.002, main effect of brain region $F_{(3,14)} = 15.864$, P = 0.0013. **(F)** Average FOV mitochondrial sphericity, Two-way ANOVA with Bonferroni correction for post hoc comparisons: main effect of genotype

$F_{(3,14)}$ = 5.313, P = 0.037, main effect of brain region $F_{(3,14)}$ = 1.636, P = 0.221. **(G)** Microglial density, Two-way ANOVA with Bonferroni correction for post hoc comparisons: main effect of genotype $F_{(3,14)}$ = 1.666, P = 0.218, main effect of brain region $F_{(3,14)}$ = 96.163, P < 0.0001. **(H)** Microglial tissue coverage (FOV volume), Two-way ANOVA with Bonferroni correction for post hoc comparisons: main effect of genotype $F_{(3,14)}$ = 9.665, P = 0.007, main effect of brain region $F_{(3,14)}$ = 43.274, P < 0.0001. **(I)** Branching complexity of individual microglia (total number of Sholl intersections), NAc N = 27 CTR and N = 35 KO cells; VTA N = 25 CTR N = 33 KO cells, Two-way ANOVA with Bonferroni correction for post hoc comparisons: main effect of genotype $F_{(3,116)}$ = 10.314, P = 0.002, main effect of brain region $F_{(3,116)}$ = 45.863, P < 0.0001. **(J)** FOV mitochondrial number normalized to FOV microglial volume, Two-way ANOVA with Bonferroni correction for post hoc comparisons: main effect of genotype $F_{(3,14)}$ = 0.366, P = 0.554, main effect of brain region $F_{(3,14)}$ = 2.295, P = 0.152. **(K)** FOV mitochondrial mass (FOV mitochondrial volume normalized to FOV microglial volume), Two-way ANOVA with Bonferroni correction for post hoc comparisons: main effect of genotype $F_{(3,14)}$ = 0.119, P = 0.734, main effect of brain region $F_{(3,14)}$ = 4.728, P = 0.047. Data was plotted as mean +/- SEM. For panels *D-H*, *J* and *K*, N = CTR 4 and 5 KO mice. For all data panels, CTR samples are represented by *filled circles* and KO samples are represented by *open circles*. Mice were treated with 4-hydroxytamoxifen and analyzed 2 months later as described in methods. * P < 0.05, ** P < 0.01,*** P < 0.001. Source data used to generate all graphs are provided as a Source Data file.

FIGURE 8: TFAM loss alters microglial size and baseline gene expression, but causes only subtle changes in microglial capacity to respond to acute inflammatory challenge. (A) Median Fluorescence Intensity for forward scatter (FSC, cell size), side scatter (SSC, internal cellular complexity), CD45, and CX3CR1 in STR and MB microglia from N = 7 CTR mice (*filled circles*) and N = 6 TFAM KO mice (*open circles*). See *Table S5* for F and P values from Two-way ANOVAs with Bonferroni correction for post hoc comparisons. **(B)** Heatmaps showing relative expression levels ($2^{-\Delta Ct}$) of key microglial function and mitochondrial function related genes in each group. Z-scores represent average gene expression across genotypes and brain regions. See *Table S5* for F and P values from Two-way ANOVA with Bonferroni correction for post hoc comparisons. * P < 0.05, ** P < 0.01, *** P < 0.001, significant effect of treatment, post hoc comparison with Bonferroni correction. $^{\$}$ P < 0.05, significant effect of brian region, post hoc comparison with Bonferroni correction. (N = 7 mice for CTR STR and CTR MB, N = 5 mice for TFAM KO STR and TFAM KO MB). **(C)** Principal Component Analysis of control (STR *filled gray circles*, MB *open gray circles*) and MG-TFAMKO (STR *filled black triangles*, MB *open black triangles*) samples based on microglial- and mitochondrial- function related genes. **(D)** Median Fluorescence Intensity of GFP, FSC, SSC, and CXC3CR1 signal in STR and MB microglia from N = 6 CTR mice (*filled circles*) and N = 4 TFAM KO mice (*open circles*) 12 hrs after LPS injection. Dotted line represents average signal of microglia from saline injected *MG-mitoGFP* mice (shown in *Fig 4F* and *Fig S4D*). See *Table S6* for F and P values from Two-way ANOVA with Bonferroni correction for post hoc comparisons. * P < 0.05, ** P < 0.01, *** P < 0.001, post hoc comparison with Bonferroni correction. **(E)** Fold change ($2^{-\Delta\Delta Ct}$) of key

microglial genes *Cd68*, *Itgam*, *Il1β*, and *Tgfβ1* in N = 5 LPS-treated CTR mice (*filled circles*) and N = 4 LPS-treated KO mice (*open circles*) relative to microglia from saline-treated mice. See *Table S7* for F and P values from Two-way ANOVA with Bonferroni correction for post hoc comparisons. * $P < 0.05$, ** $P < 0.01$, *** $P < 0.001$, post hoc comparison with Bonferroni correction. **(F)** Principal Component Analysis of microglia from saline- (*gray/black*) and LPS-treated (*pink/red*) CTR (*circles*) and TFAM KO (*triangles*) mice based on expression levels of microglial- and mitochondrial- function related genes. Fold-change analyses in *E* and PCA in *F* incorporate data from saline-treated *MG-mitoGFP* mice (*Fig. 4* and *Fig. S4*) as well as untreated *MG-TFAMKO* mice (*Fig. 8B*). Mice for these experiments were injected with 4-hydroxytamoxifen and analyzed 2 months later as described in methods. Data in *A*, *D*, and *E* was plotted as mean ± SEM. Source data for all graphs are provided as a Source Data file.

Figure 1

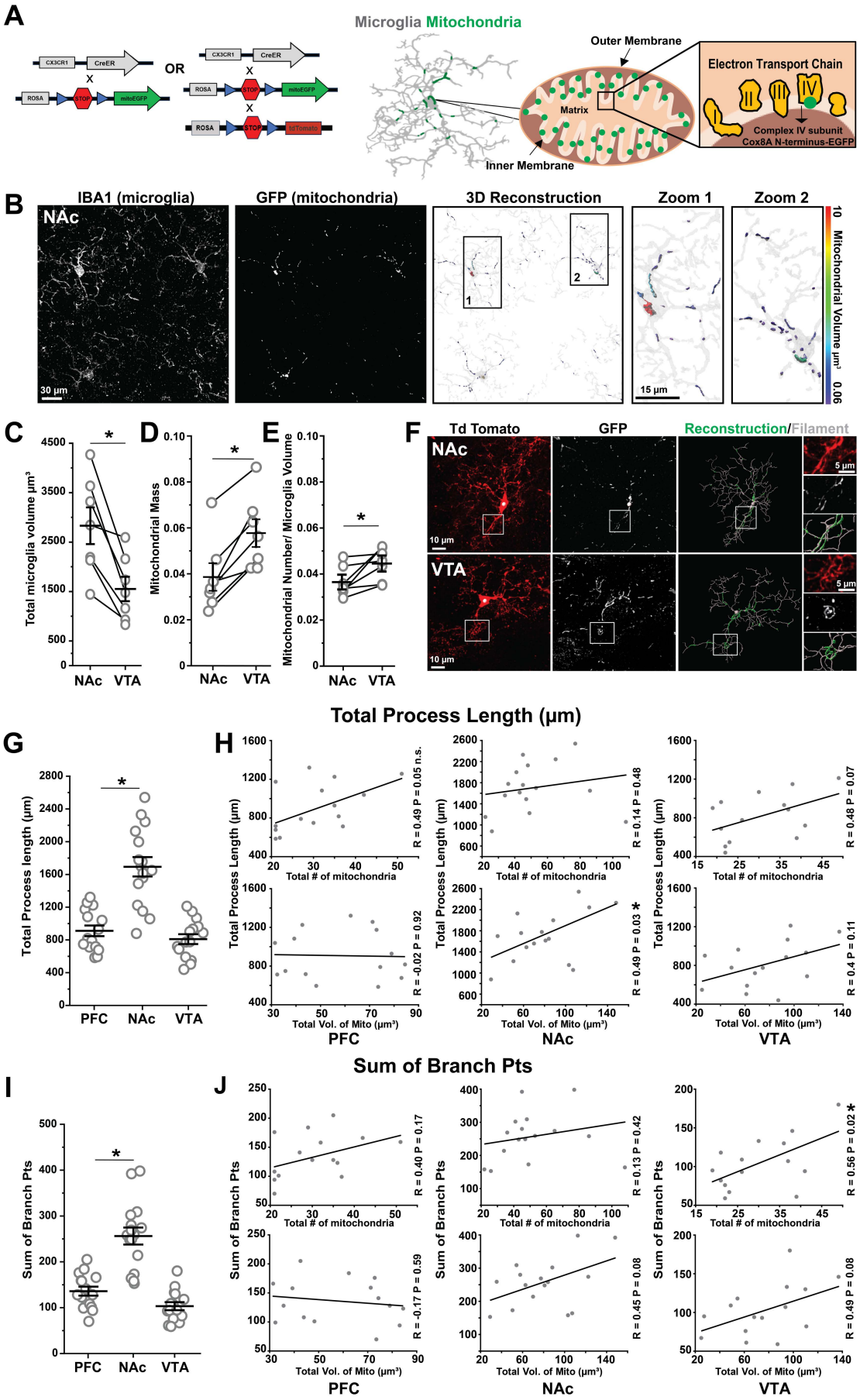
A
Microglia Mitochondria
CX3CR1
CreER
ROSA
STOP
mitoEGFP
OR
tdTomato
Outer Membrane
Matrix
Inner Membrane
Electron Transport Chain
Complex IV subunit
Cox8A N-terminus-EGFP
B
IBA1 (microglia)
GFP (mitochondria)
3D Reconstruction
Zoom 1
Zoom 2
NAc
30 µm
15 µm
Mitochondrial Volume µm³
C
Total microglia volume µm³
D
Mitochondrial Mass
E
Mitochondrial Number/ Microglia Volume
NAc
VTA
F
Td Tomato
GFP
Reconstruction/Filament
VTA
10 µm
5 µm
Total Process Length (µm)
G
Total Process length (µm)
PFC
H
Total # of mitochondria
Total Vol. of Mito (µm³)
R = 0.49 P = 0.05 n.s.
R = 0.14 P = 0.48
R = 0.48 P = 0.07
R = -0.02 P = 0.92
R = 0.49 P = 0.03
R = 0.4 P = 0.11
Sum of Branch Pts
I
J
R = 0.40 P = 0.17
R = 0.13 P = 0.42
R = 0.56 P = 0.02
R = -0.17 P = 0.59
R = 0.45 P = 0.08
R = 0.49 P = 0.08

Figure 2

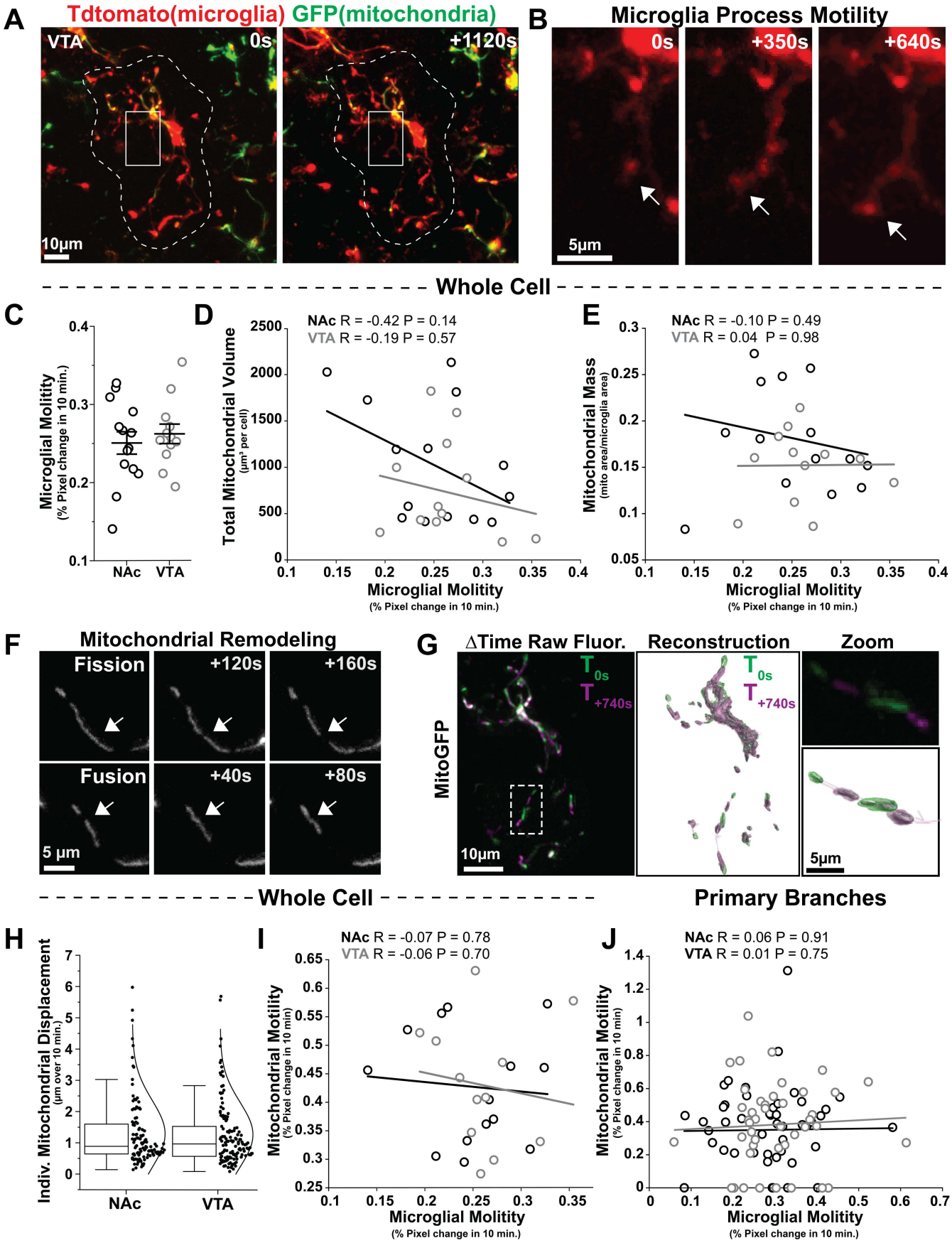
A
Tdtomato(microglia) GFP(mitochondria)
VTA
0s
+1120s
10µm
B
Microglia Process Motility
0s
+350s
+640s
5µm
Whole Cell
C
Microglial Molitity
(% Pixel change in 10 min.)
NAc
VTA
D
NAc R = -0.42 P = 0.14
VTA R = -0.19 P = 0.57
Total Mitochondrial Volume
(µm³ per cell)
Microglial Molitity
(% Pixel change in 10 min.)
E
NAc R = -0.10 P = 0.49
VTA R = 0.04 P = 0.98
Mitochondrial Mass
(mito area/microglia area)
Microglial Molitity
(% Pixel change in 10 min.)
F
Mitochondrial Remodeling
Fission
+120s
+160s
Fusion
+40s
+80s
5 µm
G
ΔTime Raw Fluor.
Reconstruction
Zoom
MitoGFP
T0s
T+740s
10µm
5µm
Whole Cell
Primary Branches
H
Indiv. Mitochondrial Displacement
(µm over 10 min.)
NAc
VTA
I
NAc R = -0.07 P = 0.78
VTA R = -0.06 P = 0.70
Mitochondrial Motility
(% Pixel change in 10 min)
Microglial Molitity
(% Pixel change in 10 min.)
J
NAc R = 0.06 P = 0.91
VTA R = 0.01 P = 0.75
Mitochondrial Motility
(% Pixel change in 10 min)
Microglial Molitity
(% Pixel change in 10 min.)

Figure 3

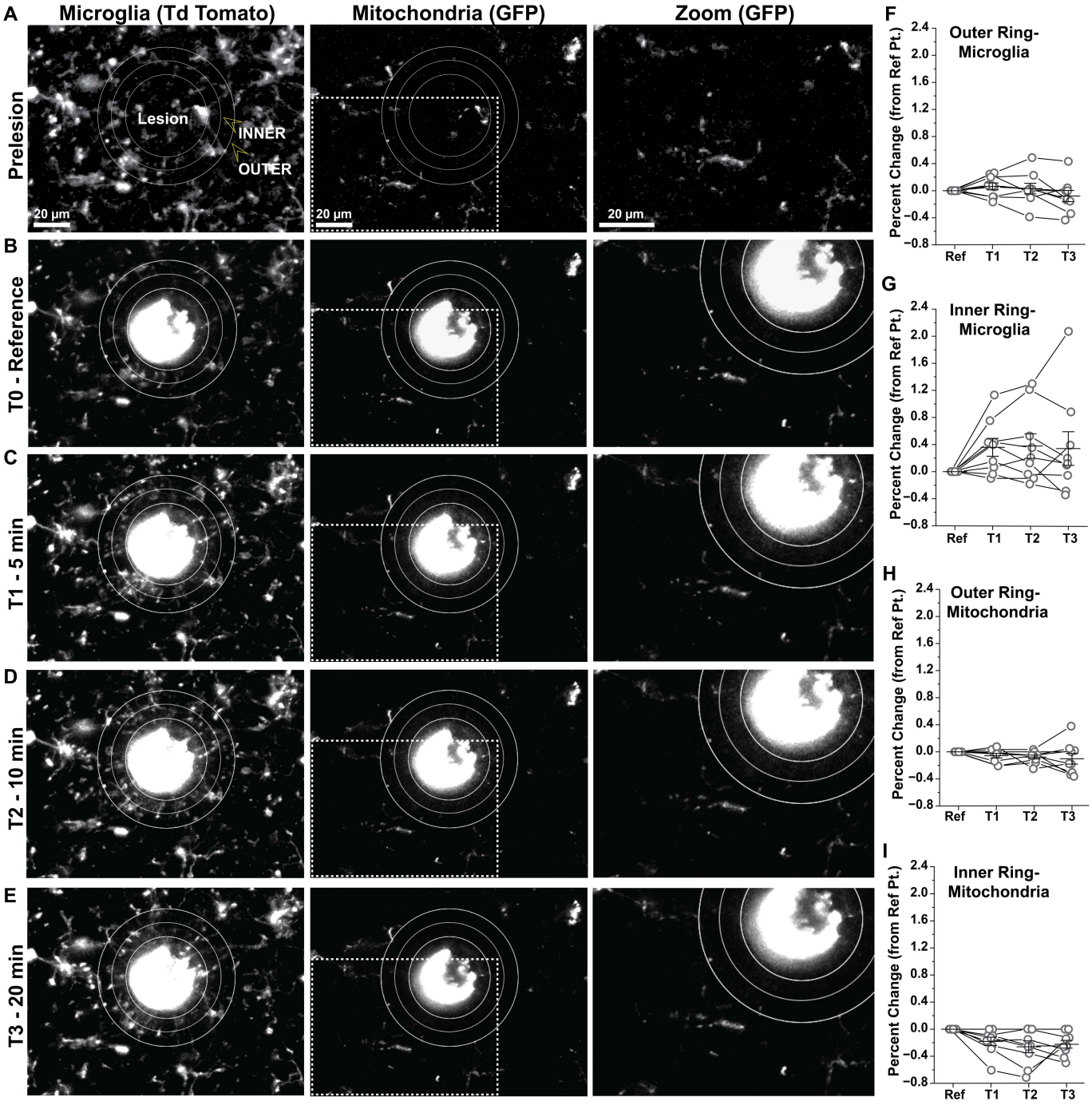
A
Microglia (Td Tomato)
Mitochondria (GFP)
Zoom (GFP)
Prelesion
Lesion
INNER
OUTER
20 µm
20 µm
20 µm
B
T0 - Reference
C
T1 - 5 min
D
T2 - 10 min
E
T3 - 20 min
F
Outer Ring-Microglia
G
Inner Ring-Microglia
H
Outer Ring-Mitochondria
I
Inner Ring-Mitochondria
Percent Change (from Ref Pt.)
2.4
2.0
1.6
1.2
0.8
0.4
0.0
−0.4
−0.8
Ref
T1
T2
T3

Figure 4

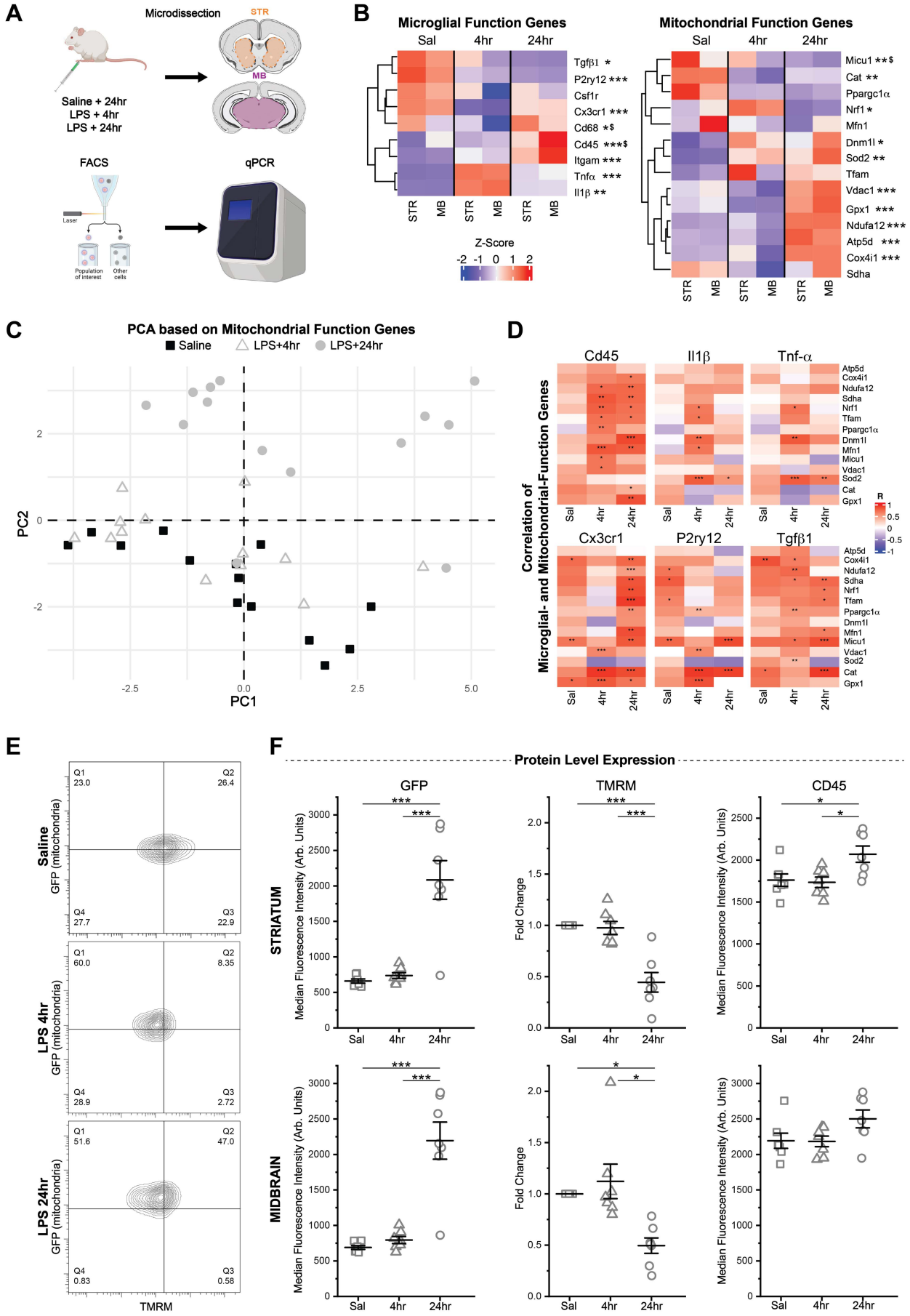
A
Microdissection
STR
MB
Saline + 24hr
LPS + 4hr
LPS + 24hr
FACS
qPCR
Laser
Population of interest
Other cells
B
Microglial Function Genes
Sal
4hr
24hr
Tgfβ1 *
P2ry12 ***
Csf1r
Cx3cr1 ***
Cd68 *$
Cd45 ***$
Itgam ***
Tnfα ***
Il1β **
STR
MB
Z-Score
-2 -1 0 1 2
Mitochondrial Function Genes
Micu1 **$
Cat **
Ppargc1α
Nrf1 *
Mfn1
Dnm1l *
Sod2 **
Tfam
Vdac1 ***
Gpx1 ***
Ndufa12 ***
Atp5d ***
Cox4i1 ***
Sdha
C
PCA based on Mitochondrial Function Genes
Saline
LPS+4hr
LPS+24hr
PC2
PC1
-2.5
0.0
2.5
5.0
D
Cd45
Il1β
Tnf-α
Cx3cr1
P2ry12
Tgfβ1
Correlation of Microglial- and Mitochondrial-Function Genes
Atp5d
Cox4i1
Ndufa12
Sdha
Nrf1
Tfam
Ppargc1α
Dnm1l
Mfn1
Micu1
Vdac1
Sod2
Cat
Gpx1
Sal
4hr
24hr
R
1
0.5
0
-0.5
-1
E
Saline
LPS 4hr
LPS 24hr
GFP (mitochondria)
TMRM
Q1 23.0
Q2 26.4
Q4 27.7
Q3 22.9
Q1 60.0
Q2 8.35
Q4 28.9
Q3 2.72
Q1 51.6
Q2 47.0
Q4 0.83
Q3 0.58
F
Protein Level Expression
GFP
TMRM
CD45
STRIATUM
MIDBRAIN
Median Fluorescence Intensity (Arb. Units)
Fold Change
Sal
4hr
24hr

Figure 5

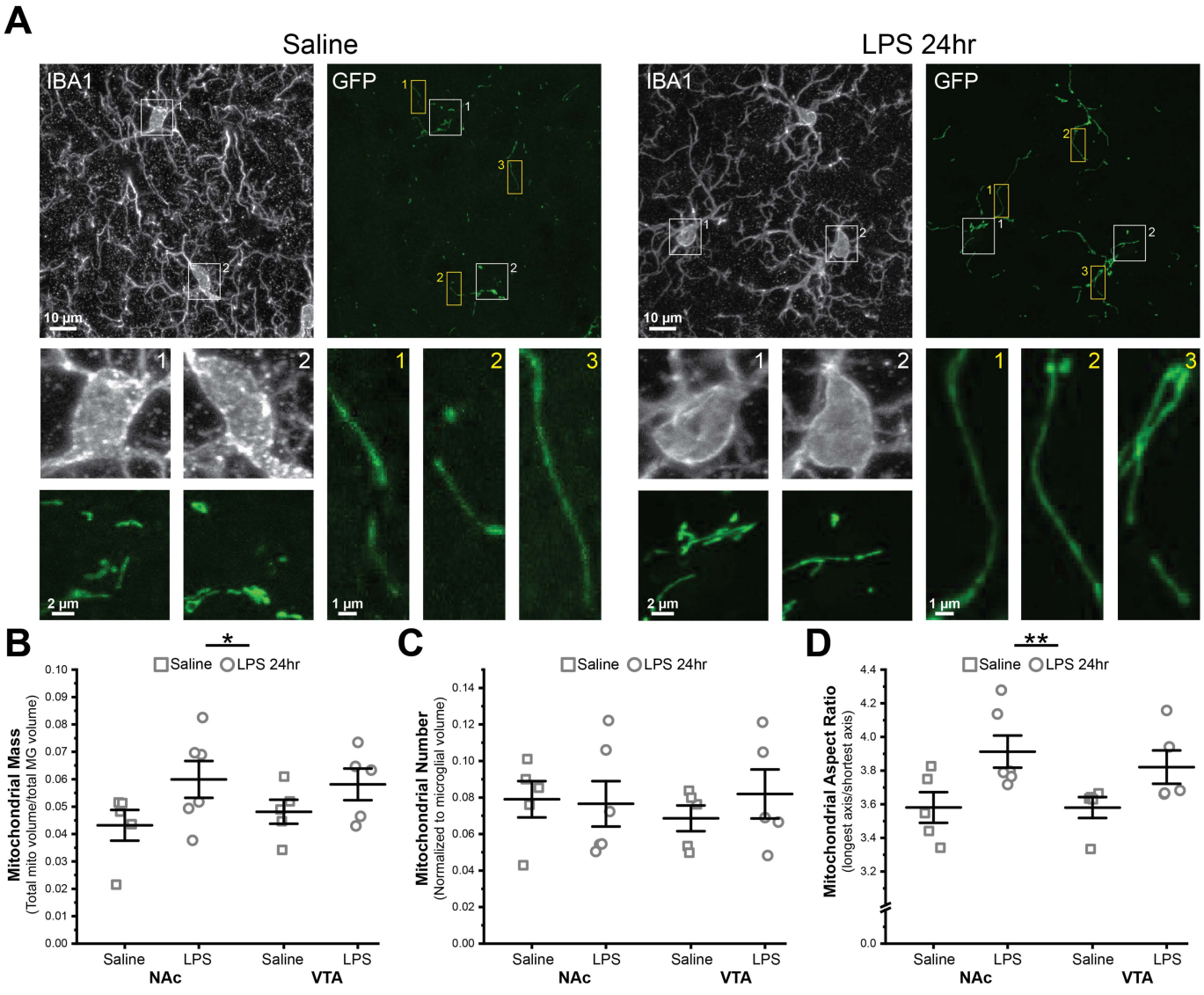
A
Saline
LPS 24hr
IBA1
GFP
10 µm
2 µm
1 µm
B
C
D
Saline
LPS 24hr
Mitochondrial Mass
(Total mito volume/total MG volume)
Mitochondrial Number
(Normalized to microglial volume)
Mitochondrial Aspect Ratio
(longest axis/shortest axis)
Saline
LPS
NAc
VTA

Figure 6

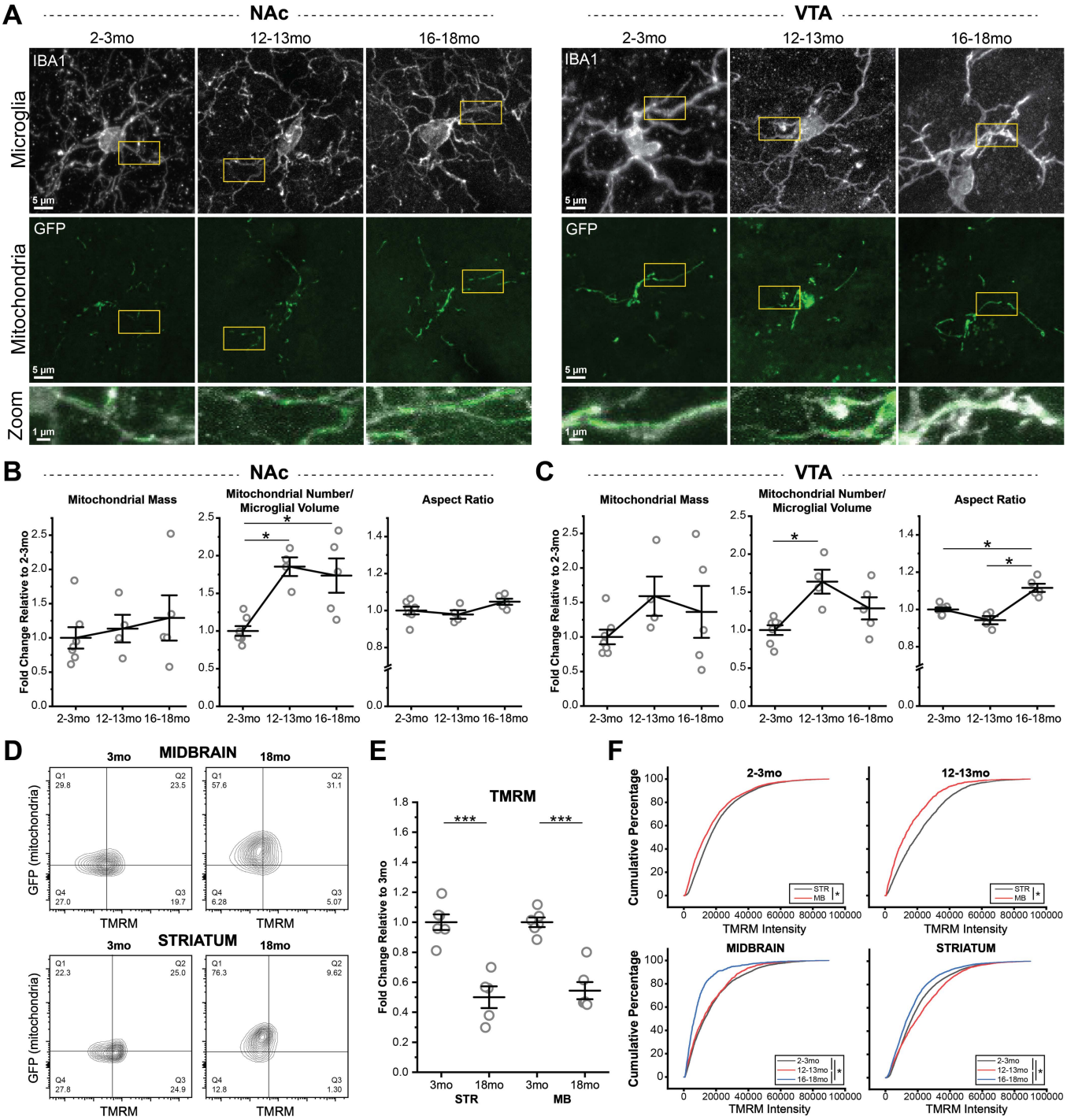
A
NAc
VTA
2-3mo
12-13mo
16-18mo
IBA1
GFP
Microglia
Mitochondria
Zoom
5 µm
1 µm
B
C
Mitochondrial Mass
Mitochondrial Number/ Microglial Volume
Aspect Ratio
Fold Change Relative to 2-3mo
D
MIDBRAIN
STRIATUM
3mo
18mo
GFP (mitochondria)
TMRM
E
TMRM
Fold Change Relative to 3mo
STR
MB
F
Cumulative Percentage
TMRM Intensity
STR
MB
2-3mo
12-13mo
16-18mo

Figure 7

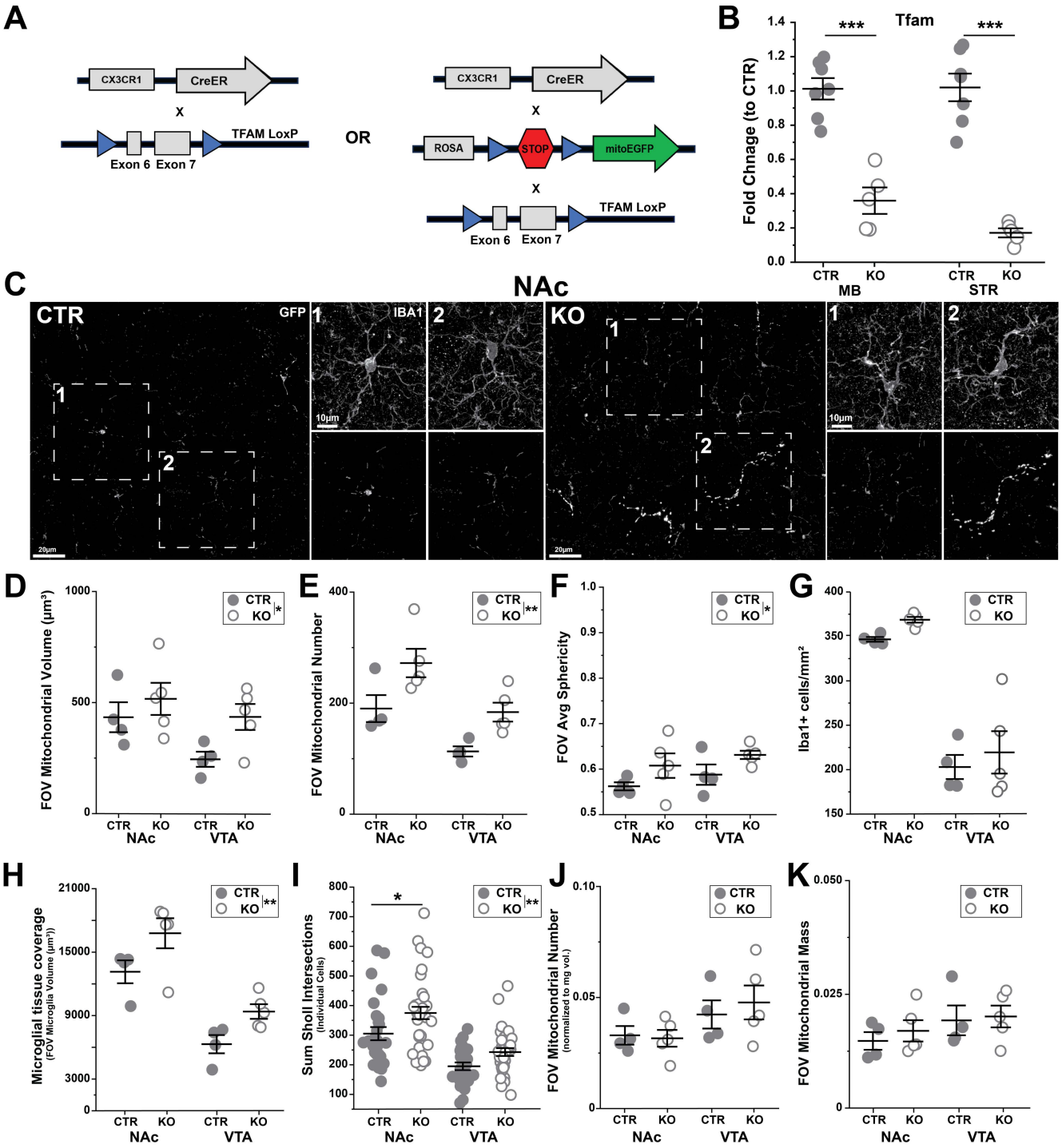
A
CX3CR1
CreER
x
TFAM LoxP
Exon 6 Exon 7
OR
CX3CR1
CreER
x
ROSA
STOP
mitoEGFP
x
TFAM LoxP
Exon 6 Exon 7
B
Tfam
***
***
Fold Chnage (to CTR)
CTR KO CTR KO
MB STR
C
NAc
CTR
GFP
IBA1
KO
10µm
20µm
D
FOV Mitochondrial Volume (µm³)
E
FOV Mitochondrial Number
F
FOV Avg Sphericity
G
Iba1+ cells/mm²
H
Microglial tissue coverage
(FOV Microglia Volume (µm³))
I
Sum Sholl Intersections
(Individual Cells)
J
FOV Mitochondrial Number
(normalized to mg vol.)
K
FOV Mitochondrial Mass
CTR
KO
CTR KO CTR KO
NAc VTA

Figure 8

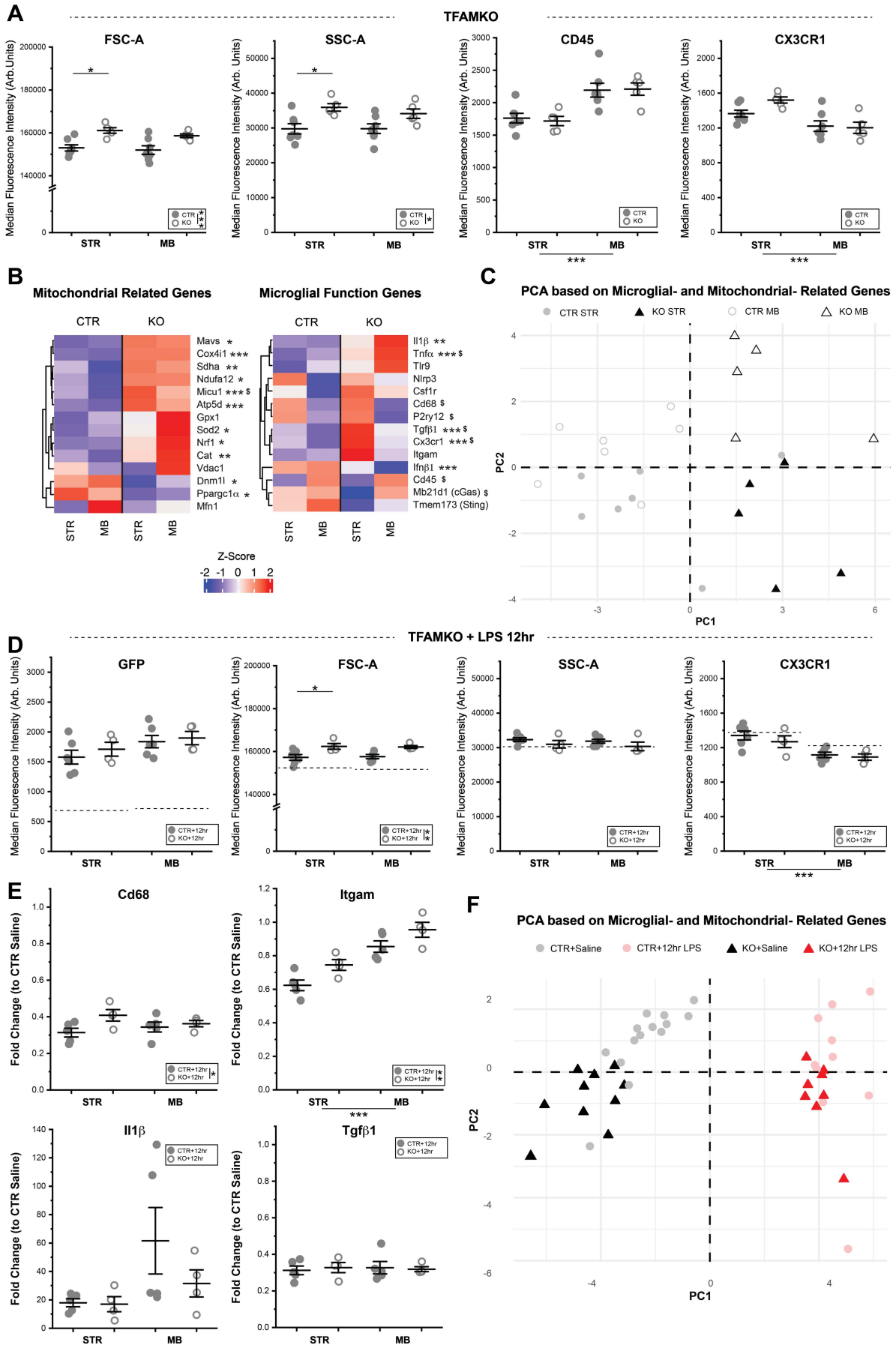
A
TFAMKO
FSC-A
SSC-A
CD45
CX3CR1
Median Fluorescence Intensity (Arb. Units)
CTR
KO
STR
MB
B
Mitochondrial Related Genes
Microglial Function Genes
Mavs *
Cox4i1 ***
Sdha **
Ndufa12 *
Micu1 *** $
Atp5d ***
Gpx1
Sod2 *
Nrf1 *
Cat **
Vdac1
Dnm1l *
Ppargc1α *
Mfn1
Il1β **
Tnfα *** $
Tlr9
Nlrp3
Csf1r
Cd68 $
P2ry12 $
Tgfβ1 *** $
Cx3cr1 *** $
Itgam
Ifnβ1 ***
Cd45 $
Mb21d1 (cGas) $
Tmem173 (Sting)
Z-Score
C
PCA based on Microglial- and Mitochondrial- Related Genes
CTR STR
KO STR
CTR MB
KO MB
PC1
PC2
D
TFAMKO + LPS 12hr
GFP
CTR+12hr
KO+12hr
E
Cd68
Itgam
Il1β
Tgfβ1
Fold Change (to CTR Saline)
F
PCA based on Microglial- and Mitochondrial- Related Genes
CTR+Saline
CTR+12hr LPS
KO+Saline
KO+12hr LPS

Supplementary Figure 1 - Related to Figure 1

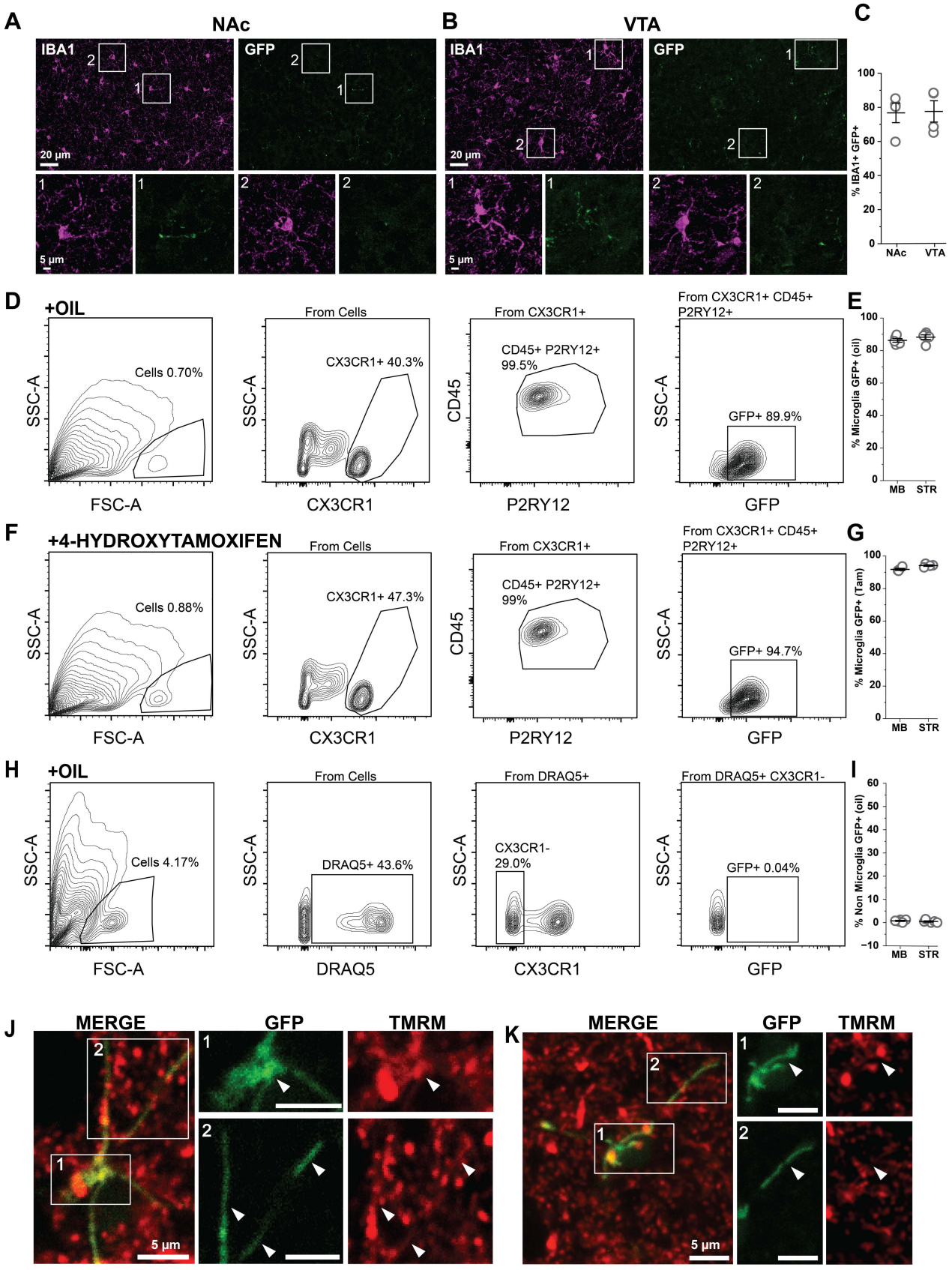

FIGURE S1: *MG-MitoGFP* mice accurately label microglial mitochondria (*related to Figure 1*). (A,B) 20x confocal images of native GFP signal and Iba1 (*magenta*) staining in *CX3CR1-CreER; flox-stop mitoGFP* (*MG-MitoGFP*) mice. *Boxes* highlight examples of IBA1+ GFP+ positive cells as well as IBA1+GFP- cells from both the NAc and VTA. **(C)** Percentage of Iba1+ NAc and VTA microglia exhibiting GFP expression. N = 4 mice for NAc and VTA, 2-3mo of age. Data was plotted as mean +/- SEM. **(D)** Sequential gating strategy for FACS-based analysis of microglia from oil-injected *MG-MitoGFP* mice. **(E)** Percentage of midbrain (MB) and striatum (STR) microglia (CX3CR1+P2RY12+CD45+) that are also GFP+. N = 5 mice for MB and STR, 3-4mo of age. Data was plotted as mean +/- SEM. **(F)** Sequential gating strategy for FACS-based analysis of microglia from 4-hydroxytamoxifen-injected *MG-MitoGFP* mice. **(G)** Percentage of MB and STR microglia (CX3CR1+P2RY12+CD45+) that are also GFP+ in 4-hydroxytamoxifen treated mice. N = 4 mice for MB and STR, 3-4mo of age. Data was plotted as mean +/- SEM. **(H)** Sequential FACS gating strategy used to identify non-microglial cells (DRAQ5+, CX3CR1-) and examine GFP expression. **(I)** Percentage of non-microglial cells (CX3CR1- Draq5+) exhibiting GFP expression in MB and STR. N = 4 mice for MB and STR, 3-4mo of age. Data was plotted as mean +/- SEM. **(J-K)** Live imaging of acute brain sections from *MG-MitoGFP* mice incubated with mitochondrial membrane potential indicator dye TMRM. Source data for all graphs are provided as a Source Data file.

Supplementary Figure 2 - Related to Figure 1

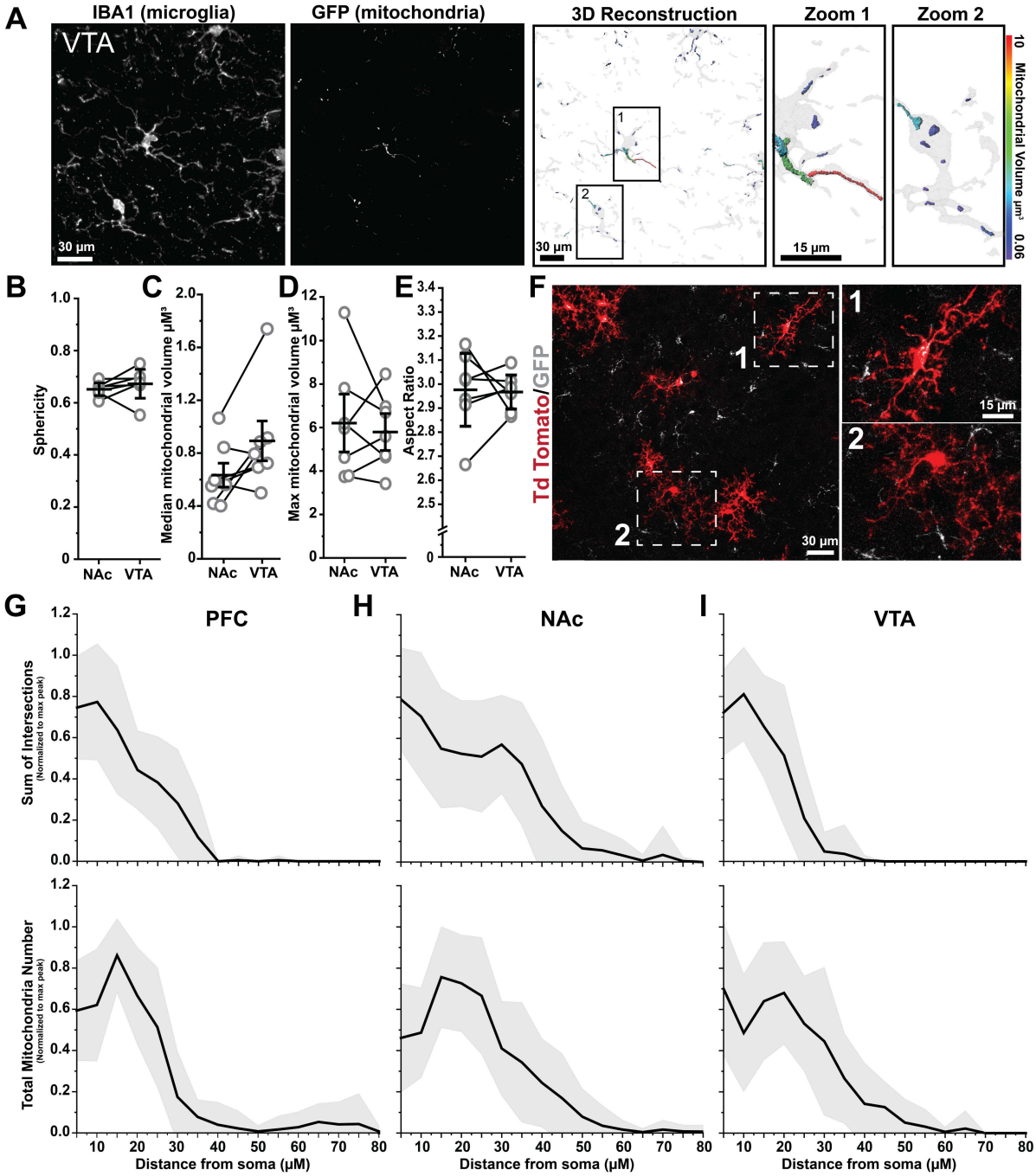

J

Morphological Parameters	Region	Total # of Mitochondria	Total Volume of Mitochondria
Total Process Length	PFC	R=0.49 P=0.05 n.s.	R=-0.02 P=0.92
	Nac	R=0.14 P=0.48	R=0.49 P=0.03 *
	VTA	R=0.48 P=0.07	R=0.40 P=0.11
Sum of branch pts.	PFC	R=0.40 P=0.17	R=-0.17 P=0.59
	Nac	R=0.13 P=0.42	R=0.45 P=0.08
	VTA	R=0.56 P=0.02*	R=0.49 P=0.08
Max # of intersections	PFC	R=0.54 P=0.02*	R=-0.16 P=0.99
	Nac	R=0.45 P=0.08	R=-0.34 P=0.13
	VTA	R=0.53 P=0.05 n.s.	R=0.48 P=0.10

FIGURE S2: Mitochondrial abundance and distribution align with morphological features of microglia (*related to Figure 1*). (A) Representative high-magnification images of VTA microglia (*Iba1*) and mitochondria (*native GFP*); 3D volumetric reconstructions of microglia (*gray*) and mitochondria (*colored according to volume*) from *MG-MitoGFP* mice. **(B-E)** Quantification of field of view (FOV) mitochondrial morphological parameters across brain regions. Data points from the same mouse are identified by connecting lines (N = 7 mice, 2mo of age). Sphericity: P = 0.346, Two-tailed paired t-test. Median mitochondria volume: P = 0.056, Two-tailed paired t-test. Max mitochondria volume: P = 0.640, Two-tailed paired t-test. Aspect ratio (longest axis divided by shortest axis): P = 0.894, Two-tailed paired t-test. *P<0.05 Data was plotted as mean +/- SEM. **(F)** Representative 20x image of the sparse recombination observed in *MG-MitoGFP;Ai14* triple transgenic mice that have not been treated with 4-hydroxytamoxifen. **(G-I)** Sholl analysis of 3D-reconstructed microglia and distribution of their mitochondria relative to cell somas (PFC N = 16, NAc N = 16 and VTA N = 15 cells). Data was plotted as mean (black line) +/- SEM (gray shading). **(J)** Table of robust regression analyses relating cell morphological features of individual microglia to number and volume of their mitochondria. Mice used for these experiments were not treated with 4-hydroxytamoxifen. Source data used to prepare all graphs are provided as a Source Data file.

Supplementary Figure 3 - Related to Figure 2

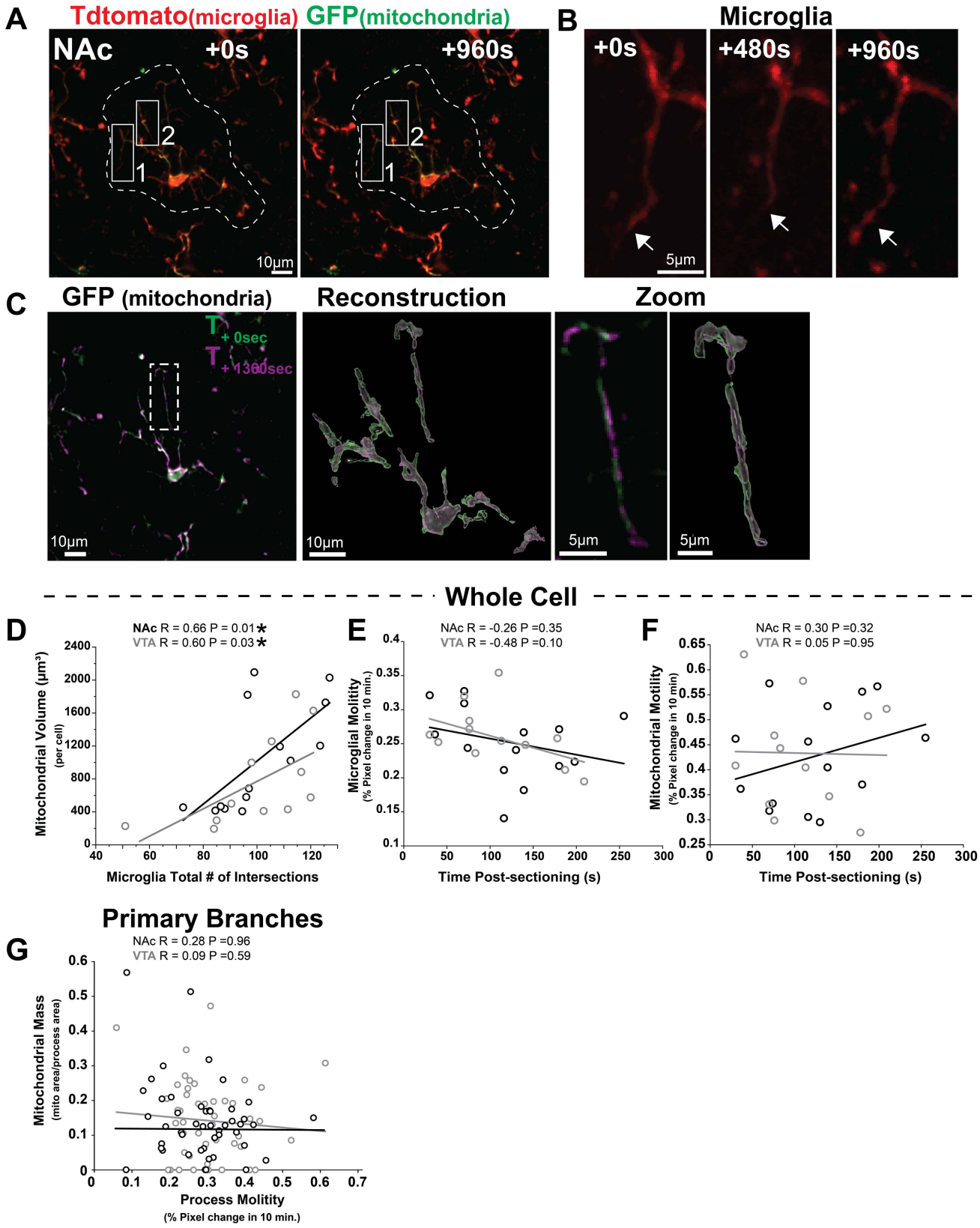

FIGURE S3: Microglial motility is not correlated with tissue sectioning or mitochondrial motility (*related to Figure 2*). **(A)** Representative images taken during multiphoton live imaging of NAc microglia (*TdTomato*) in acute brain sections from 1.5 -2mo old *MG-mitoGFP;Ai14* mice. **(B)** Example of microglial cell process retraction and re-extension highlighted by *white arrows*. **(C)** Raw fluorescence from multiphoton imaging and corresponding 3D reconstruction of microglial mitochondria, colored by time. *Dashed white box* shown at higher magnification *at right*. **(D)** Robust regression with false discovery rate correction analysis relating total mitochondrial volume per cell and microglial morphological complexity (total Sholl intersections across all radii). N = 14 NAc cells, R = 0.66 P = 0.01 and N = 12 VTA cells, R = 0.60 P = 0.03. **(E)** Robust regression with false discovery rate correction analysis relating microglial motility (% pixel change over 10min) to time elapsed since preparation of acute brain sections. N = 14 NAc cells, R = -0.26 P = 0.35 and N = 12 VTA cells, R = -0.48 P = 0.10. **(F)** Robust regression with false discovery rate correction analysis relating mitochondrial motility (% pixel change over 10min) to time elapsed since preparation of acute brain sections. N = 14 NAc cells, R = 0.30 P = 0.32 and N = 12 VTA cells, R = 0.05 P = 0.95. **(G)** Robust regression with false discovery rate correction analysis relating mitochondrial mass within one primary microglial branch to motility of that primary branch for NAc and VTA microglia. N = 55 NAc microglia primary processes, R = 0.28 P = 0.96 and N=46 VTA microglia primary processes, R = 0.09 P = 0.59. Mice used for these experiments were not treated with 4-hydroxytamoxifen. *P<0.05. Source data used to prepare all graphs are provided as a Source Data file.

Supplementary Figure 4 - Related to Figure 4

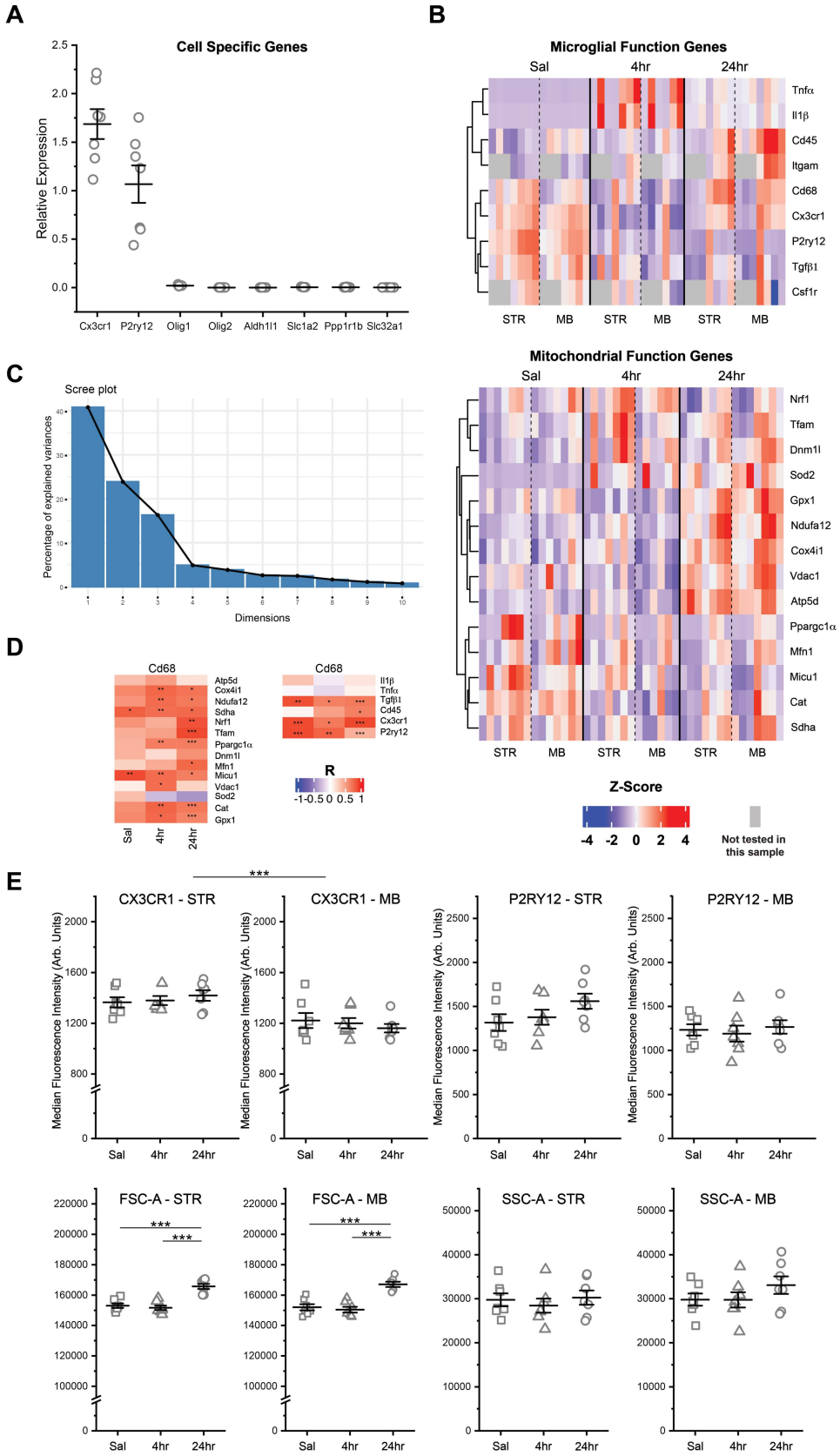

FIGURE S4: Microglial and mitochondrial responses to inflammatory challenge (LPS, *related to Figure 4*). (A) Relative expression levels ($2^{-\Delta Ct}$) of cell specific genes for microglia (*Cx3cr1* and *P2ry12*), oligodendrocyte lineage cells (*Olig1*, *Olig2*), astrocytes (*Aldh1l1*, and *Slc1a2*) and neurons (*Ppp1r1b* and *Slc32a1*) from a subset of saline and LPS treated samples (N = 7 mice), confirming purity of collected microglia. Data was plotted as mean +/- SEM. **(B)** Heatmaps showing relative expression levels ($2^{-\Delta Ct}$) of key microglial function and mitochondrial function genes for individual samples (Saline STR N = 7 mice, Saline MB N = 7 mice, LPS 4hr STR N = 7 mice, LPS 4hr MB N = 6 mice, LPS 24hr STR N = 7 mice, LPS 24hr MB N = 7 mice); *corresponding heat map with group averages shown in Fig. 4B*. **(C)** Scree plot demonstrating the percentage of dataset variance explained by each principal component identified via Principal Component Analysis of all samples. PCA (shown in *Fig. 4C*) was carried out using expression values from mitochondrial function genes only. **(D)** Heat maps depicting the degree of correlation between *Cd68* expression and expression levels of microglial and mitochondrial function genes as determined by robust regression analysis with false discovery rate correction. See *Table S4* for R^2- and P-values. * $P < 0.05$, ** $P < 0.01$, *** $P < 0.001$. **(E)** Median Fluorescence Intensity of CX3CR1, P2RY12, FSC-A, SSC-A signals in STR and MB microglia from Saline (N = 7, *squares*), LPS 4hr (N = 7, *triangles*), and LPS 24hr (N = 7, *circles*) mice. Two-way ANOVA with Bonferroni correction for post hoc comparisons: CX3CR1, main effect of treatment, $F_{(2,36)} = 0.00442$, $P = 0.99559$, main effect of region, $F_{(1,36)} = 30.80804$, $P < 0.0001$; P2RY12, main effect of treatment, $F_{(2,36)} = 1.71502$, $P = 0.19514$, main effect of region $F_{(1,36)} = 7.52567$, $P = 0.00942$; FSC-A, main effect of treatment, $F_{(2,36)} = 49.45017$, $P < 0.0001$, main effect of region, $F_{(1,36)} = 0.03974$, $P = 0.84311$; SSC-A, main effect of treatment, $F_{(2,36)} = 1.32646$, $P = 0.27808$, main effect of region, $F_{(1,36)} = 1.07222$, $P = 0.30735$. *** $P < 0.001$. Data was plotted as mean +/- SEM. Mice used for these experiments were not treated with 4-hydroxytamoxifen. Source data used to generate all graphs are provided as a Source Data file.

Supplementary Figure 5 - Related to Figure 5

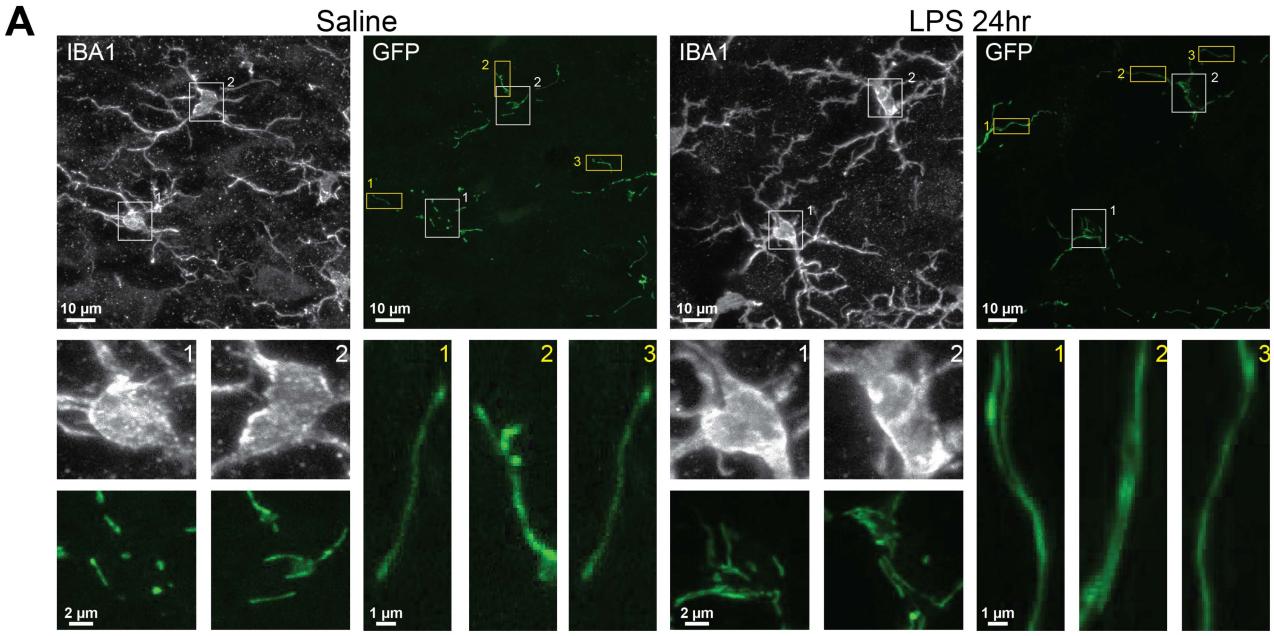

FIGURE S5: VTA microglial mitochondrial response to inflammatory challenge (LPS, *related to Figure 5*). **(A)** Representative images of VTA microglia (IBA1) and microglial mitochondria (GFP) from 3-4mo *MG-MitoGFP* mice injected with saline (*left*) or LPS 24hr (*right*) prior to euthanasia. *White* and *yellow boxes* highlight examples of somatic mitochondria and cell process mitochondria shown at higher magnification *below*. Mice used for these experiments were not treated with 4-hydroxytamoxifen.

Supplementary Figure 6 - Related to Figure 6

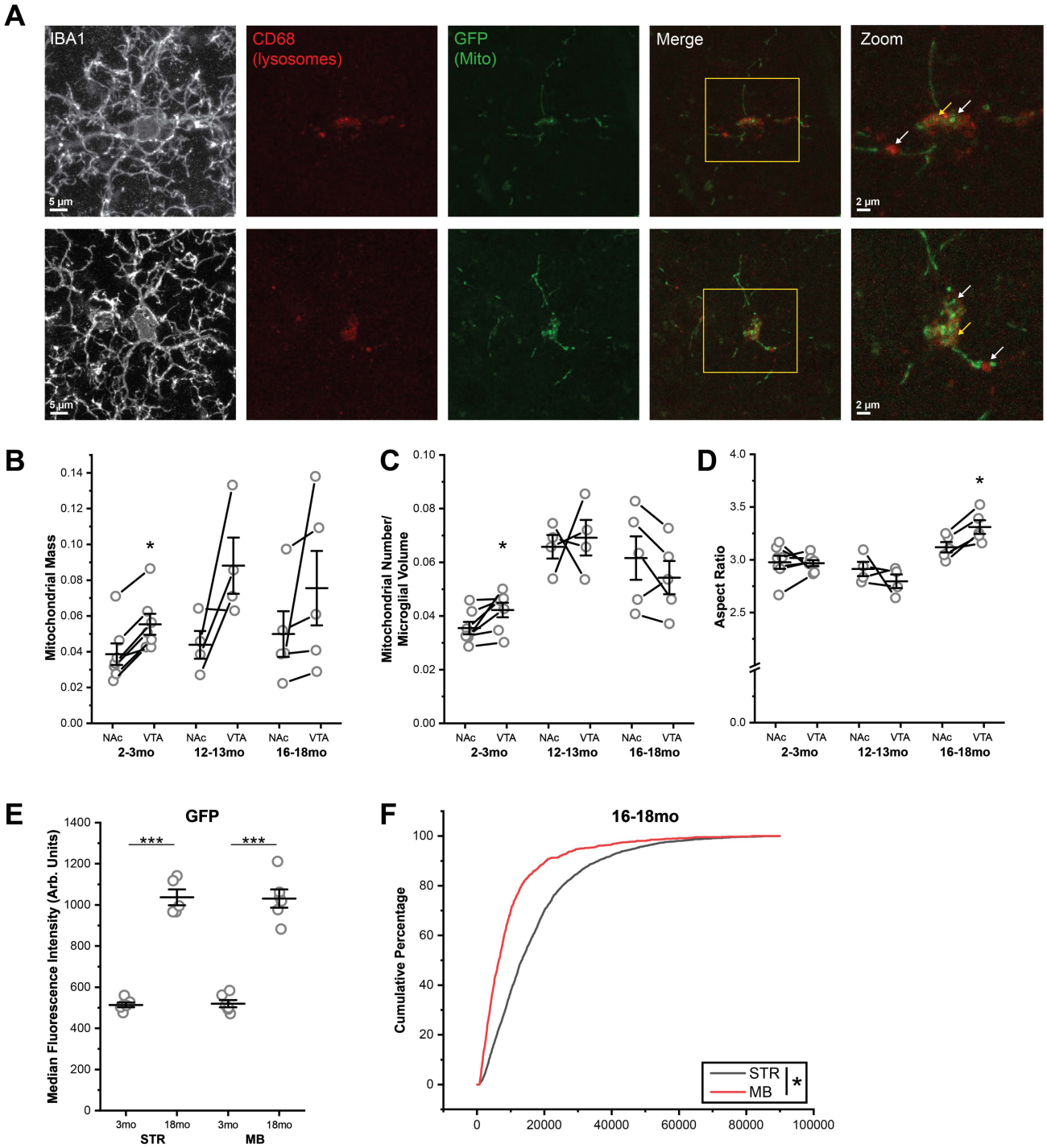

FIGURE S6: Microglial mitochondria undergo remodeling in middle- and late middle aged mice (*related to Figure 6*). (A) Representative confocal images of microglia (IBA1) from 18mo *MG-MitoGFP* mice revealing dim remnants of somatic autofluorescent material following tissue treatment with Trueblack (Biotium). Co-staining with CD68 confirms that brighter mitoGFP signals (*white arrows*) are not colocalized with bright CD68 puncta (*white arrowheads*) and that dimmer somatic GFP autofluorescence that colocalizes with CD68 (*yellow arrows*) is easily distinguished from brighter mitoGFP signals. **(B-D)** Comparison of FOV microglial mitochondrial mass (2-3mo P = 0.001, 12-13mo P = 0.092, 16-18mo P = 0.235, two tailed paired t-test), mitochondrial number (2-3mo P = 0.026, 12-13mo P = 0.778, 16-18mo P = 0.167, two tailed paired t-test), and mitochondrial aspect ratio (2-3mo P = 0.885, 12-13mo P = 0.392, 16-18mo P = 0.009, two tailed paired t-test) across the NAc and VTA of individual 2-3mo (N = 7 mice), 12-13mo (N = 4 mice), and 16-18mo (N = 5 mice) *MG-MitoGFP* mice. * P< 0.05. Data was plotted as mean +/- SEM. **(E)** GFP median fluorescence intensity of STR and MB microglia from 3mo (N = 6 STR, 6 MB) and 18mo (N = 5 STR, 6 MB) *MG-MitoGFP* mice. Two-way ANOVA with Bonferroni correction for post hoc comparisons: main effect of age, $F_{(1,19)} = 287.28$, $P < 0.0001$; main effect of region, $F_{(1,19)} = 0.0003$, $P = 0.9953$. *** P < 0.001. Data was plotted as mean +/- SEM **(F)** Cumulative probability distributions comparing microglial TMRM intensity of microglia across brain regions (STR *black*, MB *red*) in 16-18mo C57Bl6 wildtype mice. * P < 0.05, Kolmogorov-Smirnov tests. Mice used for these experiments were not treated with 4 hydroxytamoxifen. Source data are provided as a Source Data file.

Supplementary Figure 7 - Related to Figure 7

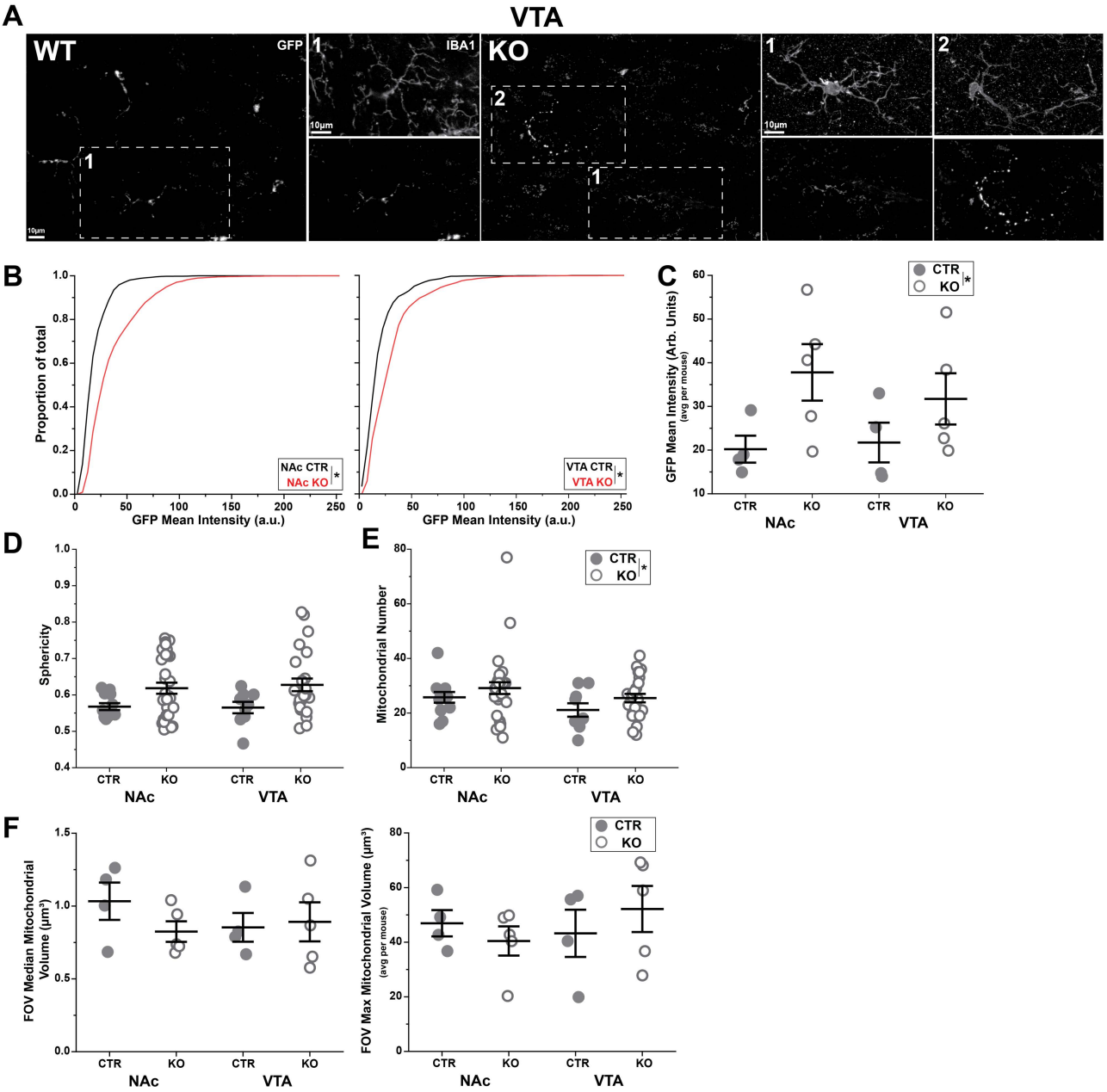

FIGURE S7: Microglial mitochondria display increased GFP intensity in *MG-mitoGFP-TFAMKO* mice (*related to figure 7*). (A) Representative confocal images of microglia (IBA1) and mitochondria (GFP) in the VTA of *MG-mitoGFP* (CTR) and *MG-mitoGFP-TFAMKO* (KO) mice. **(B)** Cumulative distribution of GFP intensity of individual mitochondria across genotypes (CTR = *black*, KO = *red*) in the VTA and NAc. Distribution curves for each animal within a group were averaged to generate the displayed, group average, cumulative distributions. *P < 0.05, Kolmogorov-Smirnov test. **(C)** Mean mitoGFP intensity for all mitochondria analyzed for each mouse. CTR (*filled circles*) = 4 mice and KO (*open circles*) = 5 mice. Two-way ANOVA with Bonferroni correction for post hoc comparisons: main effect of genotype, $F_{(3,14)} = 6.264$, P = 0.025, main effect of brain region, $F_{(3,14)} = 0.171$, P = 0.685. Data was plotted as mean +/- SEM. **(D)** Average sphericity of mitochondria within individual NAc and VTA microglial cells. Two-way ANOVA with Bonferroni correction for post hoc comparisons: main effect of genotype $F_{(3,73)} = 8.119$, P = 0.005, main effect of brain region, $F_{(3,73)} = 0.028$, P = 0.867. Data was plotted as mean +/- SEM. **(E)** Total number of mitochondria within individual NAc and VTA microglial cells. Two-way ANOVA with Bonferroni correction for post hoc comparisons: main effect of genotype $F_{(3,73)} = 2.452$, P = 0.121, main effect of brain region, $F_{(3,73)} = 2.805$, P = 0.098. Data was plotted as mean +/- SEM. **(F)** Median volume and maximum volume of mitochondria within FOV across CTR (*filled circles*) and KO (*open circles*) mice. Two-way ANOVA with Bonferroni correction for post hoc comparisons: medium volume main effect of genotype $F_{(3,14)} = 0.584$, P = 0.457 and maximum volume main effect of genotype $F_{(3,73)} = 0.254$, P = 0.621. Data was plotted as mean +/- SEM. Mice were treated with 4-hydroxytamoxifen and analyzed 2 months later as described in methods. Source data used to generate all graphs are provided as a Source Data file.

Supplementary Figure 8 - Related to Figure 8

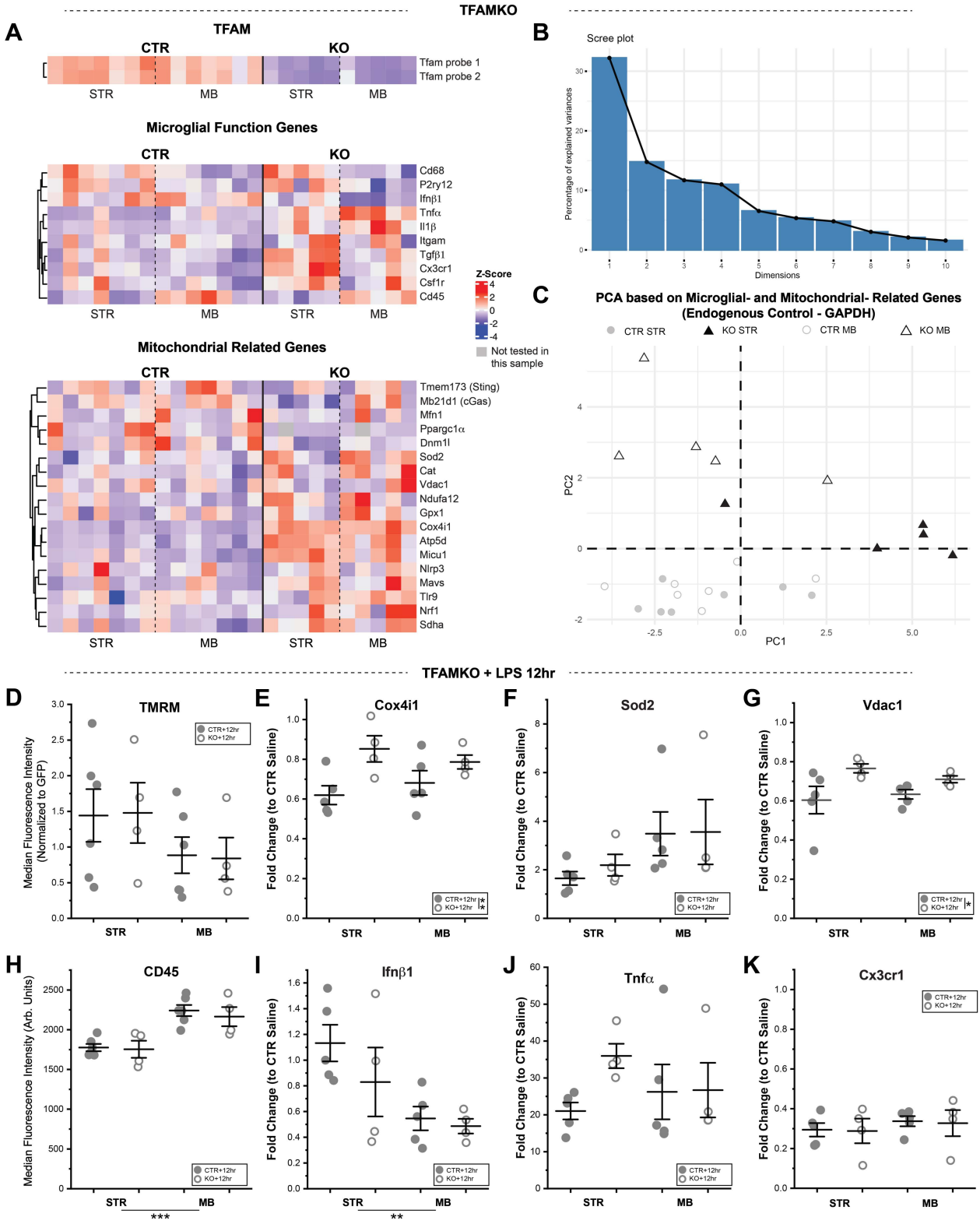

FIGURE S8: TFAM loss alters microglial size and baseline gene expression, but causes only subtle changes in microglial capacity to respond to acute inflammatory challenge (*related to Figure 8*). (A) Heatmaps showing relative expression levels ($2^{-\Delta Ct}$) of *Tfam*, key microglial function genes, and mitochondrial function genes for individual samples (STR and MB from N = 7 CTR mice, STR and MB from N = 5 TFAM KO mice) . **(B)** Scree plot demonstrating the percentage of dataset variance explained by each principal component identified via Principal Component PCA of all samples shown in *Fig. 8C*. **(C)** Principal Component Analysis of microglia from control (STR *filled gray circles,* MB *open gray circles*) and *MG-TFAMKO* (STR *filled black triangles,* MB *open black triangles*) mice based on expression of microglial- and mitochondrial- function genes calculated relative to a second endogenous control gene, *Gapdh*. **(D)** TMRM median fluorescence intensity (normalized to individual cell mitoGFP signal to account for mitochondrial abundance) of microglia from LPS treated CTR (N = 6, *filled circles*) and *MG-TFAMKO* (N = 4, *open circles*) mice. **(E-G)** Fold change ($2^{-\Delta\Delta Ct}$) of expression of mitochondrial genes *Cox4i1*, *Sod2*, and *Vdac1* in LPS treated MG-TFAMKO (N = 4, *open circles*) and LPS treated CTR (N = 5, *filled circles*) mice relative to microglia from saline treated *MG-mitoGFP* mice (*Fig. 4B*). **(H)** CD45 median fluorescence intensity of microglia from LPS treated CTR (N = 6, *filled circles*) and *MG-TFAMKO* (N = 4, *open circles*) mice. **(I-K)** Fold change ($2^{-\Delta\Delta Ct}$) of expression of microglial function genes *Ifnβ1*, *Tnfα*, and *Cx3cr1* in LPS treated MG-TFAMKO (N = 4, *open circles*) and LPS treated CTR (N = 5, *filled circles*) mice relative to microglia from saline treated *MG-mitoGFP* mice (*Fig. 4B*). See *Table S5* and *Table S7* for Two-way ANOVA with Bonferroni correction for post hoc comparisons F^2 and P values. * $P < 0.05$, ** $P < 0.01$, *** $P < 0.001$. Mice were treated with 4-hydroxytamoxifen and analyzed 2 months later as described in methods. Data was plotted as mean ± SEM. Source data used to generate all graphs are provided as a Source Data file.

Supplementary Figure 9

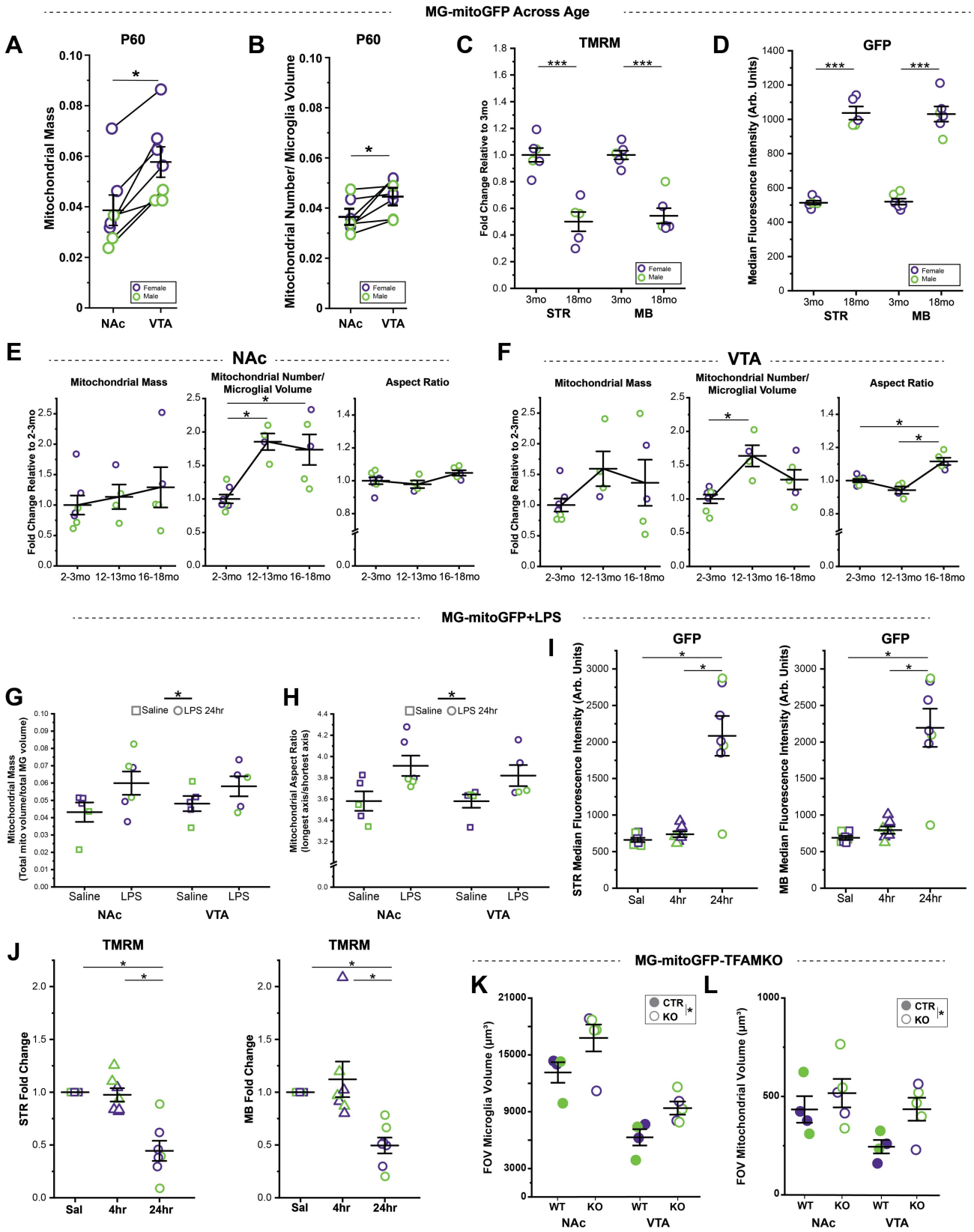

FIGURE S9: Most analyses do not suggest obvious sex-based differences in microglial mitochondrial features (*related to Figures 1, 4, 5, 6, S6, and 7*). Key graphs from the study annotated according to mouse sex with females labeled in *purple* and males in *green* **(A-B)** Mitochondrial mass (mitochondrial volume / microglial volume) and mitochondrial number (relative to cell volume) in NAc (N = 3 male, 4 female mice) and VTA (N = 3 male, 4 female mice). **(C-D)** Median fluorescence intensity of TMRM (normalized to individual cell's GFP signal to account for mitochondrial abundance) and GFP in microglia from the STR and MB of 3mo (STR N = 3 male, 3 female mice; MB 3 male, 3 female mice) and 18mo (STR N = 2 male, 3 female mice; MB 2 male, 4 female mice) mice. **(E-F)** Mitochondrial mass, number, and aspect ratio of NAc and VTA microglia during aging, normalized to mean values from 2-3mo animals (2-3mo N = 3 male, 4 female mice; 12-13mo N = 3 male, 1 female mice; 16-18mo N = 3 male, 2 female mice). **(G-H)** Microglial mitochondrial mass (mitochondrial volume / cell volume) and mitochondrial aspect ratio at 24hr after saline (N = 2 male, 3 female mice) or LPS injection (N = 3 male, 3 female mice). **(I-J)** Median Fluorescence Intensity of GFP and TMRM (normalized to individual cell's GFP signal to account for mitochondrial abundance) in STR and MB microglia from Saline (N = 3 male, 4 female mice), LPS 4hr (N= 3 male, 4 female mice), and LPS 24hr (N = 3 male, 4 female mice) mice. **(K-L)** FOV microglial volume across and FOV mitochondrial volume in CTR (N = 2 male, 2 female mice) and *MG-TFAMKO* (N = 3 male, 2 female mice) mice. Data was plotted as mean ± SEM for all graphs. Source data used to generate all graphs are provided as a Source Data file.

Supplementary Table 1: LPS Relative Gene Expression ANOVA Values.
Related to Figure 4B.

	Treatment		Region	
Gene	F Value	P Value	F Value	P Value
Tgfβ1	3.64818	0.03638	0.74976	0.39245
P2ry12	13.3998	0.0001	0.68065	0.41495
Csf1r	1.13966	0.34319	1.2454	0.27996
Cx3cr1	9.42003	0.000533	0.04288	0.83715
Cd68	4.11485	0.02483	5.06765	0.03076
Cd45	8.86009	0.00077	7.37401	0.01021
Itgam	14.09506	0.000246	1.07928	0.31341
Tnfα	10.23143	0.000317	0.01671	0.8979
Il1β	8.41188	0.00104	0.01627	0.89925
Micu1	5.40554	0.009	5.57555	0.02391
Cat	7.43629	0.00204	0.11711	0.73424
Ppargc1α	2.99706	0.06289	0.15601	0.69526
Nrf1	4.43215	0.01924	0.04594	0.83152
Mfn1	0.77771	0.46724	1.3191	0.25854
Dnm1l	4.8918	0.01338	0.31082	0.58072
Sod2	7.41671	0.00206	1.70341	0.20036
Tfam	2.1335	0.13357	1.72655	0.1974
Vdac1	12.4427	0.0001	0.06818	0.79554
Gpx1	20.79043	0.0001	1.01441	0.32076
Ndufa12	15.1893	0.0001	0.31724	0.57686
Atp5d	36.99749	0.0001	2.90216	0.09733
Cox4i1	12.11631	0.0001	1.69829	0.20102
Sdha	1.8012	0.18007	0.00647	0.93633

Supplementary Table 2: LPS Relative Gene Expression Post Hoc Analyses. Related to Figure 4B.

Genes		LPS 4hr vs Saline	LPS 24hr vs Saline	LPS 24hr vs LPS 4hr	MB vs STR
Tgfβ1	Probability	0.29856	0.03572	1	0.41278
	T value	-1.69206	-2.65327	-0.91161	-0.8289
P2ry12	Probability	0.00101	0.0001	1	0.45099
	T value	-3.97331	-4.8306	-0.76698	-0.76229
Csf1r	Probability	0.56513	1	1	0.33355
	T value	-1.37044	-0.94236	0.46004	-0.99552
Cx3cr1	Probability	0.00041798	0.45199	0.02272	0.95445
	T value	-4.27642	-1.46937	2.83451	-0.05753
Cd68	Probability	0.17688	1	0.03203	0.03952
	T value	-1.95212	0.75952	2.69744	-2.13869
Cd45	Probability	1	0.00219	0.00309	0.00733
	T value	0.05282	3.7024	3.58036	2.84717
Itgam	Probability	0.2025	0.000191597	0.01835	0.25439
	T value	1.95288	5.25978	3.12856	1.17964
Tnfα	Probability	0.000198161	0.117796	0.03916	0.9941
	T value	4.52848	1.9492	-2.61572	-0.00745
Il1β	Probability	0.00078693	0.42024	0.04286	0.98861
	T value	4.06006	1.50976	-2.57852	-0.01438
Micu1	Probability	0.27588	0.00708	0.4393	0.02479
	T value	-1.73266	-3.27919	-1.48524	-2.34559
Cat	Probability	0.00198	0.04203	0.71437	0.82245
	T value	-3.73851	-2.58666	1.2002	-0.22609
Ppargc1α	Probability	0.16869	0.09614	1	0.71262
	T value	-1.97473	-2.23293	-0.21646	-0.37134
Nrf1	Probability	0.21664	0.78056	0.01577	0.89431
	T value	1.85378	-1.24449	-2.97688	0.13382
Mfn1	Probability	1	0.76394	1	0.23403
	T value	-0.95289	-1.15815	-0.18361	1.21095
Dnm1l	Probability	0.02817	0.03151	1	0.58201
	T value	2.7491	2.70405	-0.0956	0.55561
Sod2	Probability	0.02418	0.00246	1	0.21081
	T value	2.80989	3.6624	0.78404	1.2747
Tfam	Probability	0.14411	0.35257	1	0.20397
	T value	2.04883	1.6048	-0.47402	-1.2945
Vdac1	Probability	0.09993	0.027	0.0001	0.64942
	T value	-2.2157	2.76603	4.93002	0.4585
Gpx1	Probability	0.06221	0.000865327	0.0001	0.2331
	T value	-2.42235	4.02733	6.3744	1.2134
Ndufa12	Probability	1	0.0001	0.00026155	0.66075
	T value	0.4567	4.98498	4.43509	-0.44264
Atp5d	Probability	1	0.0001	0.0001	0.13839
	T value	-0.26036	7.3228	7.44627	-1.51645
Cox4i1	Probability	1	0.000437904	0.00068819	0.25917
	T value	0.065	4.26059	4.11594	-1.14698
Sdha	Probability	0.32009	1	0.38157	0.98235
	T value	-1.65582	-0.0952	1.5624	0.02229

Supplementary Table 3: LPS Microglila- and Mitochondrial- Function Gene Correlation Values. Related to Figure 4D.

		Cd45			Il1β			Tnfα		
Genes		Saline	LPS 4hr	LPS 24hr	Saline	LPS 4hr	LPS 24hr	Saline	LPS 4hr	LPS 24hr
Atp5d	p-value	0.493624	0.137549	0.359852	0.257306	0.366931	0.13625	0.730913	0.775393	0.135199
	R value	0.334	0.524	0.233	0.131	0.322	0.501	0.218	0.098	0.493
Cox4i1	p-value	0.36897	0.06131	0.028433	0.405715	0.466862	0.206421	0.36897	0.648234	0.285042
	R value	0.44	0.612	0.669	0.395	0.274	0.401	0.443	-0.053	0.301
Ndufa12	p-value	0.409387	0.019198	0.004428	0.850599	0.074777	0.132485	0.80196	0.282537	0.062985
	R value	0.335	0.743	0.758	0.106	0.549	0.531	0.133	0.408	0.609
Sdha	p-value	0.510373	0.00215	0.008388	0.756231	0.141612	0.875422	0.950833	0.478784	0.86928
	R value	0.22	0.825	0.761	0.13	0.492	0.046	0.015	0.298	0.057
Nrf1	p-value	0.454638	0.007198	0.014085	0.994889	0.030809	0.830012	0.856943	0.03054	0.86928
	R value	0.323	0.787	0.717	0.055	0.668	-0.09	0.116	0.696	-0.062
Tfam	p-value	0.949681	0.016268	0.027111	0.826454	0.012704	0.522152	0.525826	0.071535	0.655121
	R value	0.047	0.712	0.69	-0.073	0.694	0.234	-0.197	0.636	0.152
Ppargc1α	p-value	0.637997	0.003019	0.205423	0.405715	0.59376	0.400037	0.405715	0.664901	0.522152
	R value	-0.189	0.679	0.429	-0.35	0.194	0.293	-0.336	0.169	0.208
Dnm1l	p-value	0.424293	0.06131	0.000262	0.912003	0.004815	0.206421	0.72725	0.004663	0.07025
	R value	0.326	0.587	0.891	-0.036	0.75	0.454	0.165	0.822	0.601
Mfn1	p-value	0.455014	1.92E-05	0.004428	0.637997	0.027085	0.652545	0.826454	0.211542	0.511684
	R value	0.3	0.83	0.799	-0.213	0.685	0.126	0.112	0.554	0.168
Micu1	p-value	0.752171	0.030809	0.285042	0.325813	0.179278	0.4977	0.856943	0.757082	0.285042
	R value	0.138	0.688	0.364	0.378	0.458	-0.347	0.063	0.144	-0.445
Vdac1	p-value	0.399239	0.030809	0.052616	0.493624	0.755757	0.253649	0.392043	0.400442	0.324445
	R value	0.422	0.691	0.59	0.087	0.105	0.381	0.363	-0.24	0.339
Sod2	p-value	0.295294	0.283494	0.830012	0.525465	0.00018	0.026746	0.295294	3.58E-06	0.003066
	R value	0.463	0.13	0.078	0.28	0.805	0.533	0.465	0.808	0.668
Cat	p-value	0.125641	0.155162	0.027111	0.295294	0.59376	0.561764	0.242937	0.146376	0.405422
	R value	0.621	0.5	0.402	0.443	-0.289	-0.315	0.491	-0.531	-0.409
Gpx1	p-value	0.171525	0.494331	0.001258	0.242937	0.308306	0.450881	0.431017	0.394667	0.298227
	R value	0.553	0.439	0.851	0.497	-0.408	0.294	0.304	-0.452	0.379

		Cx3cr1			P2ry12			Tgfβ1		
Genes		Saline	LPS 4hr	LPS 24hr	Saline	LPS 4hr	LPS 24hr	Saline	LPS 4hr	LPS 24hr
Atp5d	p-value	0.295294	0.603463	0.875422	0.206176	0.603463	0.228693	0.264582	0.065075	0.561764
	R value	0.239	0.193	0.024	0.207	0.191	-0.44	0.378	0.622	-0.229
Cox4i1	p-value	0.043146	0.091527	0.004428	0.249124	0.059409	0.612193	0.008057	0.044751	0.206421
	R value	0.736	0.515	0.762	0.541	0.537	0.169	0.849	0.653	0.425
Ndufa12	p-value	0.062521	0.645906	0.000728	0.049385	0.398998	0.522152	0.058573	0.00215	0.875422
	R value	0.673	0.144	0.489	0.688	0.261	-0.259	0.688	0.748	0.049
Sdha	p-value	0.050195	0.394667	0.001015	0.01295	0.227722	0.150088	0.053349	0.044665	0.001258
	R value	0.709	0.253	0.835	0.807	0.329	0.508	0.699	0.659	0.743
Nrf1	p-value	0.125641	0.725984	0.001015	0.053349	0.903248	0.137724	0.066148	0.073057	0.026746
	R value	0.59	-0.147	0.863	0.67	-0.068	0.54	0.65	0.606	0.675
Tfam	p-value	0.295294	0.648234	0.000112	0.035869	0.841112	0.206421	0.295294	0.072557	0.028563
	R value	0.4	-0.183	0.922	0.618	-0.087	0.453	0.421	0.64	0.683
Ppargc1α	p-value	0.455014	0.071535	0.001258	0.06157	0.001269	0.242876	0.525826	0.007817	0.135199
	R value	0.295	0.281	0.574	0.56	0.387	0.404	0.256	0.536	0.524
Dnm1l	p-value	0.249124	0.196433	0.094176	0.295294	0.319941	0.830012	0.295294	0.162525	0.612193
	R value	0.44	-0.489	0.565	0.425	-0.388	-0.126	0.391	0.46	0.127
Mfn1	p-value	0.404407	0.903248	0.001015	0.405715	0.755757	0.184554	0.409387	0.09787	0.027111
	R value	0.332	-0.082	0.864	0.32	-0.01	0.466	0.257	0.594	0.645
Micu1	p-value	0.008057	0.212226	0.007979	0.008839	0.117015	0.000783	0.052341	0.027085	0.000728
	R value	0.686	0.404	0.817	0.749	0.465	0.875	0.731	0.714	0.855
Vdac1	p-value	0.524534	0.000343	0.324445	0.36897	0.008035	0.851314	0.295294	0.12192	0.561764
	R value	0.067	0.61	0.418	0.009	0.607	0.055	0.231	0.544	0.195
Sod2	p-value	0.438239	0.09787	0.358364	0.535235	0.153205	0.094176	0.125641	0.00215	0.150088
	R value	0.344	-0.577	-0.415	0.239	-0.532	-0.58	0.538	0.352	-0.518
Cat	p-value	0.136261	3.46E-05	1.26E-05	0.264582	8.51E-05	0.000235	0.043146	0.196433	2.79E-08
	R value	0.59	0.936	0.87	0.477	0.927	0.905	0.733	0.486	0.926
Gpx1	p-value	0.038467	0.000343	0.027111	0.178605	0.00073	0.915929	0.058573	0.308306	0.358364
	R value	0.748	0.816	0.684	0.54	0.852	-0.002	0.683	0.399	0.315

Supplementary Table 4: LPS CD68 and Mitochondrial Function Gene Correlation Values. Related to Figure S4.

		Cd68		
Genes		Saline	LPS 4hr	LPS 24hr
Atp5d	p-value	0.242937	0.146376	0.568328
	R value	0.333	0.493	0.155
Cox4i1	p-value	0.136261	0.009325	0.021439
	R value	0.604	0.759	0.701
Ndufa12	p-value	0.171525	0.009708	0.027111
	R value	0.544	0.736	0.666
Sdha	p-value	0.018529	0.006375	0.015194
	R value	0.783	0.721	0.741
Nrf1	p-value	0.178605	0.240222	0.001499
	R value	0.549	0.408	0.844
Tfam	p-value	0.295294	0.155162	0.000728
	R value	0.413	0.48	0.883
Ppargc1α	p-value	0.326307	0.006855	0.000783
	R value	0.39	0.652	0.647
Dnm1l	p-value	0.295294	0.646276	0.097101
	R value	0.391	0.187	0.558
Mfn1	p-value	0.46778	0.141192	0.010282
	R value	0.231	0.425	0.758
Micu1	p-value	0.007659	0.009708	0.015224
	R value	0.873	0.737	0.641
Vdac1	p-value	0.317446	0.019198	0.568328
	R value	0.106	0.727	0.226
Sod2	p-value	0.438239	0.494331	0.358364
	R value	0.332	-0.291	-0.455
Cat	p-value	0.136644	0.008035	0.000103
	R value	0.575	0.772	0.678
Gpx1	p-value	0.125641	0.013089	4.58E-05
	R value	0.6	0.745	0.62
Il1β	p-value	0.848035	0.396429	0.928713
	R value	0.307	-0.096	0.14
Tnfα	p-value	0.888728	0.638932	0.844106
	R value	-0.041	-0.165	0.083
Tgfβ1	p-value	0.00144	0.033754	0.000626
	R value	0.858	0.635	0.666
Cd45	p-value	0.87144	0.112515	0.046827
	R value	0.069	0.479	0.635
Cx3cr1	p-value	4.05E-05	0.04008	2.76E-11
	R value	0.876	0.666	0.885
P2ry12	p-value	4.58E-05	0.00905	0.000348
	R value	0.879	0.777	0.398752

Supplementary Table 5: MG-TFAMKO FACS and relative expression ($2^{(-\Delta CT)}$) ANOVA Values. Related to Figure 8 and Figure S8.

	ANOVA - Genotype		ANOVA - Region		Posthoc Bonferroni - Genotype		Posthoc Bonferroni - Region		TFAMKO STR vs CTR STR		TFAMKO MB vs CTR MB	
Protein Level	F Value	P Value	F Value	P Value	T Value	Probability	T Value	Probability	T Value	Probability	T Value	Probability
CD45	0.02292	0.88118	**25.02099**	**0.0001**	-0.15139	0.88118	**-5.01669**	**0.0001**	-0.34282	1	0.12872	1
CX3CR1	1.68024	0.20965	**19.34603**	**0.000278**	1.29624	0.20965	**4.18028**	**0.000462**	2.0901	0.29753	-0.25694	1
FSC-A	**20.69067**	**0.0002**	1.15312	0.29568	**4.5487**	**0.0002**	1.01152	0.32385	**3.53081**	**0.01231**	2.89202	0.05408
SSC-A	**13.92572**	**0.00132**	0.39895	0.053479	**3.73172**	**0.00132**	0.52831	0.6031	**3.10839**	**0.03323**	2.16905	0.25384
Gene Level	F Value	P Value	F Value	P Value	T Value	Probability	T Value	Probability	T Value	Probability	T Value	Probability
Atp5d	**45.95018**	**0.0001**	2.01542	0.17111	**-6.77866**	**0.0001**	1.33835	0.1958	**-5.21762**	**0.00025**	**-4.36885**	**0.00178**
Cat	**9.26908**	**0.0064**	0.40487	0.5318	**-3.04452**	**0.0064**	-0.37529	0.71139	-1.02317	1	**-3.28242**	**0.02234**
Cd45	0.02413	0.8781	**15.02046**	**0.00095**	0.15535	0.8781	**-3.90608**	**0.00088**	0.21243	1	0.00727	1
Cd68	0.01473	0.9046	**24.29689**	**0.0001**	-0.12138	0.9046	**4.87956**	**0.0001**	-0.58592	1	0.41426	1
Cox4i1	**126.6341**	**0.0001**	0.07841	0.78235	**-11.25318**	**0.0001**	0.32718	0.74694	**-7.77651**	**0.0001**	**-8.13789**	**0.0001**
Csf1r	3.10295	0.09343	2.43891	0.13404	-1.76152	0.09343	1.63864	0.11692	-1.01638	1	-1.47479	0.93503
Cx3cr1	**17.01521**	**0.00053**	**12.58095**	**0.002**	**-4.12495**	**0.00053**	**3.36426**	**0.00309**	**-3.89155**	**0.00544**	-1.94201	0.39812
Dnm1l	**4.70405**	**0.04232**	0.8066	0.37981	**2.16888**	**0.04232**	-0.85845	0.40081	1.75281	0.5697	1.31445	1
Gpx1	4.03523	0.05825	21.4793	0.15831	-2.00879	0.0825	-1.3792	0.18306	-0.97209	1	-1.86877	0.45824
Ifnβ1	**16.45206**	**0.00062**	2.29609	0.14535	**4.05611**	**0.00062**	1.1731	0.25454	1.34674	1	**4.38947**	**0.0017**
Il1β	**12.24035**	**0.00226**	2.04	0.16864	**-3.49862**	**0.00226**	-1.16721	0.25685	-1.1297	1	**-3.65079**	**0.00954**
Itgam	0.66387	0.42479	0.27531	0.60556	-0.81478	0.42479	0.42126	0.67806	-1.04002	1	-0.11226	1
Mavs	**7.40066**	**0.01318**	0.00075	0.97845	**-2.72042**	**0.01318**	-0.05566	0.95616	-2.04043	0.32839	-1.80681	0.51517
Mb21d1 (cGas)	3.33367	0.08284	**6.31848**	**0.02062**	1.82584	0.08284	-2.22691	0.0376	2.63979	0.09427	-0.05767	1
Mfn1	0.14986	0.70276	0.99939	0.3294	0.38712	0.70276	-1.11031	0.28004	-0.12966	1	0.67713	1
Micu1	**38.60565**	**0.0001**	**6.75829**	**0.01714**	**-6.21334**	**0.0001**	**2.62282**	**0.0163**	**-4.45092**	**0.00147**	**-4.33608**	**0.00192**
Ndufa12	**7.17777**	**0.01442**	0.28616	0.59859	**-2.67914**	**0.01442**	0.63132	0.53498	-1.523	0.86049	-2.26587	0.20827
Nlrp3	0.04784	0.82908	0.61263	0.44297	-0.218873	0.82909	0.87232	0.39338	0.17378	1	-0.48312	1
Nrf1	**5.00741**	**0.03678**	0.8524	0.36688	**-2.23772**	**0.03678**	-0.79631	0.4352	-0.99648	1	-2.16815	0.25431
P2ry12	0.08108	0.77877	**9.97483**	**0.00494**	0.28747	0.77877	**3.09392**	**0.00572**	-0.25539	1	0.65808	1
Ppargc1α	**5.55677**	**0.02993**	0.075	0.78731	**2.35628**	**0.02993**	0.47328	0.6417	2.13737	0.27926	1.19633	1
Sdha	**8.99841**	**0.00708**	1.12328	0.30185	**-2.99973**	**0.00708**	1.18546	0.24973	-1.65856	0.67684	-2.58371	0.10644
Sod2	**4.7674**	**0.04109**	1.78966	0.19598	**-2.18344**	**0.04109**	-1.23455	0.23131	-1.03269	1	-2.05515	0.31896
Tfam probe 1	**128.37**	**0.0001**	1.31314	0.26535	**11.33005**	**0.0001**	1.39016	0.17976	**8.96526**	**0.0001**	**7.05784**	**0.0001**
Tfam probe 2	**87.30932**	**0.0001**	0.30509	0.58683	**9.34395**	**0.0001**	0.73623	0.47014	**7.34364**	**0.0001**	**5.87069**	**0.0001**
Tgfβ1	**15.69556**	**0.00077**	**9.22353**	**0.00651**	**-3.96176**	**0.00077**	**2.87826**	**0.00929**	**-3.64577**	**0.00965**	-1.95701	0.38671
Tlr9	2.81938	0.10869	1.89537	0.18381	-1.6791	0.10869	-1.36979	0.18594	-1.0766	1	-1.29801	1
Tmem173 (Sting)	0.68991	0.416	0.34889	0.56136	0.83061	0.416	-0.58405	0.56571	0.65007	1	0.52459	1
Tnfα	**29.54024**	**0.0001**	**7.40789**	**0.01314**	**-5.43509**	**0.0001**	**-2.53105**	**0.01987**	-2.88394	0.05506	**-4.80244**	**0.00065**
Vdac1	0.10673	0.7473	0.39367	0.53748	-0.32669	0.7473	-0.39797	0.69487	0.76612	1	-1.22813	1

Supplementary Table 6: Comparison of gene average fold changes ($2^{(-\Delta\Delta CT)}$) for MG-mitoGFP and MG-mitoGFP-TFAMKO samples following LPS challenge, relative to MG-mitoGFP saline treated samples. Related to Figure 4 and 8.

STRIATUM - Average Fold Changes (2^(-ΔΔCt)) to MG-mitoGFP + Saline

	MG-mitoGFP + Saline	MG-mitoGFP + 4hr LPS	MG-mitoGFP + 24hr LPS	MG-mitoGFP + Saline	MG-mitoGFP-TFAMWT + 12hr LPS	MG-mitoGFP-TFAMKO + 12hr LPS
Mitochondrial Related Genes	endo control: Gapdh	endo control: Gapdh	endo control: Gapdh	endo control: Gusb	endo control: Gusb	endo control: Gusb
Atp5d	1	1.0643	1.6086	1	0.7684	0.8749
Cat	1	0.7150	0.7701	1	0.3665	0.4199
Cox4i1	1	1.2138	1.4266	1	0.6196	0.8524
Dnm1l	1	1.6079	1.3928	1	1.0166	1.0736
Gpx1	1	0.7881	1.5620	1	0.9054	0.9643
Mavs				1	0.5385	0.5734
Mfn1	1	1.0667	0.9384	1	0.6366	0.7581
Micu1	1	0.8633	0.6883	1	0.3600	0.4794
Ndufa12	1	1.2943	2.0937	1	1.1686	1.2309
Nrf1	1	1.3074	0.9263	1	0.5448	0.6396
Ppargc1α	1	0.8476	0.6484			
Sdha	1	0.8998	0.9342	1	0.6261	0.7414
Sod2	1	2.3658	2.2959	1	1.6468	2.1885
Tfam probe 1				1	0.7573	0.4564
Tfam probe 2	1	1.4357	1.2646	1	0.5454	0.3448
Vdac1	1	0.9288	1.2152	1	0.6042	0.7660
Microglial Related Genes						
Cd45	1	1.1367	1.3506	1	0.5219	0.5597
Cd68	1	0.8428	1.0707	1	0.3137	0.4081
Csf1r	1	0.9567	0.9133	1	0.4170	0.4551
Cx3cr1	1	0.5828	0.8266	1	0.2943	0.2885
Ifnβ1				1	1.1322	0.8297
Il1β	1	79.2113	37.1183	1	17.9284	16.9704
Itgam	1	1.4364	1.5346	1	0.6232	0.7448
Mb21d1 (cGas)				1	1.1895	1.2916
Nlrp3				1	0.8822	1.0850
P2ry12	1	0.4974	0.3403	1	0.1037	0.1020
Tgfβ1	1	0.8933	0.7280	1	0.3126	0.3276
Tlr9				1	0.5578	0.6234
Tmem173 (Sting)				1	0.3207	0.3293
Tnfα	1	100.1634	37.9237	1	21.0308	35.9473

MIDBRAIN - Average Fold Changes (2^(-ΔΔCt)) to MG-mitoGFP + Saline

	MG-mitoGFP + Saline	MG-mitoGFP + 4hr LPS	MG-mitoGFP + 24hr LPS	MG-mitoGFP + Saline	MG-mitoGFP-TFAMWT + 12hr LPS	MG-mitoGFP-TFAMKO + 12hr LPS
Mitochondrial Related Genes	endo control: Gapdh	endo control: Gapdh	endo control: Gapdh	endo control: Gusb	endo control: Gusb	endo control: Gusb
Atp5d	1	0.9707	1.5187	1	0.8185	0.8055
Cat	1	0.6389	0.7711	1	0.4019	0.4204
Cox4i1	1	0.9812	1.4290	1	0.6812	0.7862
Dnm1l	1	1.5099	1.5534	1	1.0222	1.1646
Gpx1	1	0.6631	1.6610	1	0.7774	0.8051
Mavs				1	0.5048	0.6817
Mfn1	1	0.9863	0.9047	1	0.5513	0.6506
Micu1	1	0.9840	0.8309	1	0.5354	0.5724
Ndufa12	1	1.1208	2.0564	1	1.2315	1.2866
Nrf1	1	1.3079	0.8748	1	0.5526	0.5607
Ppargc1α	1	1.2643	0.9411			
Sdha	1	0.9215	1.0947	1	0.7271	0.7724
Sod2	1	2.9739	3.3247	1	3.4827	3.5568
Tfam probe 1				1	0.7846	0.4604
Tfam probe 2	1	1.2224	1.1549	1	0.5519	0.3341
Vdac1	1	0.8132	1.2727	1	0.6335	0.7101
Microglial Related Genes						
Cd45	1	0.9856	1.3504	1	0.4658	0.4768
Cd68	1	0.7738	1.1420	1	0.3439	0.3625
Csf1r	1	0.8517	0.8822	1	0.3997	0.4461
Cx3cr1	1	0.5303	0.8872	1	0.3374	0.3277
Ifnβ1				1	0.5462	0.4864
Il1β	1	196.3872	39.4252	1	61.5999	31.5696
Itgam	1	1.4656	1.8833	1	0.8542	0.9547
Mb21d1 (cGas)				1	1.2161	1.3084
Nlrp3				1	1.3447	1.3352
P2ry12	1	0.4481	0.3843	1	0.0900	0.1108
Tgfβ1	1	0.8748	0.7794	1	0.3271	0.3190
Tlr9				1	0.3916	0.4157
Tmem173 (Sting)				1	0.3253	0.3055
Tnfα	1	63.6890	25.8358	1	26.2134	26.6842

Supplementary Table 7: MG-mitoGFP-TFAMKO 12hr LPS FACS and fold change ($2^{(-\Delta\Delta CT)}$) ANOVA Values. Related to Figure 8 and Figure S8.

	ANOVA - Genotype		ANOVA - Region		Posthoc Bonferroni - Genotype		Posthoc Bonferroni - Region		TFAMKO STR vs CTR STR		TFAMKO MB vs CTR MB	
Protein Level	F Value	P Value	F Value	P Value	T Value	Probability	T Value	Probability	T Value	Probability	T Value	Probability
CD45	0.35092	0.56187	**28.09286**	**0.0001**	0.59239	0.56187	**-5.47722**	**0.0001**	0.18451	1	0.65326	1
CX3CR1	1.0023	0.33166	**17.12375**	**0.00077**	1.00115	0.33166	**4.31983**	**0.00053**	1.04191	1	0.37393	1
GFP	0.68349	0.42055	3.70828	0.0721	-0.82673	0.42055	-2.0286	0.05948	-0.80352	1	-0.36565	1
TMRM (norm to GFP)	0.000133	0.99091	2.99229	0.1029	0.01157	0.99091	1.74114	0.10085	-0.07616	1	0.09253	1
FSC-A	**15.99502**	**0.00103**	0.00217	0.96338	**-3.9938**	**0.00103**	-0.10335	0.91897	**-3.02113**	**0.04868**	-2.63485	0.1081
SSC-A	3.03955	0.10044	0.43762	0.51769	1.74343	0.10044	0.65455	0.52206	1.16136	1	1.30422	1
Gene Level	F Value	P Value	F Value	P Value	T Value	Probability	T Value	Probability	T Value	Probability	T Value	Probability
Atp5d	0.72773	0.40798	0.031	0.86276	-0.85307	0.40798	0.05531	0.95667	-1.37387	1	0.16745	1
Cat	1.36818	0.26165	0.34219	0.56788	-1.16969	0.26165	-0.65222	0.52483	-1.22933	1	0.42486	1
Cd45	0.30415	0.58999	2.47447	0.13803	-0.5515	0.58999	1.54885	0.14372	-0.60495	1	-0.17498	1
Cd68	**4.75047**	**0.04686**	0.08683	0.77257	**-2.17956**	**0.04686**	0.13311	0.896	-2.57458	0.13224	-0.50778	1
Cox4i1	**9.4789**	**0.00817**	0.00174	0.96731	**-3.07878**	**0.00817**	-0.08819	0.93098	-3.00025	0.05728	-1.3538	1
Csf1r	2.10639	0.16872	0.20527	0.65744	-1.45134	0.16872	0.47173	0.64439	-0.9261	1	-1.12641	1
Cx3cr1	0.02797	0.86958	0.78802	0.3897	0.16723	0.86958	-0.89802	0.38436	0.08798	1	0.14852	1
Dnm1l	1.99438	0.17972	0.46871	0.50476	-1.41223	0.17972	-0.62125	0.54442	-0.57078	1	-1.4264	1
Gpx1	0.19037	0.66926	2.09591	0.16972	-0.43632	0.66926	1.43919	0.17208	-0.41957	1	-0.19748	1
Ifnβ1	1.38512	0.25885	**9.10928**	**0.00921**	1.17691	0.25885	**3.12508**	**0.00745**	1.38953	1	0.27487	1
Il1β	1.18581	0.29457	4.19297	0.05983	1.08895	0.29457	-2.17465	0.04729	0.04761	1	1.4924	0.9467
Itgam	**9.71587**	**0.00757**	**38.28983**	**0.0001**	**-3.11703**	**0.00757**	**-6.25963**	**0.0001**	-2.41403	0.1803	-1.99412	0.39595
Mavs	**7.42879**	**0.01641**	0.92349	0.35287	**-2.72558**	**0.01641**	-0.76275	0.45827	-0.63566	1	**-3.21889**	**0.0371**
Mb21d1 (cGas)	0.71785	0.4111	0.03603	0.85217	-0.84726	0.4111	-0.19579	0.84759	-0.62932	1	0.56888	1
Mfn1	**5.01149**	**0.04194**	3.81642	0.07103	**-2.23864**	**0.04194**	1.94061	0.07272	-1.74185	0.62071	-1.42406	1
Micu1	**4.60747**	**0.04984**	**13.55873**	**0.00246**	**-2.1465**	**0.04984**	**-3.83155**	**0.00183**	-2.31719	0.21691	-1.71174	0.65398
Ndufa12	0.48029	0.49963	0.48985	0.49546	-0.69303	0.49963	-0.70896	0.48999	-0.51978	1	-0.46031	1
Nlrp3	0.29591	0.59502	4.02278	0.06461	-0.54397	0.59502	-2.0849	0.05586	-0.80716	1	0.03787	1
Nrf1	0.44038	0.51772	0.21063	0.65332	-0.66361	0.51772	0.39932	0.69568	-0.86441	1	-0.07408	1
P2ry12	0.63472	0.43893	0.04136	0.84178	-0.7967	0.43893	0.30901	0.76186	0.09682	1	-1.22352	1
Sdha	2.89461	0.11097	1.95487	0.18382	-1.70136	0.11097	-1.48974	0.15874	-1.72712	0.63679	-0.67896	1
Sod2	0.14255	0.71142	3.85925	0.06964	-0.37756	0.71142	-2.00879	0.06425	-0.46973	1	-0.06423	1
Tfam probe 1	**35.54773**	**0.0001**	0.08884	0.77004	**5.96219**	**0.0001**	-0.32467	0.75023	**4.05931**	**0.00703**	**4.37251**	**0.00383**
Tfam probe 2	**22.46606**	**0.00032**	0.00237	0.96186	**4.73984**	**0.00032**	0.0272	0.97868	**3.21378**	**0.03748**	**3.48936**	**0.02166**
Tgfβ1	0.0166	0.89933	0.01159	0.91578	-0.12883	0.89933	-0.15594	0.87831	-0.4003	1	0.20992	1
Tlr9	1.05088	0.32269	**18.2921**	**0.00077**	-1.02513	0.32269	**4.25042**	**0.00081**	-1.06107	1	-0.38868	1
Tmem173 (Sting)	0.01694	0.89829	0.0505	0.82544	0.13017	0.89829	0.18902	0.85279	-0.14263	1	0.32671	1
Tnfα	1.83805	0.19665	0.12926	0.72457	-1.35575	0.19665	0.21946	0.82946	-1.85866	0.50535	-0.05866	1
Vdac1	**7.44427**	**0.01632**	0.09222	0.76584	**-2.72842**	**0.01632**	0.19653	0.84702	-2.6189	0.12132	-1.23967	1

Supplementary Table 8: Primers and probes used for qPCR experiments. Related to Figures 4, S4, 8, and S8.

Gene	TaqMan Assay ID or custom probe	Forward Primer	Reverse Primer
Aldh1l1	Mm03048957_m1		
Atp5d	Mm00502864_m1		
Cat	Mm00437992_m1		
Cd45 (Ptprc)	Mm01293577_m1		
Cd68	Mm03047343_m1		
Cox4i1	Mm01250094_m1		
Csrf1	Mm01266652_m1		
Cx3cr1	Mm00438354_m1		
Dnm1l	Mm01342903_m1		
Gapdh	MGB - CTCATGACCACAGTCCA - VIC	GACAACTTTGGCATTGTGGAA	CACAGTCTTCTGGGTGGCAGTGA
Gpx1	Mm04207457_g1		
Ifnβ1	Mm00439552_s1		
Il1β	Mm00434228_m1		
Itgam	Mm00434455_m1		
Mavs	Mm00523170_m1		
Mb21d1 (cGas)	Mm01147496_m1		
Mfn1	Mm00612599_m1		
Micu1	Mm00522783_m1		
Nrf1	Mm01135606_m1		
Ndufa12	Mm01240336_m1		
Nlrp3	Mm00840904_m1		
Olig1	Mm00497537_s1		
Olig2	Mm01210556_m1		
P2ry12	Mm00446026_m1		
Ppargc1α	Mm01208835_m1		
Ppp1r1b	Mm00454892_m1		
Sdha	Mm01352366_m1		
Slc1a2	Mm01275814_m1		
Slc32a1	Mm00494138_m1		
Sod2	Mm01313000_m1		
Tfam probe 1	Mm00627275_g1		
Tfam probe 2	Mm01148667_m1		
Tgfβ1	Mm01178820_m1		
Tlr9	Mm07299609_m1		
Tmem173 (Sting)	Mm01158117_m1		
Tnfα	Mm00443258_m1		
Vdac1	Mm00834272_m1		